

ADVERTIMENT. L'accés als continguts d'aquesta tesi queda condicionat a l'acceptació de les condicions d'ús establertes per la següent llicència Creative Commons:  <https://creativecommons.org/licenses/?lang=ca>

ADVERTENCIA. El acceso a los contenidos de esta tesis queda condicionado a la aceptación de las condiciones de uso establecidas por la siguiente licencia Creative Commons:  <https://creativecommons.org/licenses/?lang=es>

WARNING. The access to the contents of this doctoral thesis it is limited to the acceptance of the use conditions set by the following Creative Commons license:  <https://creativecommons.org/licenses/?lang=en>



Field-Induced Reversible Tuning of Oxygen Doping in High-Temperature Superconductors

A dissertation submitted for the degree of
DOCTOR OF PHILOSOPHY IN MATERIALS SCIENCE

by

Alejandro Fernández Rodríguez

Supervisors:

Dr. Anna Palau and Dr. Narcís Mestres

Superconducting Materials and Large Scale Nanostructures (SUMAN)

Institut de Ciència de Materials de Barcelona (ICMAB-CSIC)

Tutor: Dr. Carles Navau

Doctorat en Ciència de Materials

Departament de Física - Facultat de Ciències

Universitat Autònoma de Barcelona

February 2022

Alejandro Fernández Rodríguez
ICMAB-CSIC
Campus de la UAB, Bellaterra, Barcelona, Spain
afernandez3@icmab.es

February 2022



This work is published under Creative Commons, CC BY-NC-ND 4.0
The material can be copied and reproduced, providing appropriate credit to the author. You may not use the whole or part of the material for any commercial purposes. No derivatives of the material are allowed under this license. The distribution of modified material requires the authors permission.

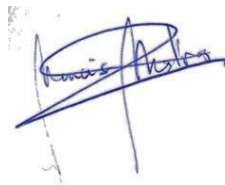
Memòria presentada per aspirar al Grau de Doctor en Ciència de Materials per

Alejandro Fernández Rodríguez

Amb el vist i plau de:



Director:
Dr. Anna Palau
Masoliver



Director:
Dr. Narcís Mestres
Andreu

Tutor:
Dr. Carles Navau Ros

Bellaterra, 17 de Febrer de 2022

La **Dra. Anna Palau Masoliver**, Investigadora Científic del Institut de Ciència de Materials de Barcelona (ICMAB), Consejo Superior de Investigaciones Científicas, CSIC,

El **Dr. Narcís Mestres Andreu**, Investigador Científic del Institut de Ciència de Materials de Barcelona (ICMAB), Consejo Superior de Investigaciones Científicas, CSIC,

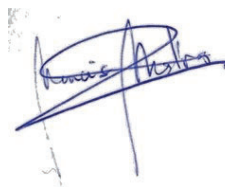
Certifiquen:

Que **Alejandro Fernández Rodríguez** ha realitzat sota la seva direcció el treball d'investigació que s'exposa a la memòria titulada "*Field-Induced Reversible Tuning of Oxygen Doping in High-Temperature Superconductors*" per optar al grau de **DOCTOR per la Universitat Autònoma de Barcelona**.

Que el dissenys dels experiments, la fabricació dels dispositius, les mesures, l'anàlisi dels resultats, la redacció dels articles i d'aquesta memòria són fruit del treball d'investigació realitzat per **Alejandro Fernández Rodríguez**.



Director:
Dr. Anna Palau
Masoliver



Director:
Dr. Narcís Mestres
Andreu

Bellaterra, 17 de Febrer de 2022

Acknowledgements

I have spent around five years here at ICMAB. Almost one year doing the Master Thesis and then four years more for this Doctoral Thesis. Along this beautiful journey I have met many people that have accompanied me and helped me in different ways. For most of the PhD students this is the first semi-professional experience, the first contact with a working environment, adults, bureaucracy, etc. That is the reason why the people you have around plays a very important role in my opinion.

Of course I have to start with my two supervisors, Dr. Anna Palau and Dr. Narcís Mestres. I am forever grateful. You trusted me and gave me the opportunity to continue the research I started in my Master Thesis. During these four years both of you have been deeply involved in my work, discussing almost every day what to do checking how the experiments were going and even doing them together. From the beginning you were very patient with me and taught me everything, and always in such a good mood. I hope you have been as comfortable as I have been with you working all this time.

I have to thank Prof. Teresa Puig, head of "Superconducting Materials and large scale nanostructures" group (SUMAN) and Prof. Xavier Obradors, director of ICMAB but also part of our group. Teresa welcomed me to the group and both took part in many discussions in different talks, meetings and during the preparation of some publications.

I am very thankful to Prof. Alejandro Silhanek, Stefan Marincovic and colleagues in Liège. We made continuous collaborations along these years that concluded in several publications. You also gave me the opportunity to do an internship in your group but it had to be first postponed and later cancelled due to the pandemic.

I want to thank Prof. Xavier Granados. You helped me a lot doing the simulations and suggesting new things to do with them. Also you took part in many discussions regarding this thesis.

I have to thank also Dr. Gemma Rius for helping me with the Raman measurements and being always ready for it.

I am grateful to Dr. Carlo Marini and Dr. Laura Simonelli from ALBA for helping me with the preparation of the experiment, the measurements and the following data analysis the two times I had the chance to have bean time.

I can not forget about Dr. Mar Tristany, project manager of the group. You helped me a lot, even before starting the thesis, with all the paperwork, which is always hard for a new student. Thank you for being always willing to help and receiving me with a smile.

I want to thank the entire staff in SUMAN group. We are not all working in the same project but still share the laboratories everyday, the weekly meetings, lab cleanings and group activities. I can not forget about some former members like Juri, Ziliang, Ferran, Joshua, Alex, Laia, Júlia, Bohores, Bernat and specially Juan Carlos, you were the only student working in the same topic as me and you taught many things and tricks in the labs and ICMAB facilities in general. With all of you I shared time in the institute but also some time outside after work or during the weekends.

Another very important group of people for a PhD student are the office mates. All along this years I was in the same office, but shared it with many different people. Some were mentioned before, and I have to mention Mathieu, Pengmei, Yunwei, Lavinia, Huan, Xiao, Aleix and Ais. I have to include of course Jordi, with you I shared long time working together and tried to teach you everything I knew. I have to express thanks to (already) Dr. Hailin Wang, who grew many of my samples and also shared very good moments. I also want to add more people from ICMAB like Pamela, Artur, Ma, Irene, Milena, Francesco, Adara, Sohini, Jewel Stefania, Adriá and Felip. With all of you I shared a lot of time these years during work but also during breaks, lunch and outside ICMAB. I hope our friendship remains after this is over.

I am very thankful to the Nanoquim staff. Luigi, Neus and the two Martas. I think I am one of the students with more time spent in the clean room and in your office, and also the one who sent more e-mails to reschedule my reservations. You all were always nice and funny with me

and our conversations during some experiments made the wait shorter and enjoyable.

The "Low Temperatures and Magnetometry" laboratory is a place where I spent a lot of time at ICMAB, doing my experiments. I want to thank the technician in charge, Bernat Bozzo. You helped me a lot in many occasions with problems in the measurements and giving some ideas when trying new things. Of course we shared also some good conversations. I want to thank also the rest of technicians of other services at ICMAB that maybe helped me few times but somehow helped me to do this thesis too.

There are also several groups of people I am very grateful to, although they are not directly involved in the research. The maintenance service, the cleaning service, the IT guys, the receptionists and the whole administration of ICMAB. You always helped me when I asked and were always nice to me.

Finally we acknowledge financial support from Ministerio de Ciencia e Innovación for their funding through FPI fellowship program (BES-2016-077310) inside the project Severo Ochoa Programme for Centres of Excellence in R&D (SEV-2015- 0496), SUMATE project (RTI2018-095853-B-C21), cofinanced by the European Regional Development Fund, the COST programme NanoCoHybri (CA 16218), and from the Catalan Government with 2017 SGR 1519.

Abstract

Modulation of carrier concentration in strongly correlated oxides offers the unique opportunity to induce different phases in the same material, which dramatically change their physical properties. Specially, the possibility of reversibly modifying the metal-insulator transition (MIT) in perovskite oxides, by means of an electric field as the external control parameter, is a very active area of research in condensed matter physics, and a promising technique to generate new solid-state devices with interesting functionalities.

In this thesis we have studied the electric manipulation of the metal (superconducting) to insulator transition in high-temperature superconductor $YBa_2Cu_3O_{7-\delta}$ thin films by field-induced oxygen doping. We demonstrate that non-volatile volume phase transitions can be locally modulated to fabricate transistor-like devices, with free-resistance channels, in which the electric field magnitude and direction, temperature, and anisotropic oxygen mobility determine their characteristics. Moreover, we have shown the potential to tune the oxygen doping in an extended region of YBCO patterned structures by mass-selective migration of oxygen atoms induced by electromigration effects. The studied devices work both at the superconducting and normal state thus providing the basis for the design of room temperature multi-terminal memristive structures, as a promising approach for neuromorphic computing applications, as well as emerging functional superconducting systems. The knowledge acquired throughout this work opens up opportunities for the design of novel devices for energy-efficient Information and Communication Technologies (e-ICT).

Motivation and objectives

The aim of this thesis is studying the field-induced reversible tuning of oxygen doping in superconducting strongly correlated oxides. We will explore the electric manipulation of the metallic (superconducting) to insulator phase transition in $YBa_2Cu_3O_{7-\delta}$ (YBCO) films through local modulation of oxygen.

The thesis is structured in 5 Chapters. First in chapter 1 we introduce the main concepts of Metal-Insulator Transition and resistive switching effects in strongly correlated oxides. We also give a short overview of high-temperature superconductors and possible applications of the studied effects. Chapter 2 is dedicated to describe the materials and fabrication and characterization techniques used in the thesis.

The objective of chapter 3 is to investigate the effect of reversibly tuning the oxygen doping in YBCO thin films by means of electric field-induced oxygen diffusion. We will systematically analyze the tuning of a metal-insulator transition induced by gate-modulated oxygen doping and the influence of this phenomenon in the physical properties of the material, which will be studied using different electric transport measurements, Raman spectroscopy and also numeric simulations, trying to understand the physical mechanisms behind. The resistive switching characteristics of the fabricated devices will be explored at room temperature and at the superconducting state for its applicability in energy efficient memory and logic devices. Different designs will be used to study the local modulation of oxygen through various gate configurations.

The aim of chapter 4 is to study oxygen diffusion in YBCO thin films, stimulated by current pulses, using controlled electromigration processes. The generation of a current-induced metal-insulator transition and the effect of electromigration in the properties of the material will be explored using electric transport measurements, Raman spectroscopy and optical

microscope imaging. The temperature dependence of both critical current density and electromigration current density will be compared to study the possible damage in the material when reaching the dissipative state. Direct visualization of oxygen diffusion will be used to shed light on the distribution and homogeneity of oxygen vacancies in YBCO patterned bridges. The work presented in this chapter has been performed in collaboration with the group of Alejandro Silhanek (University of Liege, Belgium).

The objective of chapter 5 is to explore the performance of resistive switching effects at room temperature for neuromorphic applications. The aim is to design and optimize YBCO devices to emulate certain functionalities of a brain synapse. The volume-like switching effects induced in the proposed YBCO devices may introduce robustness and flexibility to neuromorphic systems. We will study the implementation of learning capabilities and the possibility to fabricate devices with multiple gate inputs.

Contents

Acknowledgements	ix
Abstract	xii
Motivation and objectives	xiii
Contents	xv
1 Introduction	1
1.1 Metal-insulator transition in strongly correlated materials	1
1.2 Resistive Switching (RS)	5
1.2.1 Operation principles of a Resistive Switching cell	6
1.2.2 Resistive Switching mechanisms	8
1.3 Strongly correlated superconducting oxides	10
1.3.1 High-Temperature superconductors (HTS)	11
1.3.2 Superconductor-insulator transition (SIT)	14
1.4 Neuromorphic Computing	15
2 Experimental methodology	21
2.1 Sample growth	21
2.1.1 Substrates	21
2.1.2 Pulsed Laser Deposition (PLD)	22
2.1.3 Chemical solution deposition (CSD)	24
2.2 Basic structural and physical characterization	27
2.2.1 Composition and structural analysis	27
2.2.2 Measurement of thin film thickness	28
2.2.3 Magnetic characterization of YBCO films	30
2.3 Device fabrication	33
2.3.1 Photo-Lithography	33
2.3.2 YBCO film lamination for top-bottom devices	38
2.4 Electrical Transport Measurements	39

2.5	Oxygen doping characterization	43
2.5.1	Hall measurements	43
2.5.2	Raman spectroscopy	45
2.6	Numerical simulations	49
3	Field-induced oxygen migration in YBCO films	53
3.1	Device fabrication	54
3.2	Resistive switching characteristics	56
3.3	Vertical oxygen diffusion	65
3.4	Lateral oxygen diffusion	68
3.4.1	Local evaluation of field-induced oxygen diffusion . . .	72
3.4.2	Numerical simulations	74
3.5	Conclusions	78
4	Electromigration in YBCO thin films	79
4.1	Electromigration current density (J_{em})	80
4.2	Critical current density (J_c) vs electromigration current density (J_{em})	84
4.3	Selective tuning of the oxygen content in YBCO bridges	85
4.3.1	Direct visualization of electromigration	86
4.3.2	Transport measurements	87
4.3.3	Raman experiments	91
4.3.4	Anti-electromigration process	93
4.4	Conclusions	94
5	YBCO films for neuromorphic applications	97
5.1	Device fabrication	98
5.2	Multiple gate tuning of a drain-source channel conductance .	100
5.3	Potential and depression effects in top-bottom devices . .	107
5.3.1	Effect of the applied voltage	108
5.3.2	Effect of the duration of the pulses	110
5.3.3	Effect of asymmetric voltages	111
5.4	Potential and depression effects in top-top devices	112
5.5	Conclusions	114
	General conclusions	117
	Future work	119
	List of abbreviations	121

List of publications	125
List of contributors	127
Bibliography	129

Chapter 1

Introduction

Strongly correlated complex oxides are oxide compounds with properties and electronic behavior that arise from the complex interplay between charge spin, orbital and lattice degrees of freedom. They have been widely studied in the last decades due to the high variety of outstanding properties they show, such as multiferroicity, ferroelectricity, colossal magnetoresistance, metal-insulator transitions or high temperature superconductivity. Beyond fundamental interest, correlated behavior also provides a way to realize novel electronic devices in which their functionality can be tuned by using an external input. For example, reversibly switching between an insulating and metallic phase using an applied electric field can form the basis for memory or logic applications. Along this thesis we are going to study field induced metal insulating transition (MIT) in high temperature cuprates and the potentiality of this transition to induce resistive switching effects or modulate the superconducting order parameter.

In this introductory section we will provide the basic principles of MIT in strongly correlated oxides and the associated phenomena we aim to study; resistive switching and modulation of the superconducting state, and the possible mechanisms involved. We will also introduce potential applications of this effects.

1.1 Metal-insulator transition in strongly correlated materials

A metal-insulator transition (MIT) is a change in a material from metallic to insulator state or vice-versa. This transition can be generated through different external parameters like temperature, pressure or electromagnetic

field for example. At a finite temperature, the MIT can provide useful functions, enabling ultrafast switching of versatile physical properties, not only electrical conductivity, but also other transport, magnetic and optical properties [1].

The first and simplest definition of both metals and insulators, and the transition between them did not take into account any interaction between electrons and was based on the filling of the electronic bands at zero temperature. In the case of insulators, the highest band with electrons is completely filled whereas it is partially filled in the case of metals. A simplified electronic band structure is shown in figure 1.1. Later in the 30's it was discovered that the insulators with small energy gap could become conducting if electrons are thermally activated, and also that a big quantity of transition-metal oxides with a partially filled d-electron band behaved like insulators [2]. Mott and Peierls [3] suggested the possible role of the electronic correlation due to the Coulomb repulsion between electrons. Closely related to this, the first MIT reported was found in the 1940's in magnetite, a mineral rock composed of oxide iron. It is a temperature-induced transition from metal to insulator that generates changes in the structure and the physical properties, known as Verwey transition [4].

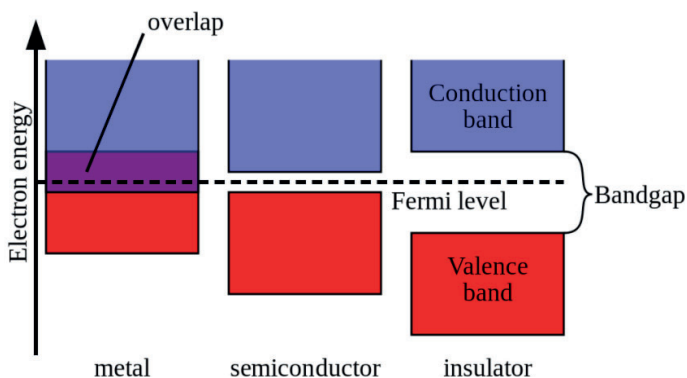


FIGURE 1.1: Simplified electronic band structure from [5].

Mott studies were particularly important [6, 7] in the field, explaining the unexpected insulating behavior in some materials through an electron-electron interaction. Supposing no interaction there could be two electrons on each orbital, one spin up and one spin down. Mott postulated that if there is electron-electron interaction, the Coulomb repulsive force between

them would split the band in two. If the lower one is filled and the upper one is empty, the insulator behavior would be explained (see figure 1.2).

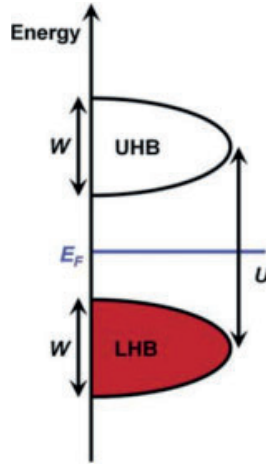


FIGURE 1.2: Splitting of a normal band into upper and lower Hubbard band due to electron correlations.

In the Hubbard model [8–10], the electron filling and the ratio U/W between the Coulomb repulsion energy U and the electron band width W , both turn out to be very critical parameters that can drive metal-insulator transitions.

The Mott metal-insulator transitions induced by tuning relative magnitude of the Coulomb Repulsion U to bandwidth W at fixed band-filling (half-filling), is called bandwidth controlled metal-insulator transition (BC-MIT). One example of this is applying stress on a Mott insulator to change the atom spacing and consequently bandwidth to induce a metal-insulator transition without changing the carrier density.

The other way to induce a metal-insulator transition in a correlated electron system is to change the band-filling (chemical doping, electrostatic modulation). This kind of transition controlled by carrier density is called filling controlled metal-insulator transition (FC-MIT). In other words, to dope the upper (lower) Hubbard band with electrons (holes). At exact half-filling, electrons cannot hop to another site due to Coulomb repulsion and all the sites are singly occupied. If holes are doped into the insulator, however, some atom sites become unoccupied and the nearby

electrons could move freely onto this unoccupied site, because the total energy is the same before and after the hopping. The original insulator now becomes metallic. Similarly, doping electrons into the insulator also makes electrons to hop freely through those unoccupied atom sites.

These two different routes to a metal-insulator transition in a correlated electron system are depicted in figure 1.3.

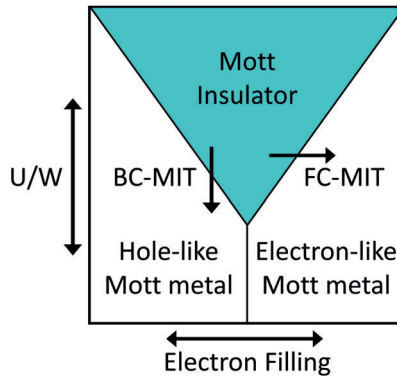


FIGURE 1.3: Phase diagram of a Mott-Hubbard system as a function of electron filling and U/W . Two routes of transitioning across the metal-insulator boundary are depicted. The metallic state in the shaded region is highly sensitive to disorder-induced localization, reproduced from [11].

It should be noted, however, that the precise details of any real system are vastly more complex than the simple Hubbard Model. Spin, orbital, and lattice interactions can all add additional degrees of freedom to the system that greatly complicate real situations. An excellent discussion of this topic can be found in reference [11].

In transition metal oxides like manganites or cuprates the 3d band splits in two following the Hubbard model, but the 2p band of the oxygen also plays a role and depending on its position two different scenarios arise. If the 2p band is below the lower Hubbard the charge carriers jump from the lower Hubbard band to the upper Hubbard band. These materials are called Mott-Hubbard insulators and some examples are cuprates like $YBa_2Cu_3O_{7-\delta}$ (YBCO) and manganites like $La_{1-x}Sr_xMnO_3$ (LSMO). On the other hand, if the 2p band of the oxygen is between the lower and

upper Hubbard bands, the charge carriers jump from the lower Hubbard band to the oxygen 2p band and from this, to the upper Hubbard band (see figure 1.4). These other materials are called Charge-transfer insulators and nickelates like $NdNiO_2$ (NNO) are an example. In both cases, a MIT is induced and can be tuned either by controlling the bandwidth or the band-filling.

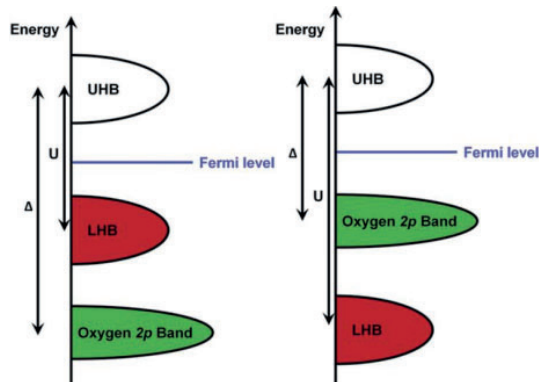


FIGURE 1.4: Mott-Hubbard insulator: oxygen p-band lies under the lower Hubbard band (left). Charge-transfer insulator: oxygen p-band between the lower Hubbard band and upper Hubbard band (right).

In the high-temperature superconductor YBCO, oxygen vacancies (V_{O^-}) control the carrier concentration, its critical current density and transition temperature. Therefore, the MIT in YBCO is band filling controlled and by the application of a gate voltage, oxygen vacancies can be redistributed within a YBCO channel, locally changing its doping level and thereby its resistance.

1.2 Resistive Switching (RS)

Memory devices can be divided in two groups: Flash memories and Dynamic random-access memories (DRAM). Flash memories are based on charge trapping effects and show large retention times (the order of 10 years). They are non-volatile but their operation times (writing and

reading) are very long (tenths of milliseconds) and show poor endurance (thousands of cycles). These characteristics make them appropriate for long-term data storage. On the other hand, DRAM memories are based on capacitance effects, with fast operation times (nanoseconds) and high endurance (millions of cycles) but very poor retention times (in the order of minutes), making them suitable for computing applications. In the last decades many efforts have been devoted to obtain a memory that gathers the best of both, that is fast operation and long retention, taking also into account the importance of lowering the consumption and the scalability to make more dense systems.

Resistive switching materials exhibit tunable resistance states (at least two) induced by an external electrical bias. A large variety of physical phenomena are known, which can in principle, accomplish such changes in resistive states. This phenomenon has been studied in many different materials like binary oxides (HfO_2 , NiO , TiO_2 , WO_3 , Va_2O_5 ,...) or more complex oxides (Ca_2RuO_4 , $Pr_{0.7}Ca_{0.3}MnO_3$, Sr_2CuO_3 ,...) [12], in order to design high-performance Resistive Random-access memories (ReRAM). These devices offer good scalability due to its simple architecture and show fast write/erase speed and long retention times, gathering the best of both flash and DRAM memories.

Strongly correlated oxides, like the already mentioned LSMO or YBCO, appear as promising materials for memory applications. In these materials a robust MIT can be induced, controlling the oxygen doping by means of an electric field, obtaining very significant resistance changes in a reversible and non-volatile way by applying short voltage pulses [13–15].

Other memory technologies that are being studied are Ferroelectric-RAM (FeRAM), Magnetoresistive-RAM (MRAM) or Phase-Change-RAM (PCRAM).

1.2.1 Operation principles of a Resistive Switching cell

A simple picture of a Resistive Switching cell or device is a material that presents RS in between two electrodes (figure 1.5). Usually the architecture is top-bottom and the switching material is an insulator, but designs with top-top configurations and metals that can switch to insulating are also

possible.

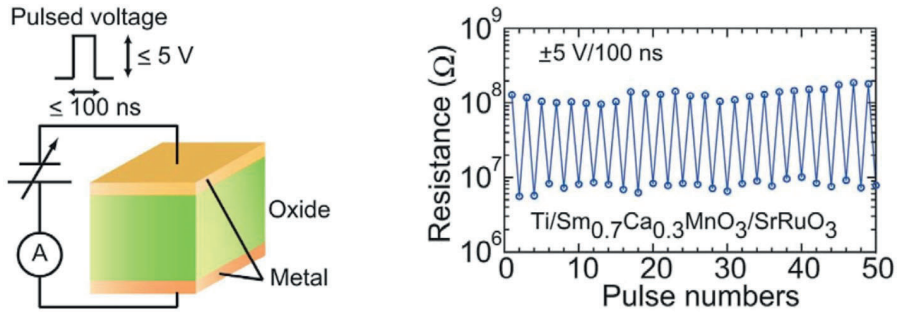


FIGURE 1.5: Diagram of a ReRAM memory cell with a capacitor-like structure (left). Reversible changes between high and low resistance by applying alternatively positive and negative pulsed voltages (taken from [16])

The material, that is usually insulating, starts in the high resistance state (HRS) or OFF state. A typical RS graph will represent the current or the resistance of the cell as a function of the applied voltage and the resulting figure is called switching loop (figure 1.6). When a suitable electric field is applied the resistance changes, becoming more conducting. This is the low resistance state (LRS) or ON state. Moreover, there can be other intermediate states depending on the material and the field applied. This OFF to ON transition is called Set. The ON state remains when the field is removed, meaning that it is a non-volatile effect. The effect can be reversibly reversed and thus switched from the LRS back to the HRS, or ON to OFF, with a reset process. Two different types of switching appear depending on these reset project: unipolar and bipolar. In the first case SET and RESET are induced depending on the amplitude of the applied field (figure 1.6 (a)). In the second case this depends on the polarity, meaning that to reverse the switching effect the opposite polarity has to be applied, and the switching is induced after reaching a certain (figure 1.6 (b) [17]). Apart from the set and reset operations, the reading operation is also relevant. It makes possible to read the state of the cell, and it usually consists on applying a very low field that do not affect the actual resistance state.

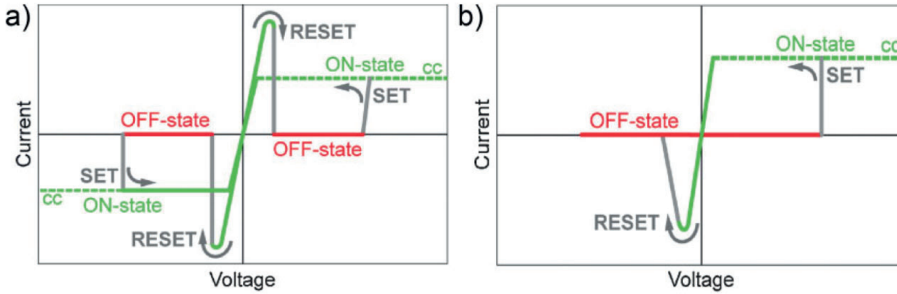


FIGURE 1.6: (a) Unipolar and (b) bipolar RS switching loops (taken from [17]).

1.2.2 Resistive Switching mechanisms

Diverse mechanisms are described to explain the RS effect in different materials, although the microscopic models responsible for it are not clearly understood in many cases. One example would be controlling the tunnelling current in a junction by manipulating the direction of the polarization of a ferroelectric domain [18]. Another example would be the electrochemical metallization mechanism (ECM) in which the mobile cations of an active metal electrode creates or "dissolves" a metallic filament by travelling along a solid electrolyte [19]. In our work we are going to focus on the valence change mechanism (VCM), present in transition metal oxides, which can be produced through different effects. In some cases the transition is induced by means of pure electrostatic doping [20, 21] or charge trapping at impurities and interfaces [22, 23]. But in most of the explored systems, as in the ones studied in this Thesis, the valence change is induced by a migration of oxygen vacancies, with higher mobility than cations [16, 17]. This mechanism is bipolar because reduction and oxidation happen with opposite polarities.

Regarding the localization of the switching event two scenarios are usually distinguished (see figure 1.7). One is the filamentary, in which the oxygen vacancies form a conductive filament that connects the two metallic electrodes. The second is the interface scenario, in which oxygen vacancies are distributed along the interface between the material and the electrode, and the modulation of a Schottky barrier determines the conductivity of the device [16]. In both cases, some limitations arise due to the strong localization of the switching event. In addition, in the case of

filamentary-type resistive switching there is no control of the localization of the formation and rupture of the filament thus resulting in a high cycle-to-cycle and cell-to-cell variability. Other problems can appear, derived from the apparition of leakage currents and the high non-linearity of the electric field in the insulating material.

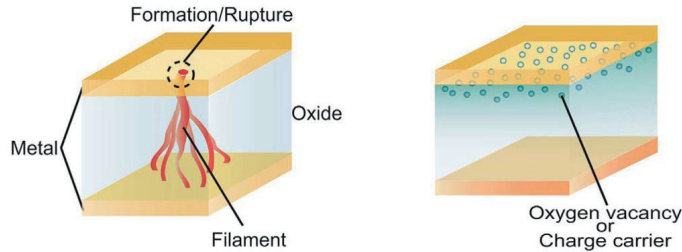


FIGURE 1.7: Sketch of two possible scenarios for the localization of the resistive switching effect. (a) Filamentary-like switching effect. (b) Interfacial-like switching effect. Extracted from [16].

In this work we will explore YBCO, a strongly correlated material which is metallic in its initial phase at room temperature. This material presents a switching performance particularly appealing since it offers the possibility of homogeneously modulate the diffusion of oxygen vacancies (and induce a metal-insulating transition), not in confined filaments or at the interface, but in a volumetric way (volumic-like switching effect) (figure 1.8) [14, 15, 24, 25]. Volumic-like switching provides an homogeneous and robust effect which may be used to conceive multi-terminal transistor devices with valuable insight for the design of memory or logic devices with extra flexibility.

We will design, fabricate and study devices made of YBCO with different architectures in order to provide new knowledge on the phenomena governing the field-induced oxygen diffusion occurring in this material and the associated metal-insulating transition. We will also explore their possible application as memristive memory devices or to implement more complex neuromorphic applications. The particular volumic nature of the phenomenon will be exploited to fabricate not only the typical devices in top-bottom configuration but also systems with multiple electrodes in top-top configuration, which offer extra flexibility to implement complex

functionalities. As we will explain in section 1.4 we will specially investigate its possible use in neuromorphic computing, where the performance of many different memristor systems is being studied.

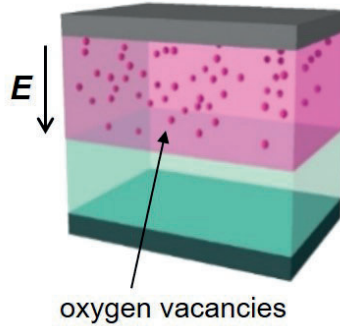


FIGURE 1.8: Sketch of volumic-like Resistive Switching in a metallic perovskite oxide.

1.3 Strongly correlated superconducting oxides

Superconductivity is a manifestation of a collective quantum state on a macroscopic scale and represents one of the most exotic and exciting phenomena in modern physics. The superconducting phenomenon is essentially characterized by the suppression of the electrical resistance of the material below a certain temperature (critical temperature, (T_c), see figure 1.9), the expulsion of the magnetic field (Meissner effect) and the quantification of magnetic flux.

The large variety of potential technological applications of superconducting materials is linked to the exploitation of one or more of their exceptional physical properties (magnetic resonance devices, magnets in large scientific facilities, filters in systems of communication or ultra-sensitive SQUID detectors, quantum computing, among others). Cryogenic costs however, are one of the main drawbacks of superconducting materials towards application.

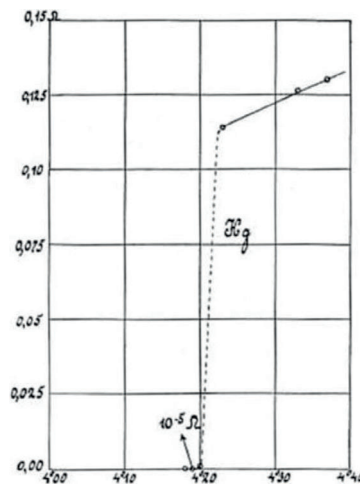


FIGURE 1.9: Historic plot of resistance versus temperature of the first measured superconducting transition (from [26]).

1.3.1 High-Temperature superconductors (HTS)

The discovery of High-Temperature superconductors in 1986 [27] provided a huge breakthrough in this sense since they could be used at temperatures above the boiling point of liquid nitrogen (77K), strongly reducing the associated cooling costs [28]. Among all family of cuprate high-temperature superconductors, YBCO is one of the most explored due to its high T_c value (93 K) and good superconducting performances up to high magnetic fields.

High-Temperature superconductors are type II superconductors in which most of their phase diagram is governed by the presence of vortices (quantum flux lines that penetrate in the material by applying a magnetic field). Vortex are very small entities (micro-, nano-metric size) formed by a core of normal electrons surrounded by super-currents. If an electric current is applied (or current density \vec{J}), along with the present magnetic field (\vec{B}), vortex will feel a Lorentz like Force which density follows the formula $\vec{F}_L = \vec{J} \times \vec{B}$, leading to energy dissipation. Vortex motion determines the maximum loss-less current that may be applied to the superconductor (the critical current density J_c). There has been very active research on how to manipulate vortices through pinning sites (non-superconducting regions), either to fix them in the material and maximize J_c [29–32] or control their motion for applications based on fluxonic concepts [33, 34].

Reversible local tuning of MIT in cuprates brings opportunities to generate insulating regions at local scale which could be used as re-configurable pinning landscapes.

$YBa_2Cu_3O_{7-\delta}$ (YBCO) is a strongly correlated high-temperature superconductor which is particularly appealing for resistive switching applications since its physical properties strongly depend on the oxygen doping. It has a triple perovskite structure formed by a sequence of stacked layers along the c -axis $CuO-BaO-CuO_2-Y-CuO_2-BaO$ (Figure 1.10). The CuO_2 planes ($a-b$ planes) are particularly important since it is there where the transport of charge carriers and superconductivity takes place. The CuO_x chains are known as copper-oxide chains and they act as charge reservoirs. Their oxygen content can vary from 0 to 1, determining its stoichiometry and crystallographic structure. Its *Goldsmith tolerance factor* is lower than 1 ($TF < 1$), and hence the octahedra of oxygen atoms surrounding the Cu cations are distorted generating a reduction of the superexchange angle (Cu-O-Cu). This has an important influence in the conducting and magnetic properties, originated in the superposition of the orbitals 3d in the Cu cation and the orbitals 2p in the O anion.

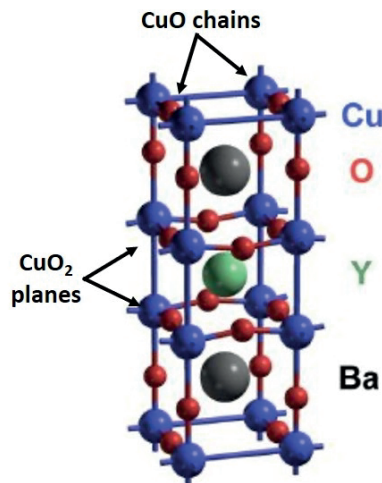


FIGURE 1.10: YBCO crystal structure, adapted from [35]

As the oxygen content increases the CuO_2 planes are doped with holes due to a charge transfer between them. Oxygen doping determines its magnetic and electronic properties following a universal phase diagram

common to all cuprate superconductors (Figure 1.11).

Starting with $\delta=1$, meaning no oxygen in the chains, one has the $YBa_2Cu_3O_6$ phase. In this case the material is an antiferromagnetic Mott insulator, with tetragonal P4/mmm structure. When increasing the oxygen content in the chains the hole doping level of the CuO_2 planes increases and, at a certain doping, a MIT takes place. As a result the YBCO becomes a superconducting metal with an orthorhombic Pmmm structure with a critical temperature (T_c) following a superconducting dome with roughly parabolic dependence. The T_c of YBCO depends on the oxygen content (or hole doping) being around 93K when optimally doped.

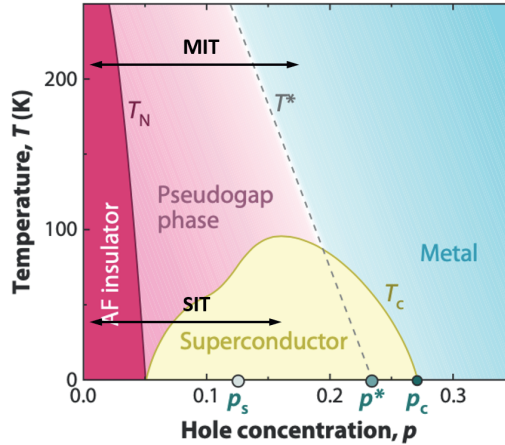


FIGURE 1.11: Phase diagram of high-temperature superconducting cuprates, indicating the two possible phase transitions that can be induced by tuning the hole doping, MIT and SIT (from [36]).

Superconductivity and the possibility of inducing a MIT through the modulation of the carrier concentration can be exploited at low temperature (below (T_c)), to produce a superconductor to insulator transition (SIT).

Another interesting property of YBCO is that its oxygen diffusion and electronic properties are highly anisotropic due to its layered structure. In particular oxygen diffusion through the $a - b$ planes can be six orders of magnitude higher than along the c -axis [37]. This can be interesting in

terms of device fabrication, since top-top configuration devices may have faster operation times than the commonly used ones with top-bottom configuration.

1.3.2 Superconductor-insulator transition (SIT)

A superconductor to insulator transition (SIT) is a quantum phase transition that implicates a radical change in the behavior of the electrons, breaking their quantum-collective coherency and thus their superconducting properties. This phenomenon has been explored in the last decades, trying to elucidate how the superconducting order parameter changes as a response to a variation of an external parameter in the Hamiltonian. It has been mainly studied in 2D materials, ultrathin films consisting of a single layer of atoms, induced by thickness modulation [38], disorder and magnetic field [39, 40], strain [41] or electrostatic doping [42].

In the case of cuprate superconductors, SIT has been induced either reducing the thickness to few nanometers in LaSrCuO (LSCO) [43] or using electrostatic doping effects in LSCO [44], BiSrCaCuO (BSCCO) [45] or YBCO [46]. In all these studies, ultrathin films and large electric fields are needed to obtain significant MIT changes which is not ideal for many practical applications.

In this work we will explore the possibility of inducing the superconductor-insulator transition in YBCO thin films by means of an electro-chemical oxygen doping, achieving a good control of the switching region through the thickness (up to hundreds of nm), substantially larger than the ones modulated in pure electrostatic experiments. Figure 1.11 schematically shows the complex phase diagram of cuprate superconductors and the transitions that may be induced at high temperatures (MIT) and below the critical temperature (SIT).

Therefore, a fine control of field-induced oxygen doping can be exploited as a practical tool for the investigation of complex phases appearing in the cuprates phase diagram, and could also be extended to other strongly correlated systems.

1.4 Neuromorphic Computing

Digital computers, based on CMOS technologies, can process a big quantity of data with high speed and precision. However, compared to the brain, they still cannot approach a comparable performance considering cognitive functions such as perception, recognition, and classification. Brain shows much lower power consumption, adaptive learning and intrinsically massive parallel processing. Current computers follow a typical Von Neumann architecture (see figure 1.12), where the memory and the computing unit are separated. The communication channel between both is smaller than the memory itself so it is a bottleneck that slows the speed and increases the power consumption. Biological brains on the contrary, operate with a massively parallel architecture connecting multiple low-power computing elements (neurons) with adaptive memory elements (synapses). Neuromorphic computing aims to implement the brain structure and operation in computational systems which can dramatically outperform speed and power efficiency of conventional digital computing on many tasks involving cognitive functions [47, 48].

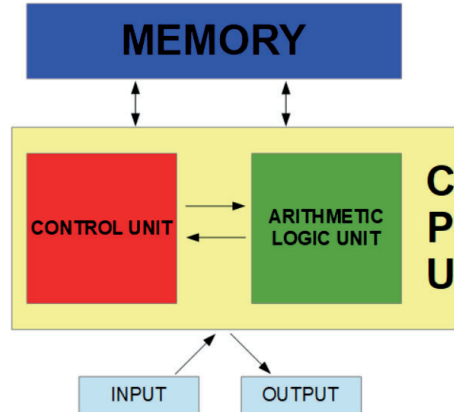


FIGURE 1.12: Basic diagram of the Von Neumann architecture.

Although certain degree of stable learning can be achieved with digital logic using binary weights [49, 50], the design of computational systems mimicking the analog brain work is completely unfeasible by conventional

digital logic. Thus, the development of novel functional materials, and individual device components able to resemble the properties of neuronal systems, are mandatory to bring a revolutionary technological leap toward the implementation of a fully neuromorphic computer.

While the building block of digital computers is the transistor, the two basic blocks of neuromorphic computing are neurons and synapses (see figure 1.13).

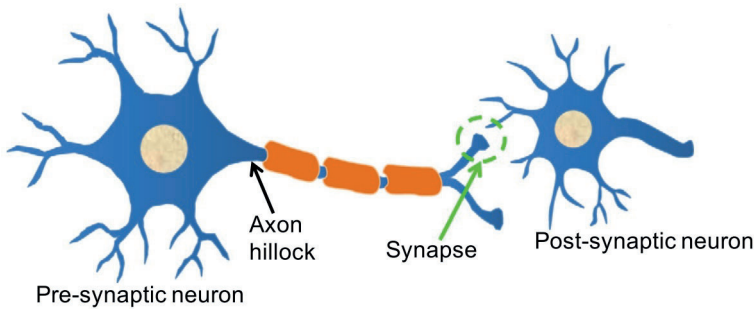


FIGURE 1.13: Sketch of two neurons and the synapse, which is the connection between them adapted from [51].

Each biological neuron consists of a dendritic tree for taking inputs from other neurons, a body or soma, which basically performs charge summation, and an output, the axon. Incoming axon lines form a connection to other neurons through synapses which locally store memory in form of synaptic strength.

Neuron functionalities are characterized by a process of charge accumulation at a membrane potential as input spikes received from post-synaptic neurons. They accumulate the signal as charge at the membrane until a certain threshold is reached above which the neuron fires and resets, emitting an output spike. The firing rate increases with the intensity of the stimulus, directly related to the amplitude and frequency of the input spikes. This whole process is known as *leaky, integrate and fire* (LIF) (see figure 1.14). In order to emulate neuron functionalities signal may be accumulated in a volatile way. Promising results have been achieved by using graphene oxide [52, 53] or silicon oxide RRAM cells [54], Mott insulators [55] and spintronic devices [56].

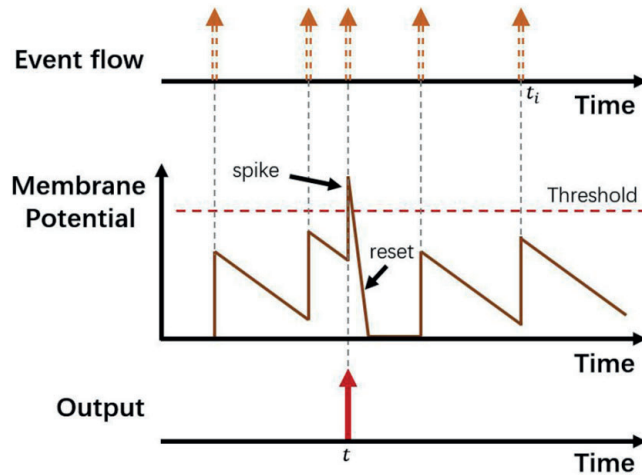


FIGURE 1.14: Schematic representation of a leaky, integrate and fire (LIF) process. Extracted from [57].

Synapse functionalities are characterized by the synapse plasticity, which is the ability of learning by increasing or decreasing the weight depending on the input signals. A representative algorithm for synaptic learning process is called spike-timing dependent plasticity (STDP), where synaptic weights are either potentiated or depressed depending on the order and time delay between pre-synaptic neuron spikes (pre-spike) and post-synaptic neuron spikes (post-spike) [58]. According to the algorithm the synaptic weight is potentiated (or strengthened) if the pre-spike happens before the post-spike ($\Delta t > 0$), which is called long-term potentiation (LTP). On the other hand, the synaptic weight is depressed (or weakened) if the pre-spike happens after the post-spike ($\Delta t < 0$), which is called long-term depression (LTD) (see figure 1.15).

This learning process is summarized with the Hebb's learning rule “neurons that fire together wire together”, meaning that when two neurons are active in response to the same event the synaptic connection should be strong [60].

Different memristors presenting resistive switching have been proposed to emulate the behavior of a synapse with promising results [51, 61–63].

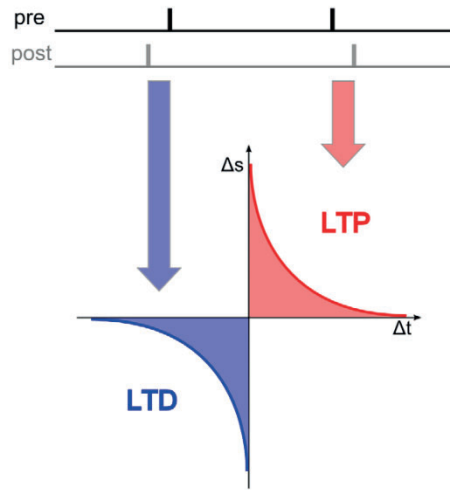


FIGURE 1.15: Schematic representation of spike-timing-dependent plasticity (STDP): the synaptic weight increases $\Delta s > 0$ when a post-synaptic potential takes places after a pre-synaptic spike $\Delta t > 0$ (long-term potentiation, LTP) and decreases $\Delta s < 0$ when a post-synaptic potential takes place before a pre-synaptic spike $\Delta t < 0$ (long-term depression, LTD).

Extracted from [59].

Their conductance or resistance¹ can be continuously modified by an input signal, which is usually either a voltage or a current. The inducted states are non-volatile, meaning that the resistance state will be preserved even after removing the input signal (ideally with long retention times). Different intermediate states can be achieved by controlling the input signal (value and number of pulses), which is required to imply learning capabilities and emulate STDP. Due to their simple architecture, they are also interesting in terms of scalability and density to be integrated in neuromorphic networks. However, efficient and accurate training of synaptic weight needs not only conductance potentiation of depression behaviours, but also a high degree of linearity of the conductance with the number of pulses. Although there has been clear progress in improving the linearity of synaptic devices by pulse modulation or material engineering (figure 1.16), much more effort

¹The terms conductance (G) and resistance (R) are reciprocal, since $G=1/R$, so their variations are analogous. Both of them are commonly used in the bibliography of this field of research and so will be in this chapter.

is still needed to find materials and structures that satisfy all the requirements of synaptic devices (symmetrical and linear conductance change under constant pulse application, high enough on-off ratio, and sufficient retention and endurance).

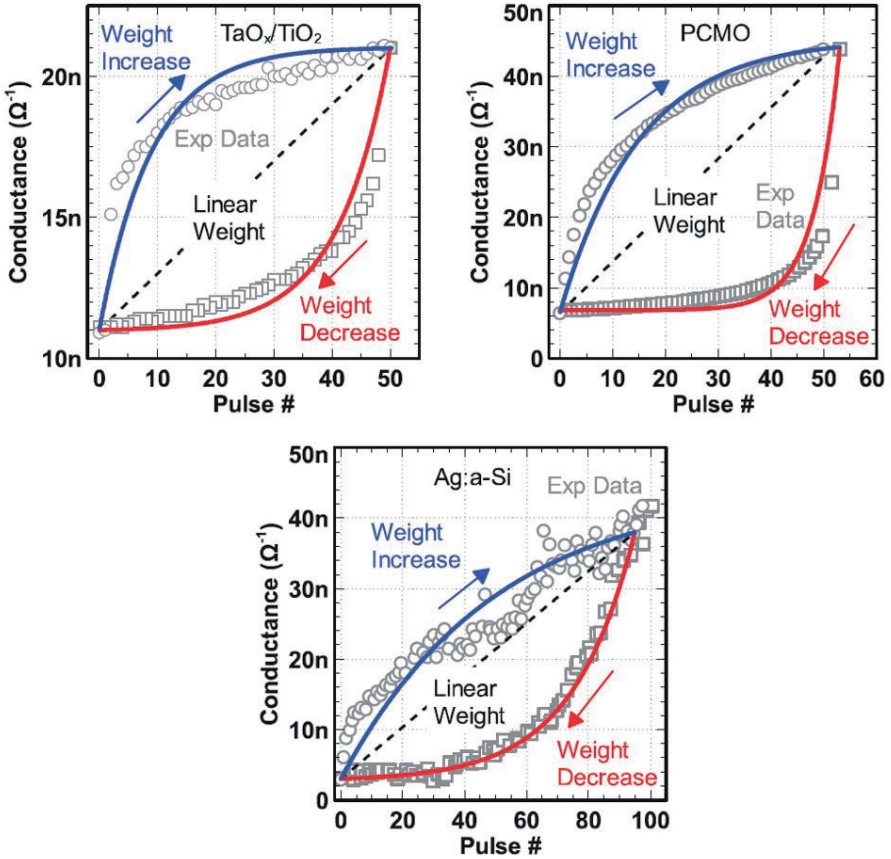


FIGURE 1.16: Synaptic weight potentiation and depression with pulses of positive and negative voltage respectively, in three different cells, showing different linearity and symmetry of the conductance change. Extracted from [64].

In this work, the potential of using YBCO for neuromorphic applications, in particular to mimic a synapse behavior with 2-terminal (2T) and multi-terminal devices, will be considered. We will exploit the possibilities of the resistive switching in this material to induce non-volatile resistance states and by tuning the applied field reach different intermediate states allowing

to emulate the learning capabilities of a synapse. The volumic nature of the effect in this material offers more robustness but also the possibility of creating 3-terminal (3T) or multi-terminal transistor-like devices to implement more complex functionalities.

While 2T devices suffer from a write disturbance problem because the writing and reading occur in the same direction, the separation of read and write in 3T structures not only improves the immunity to data disturbance but allows concurrent read and write operations [65]. On the other hand, 3T devices provide more flexibility to produce more complex cognitive processes such as heterosynaptic plasticity [66–69].

Chapter 2

Experimental methodology

This chapter describes all the experimental methodology carried out along this thesis. This includes the techniques used for the growth of the epitaxial YBCO films, its structural characterization, the fabrication of the devices and other techniques used to characterize certain local properties of the material after the resistive switching and electromigration processes.

2.1 Sample growth

When it comes to thin film growth, different physical and chemical deposition techniques are used. Some of the most common are atomic layer deposition (ALD), molecular beam epitaxy (MBE), pulsed laser deposition (PLD), chemical solution deposition (CSD) and sputtering.

In our case, we used PLD and CSD to grown (001) epitaxial YBCO thin films on $5 \times 5 \text{ mm}^2$ $SrTiO_3$ (STO) and $LaAlO_3$ (LAO) single crystal substrates. The films obtained from both techniques show very good physical properties, such as a critical temperature T_c close to 90 K and critical current density at 77 K $J_c(77K) = 3\text{-}5 \text{ MA/cm}^{-2}$ [70, 71]. We used optimally doped films of different thicknesses (from 50 to 250 nanometers). No major differences were obtained on the switching performance depending on the growing process so we used both indistinctly during the thesis.

2.1.1 Substrates

Both PLD and CSD techniques have a common first step, the selection and preparation of the substrates. The function of a substrate is giving mechanical support but it also plays an important role in the nucleation

and growth of the YBCO thin films, determining their crystalline structure and physical properties. Therefore, to obtain a good epitaxial growth the selected substrates have to have the same crystal structure as the material to be grown, in our case a perovskite structure. Moreover, small mismatch between their lattice parameters is also needed. We used STO and LAO with orientation (001) and dimensions 5 x 5 x 0.5 mm from Crystec, meeting all the criteria for a good epitaxial growth.

For both STO and LAO we followed a two-step process to prepare our substrates before any growth process. First, we clean them using an ultrasonic bath, starting with acetone and then with methanol, 2 minutes with each solvent. This will remove possible adsorbants in the surface producing no structural damage. Afterwards we do a thermal treatment to get atomically flat substrates with terraces. This annealing consists on putting the substrates in an alumina ceramic crucible inside of a quartz tube placed in a tubular furnace for 5 hours at 900°C with a constant O₂ flux of 0.6 l/min, using heating and cooling ramps of 15°C/min and 10°C/min respectively.

The results of this two-step process has been proved to fulfil the requirements to obtain YBCO thin films with good structural and transport properties, and high reproducibility.

2.1.2 Pulsed Laser Deposition (PLD)

The use of the PLD technique for YBCO thin film growth has been studied for almost 30 years [70, 72, 73], having good results in scaling the process to grow kilometeric second generation HTS coated conductors [74–76]. It has been also studied to enhance vortex pinning [77–79], which can be useful for some applications.

Pulse laser deposition (PLD) is a kind of physical vapour deposition in which a laser ablates a ceramic target, made of the material to be grown, creating a plasma plume that is deposited in an empty substrate. The material will grow mainly adopting the structure of the substrate. The properties of the film are determined by the composition of the target and several parameters of the process. The YBCO target and the PLD parameters used to grow the films (vacuum conditions, distance target-substrate, laser

energy, rate, or substrate temperature) were optimized within the group to obtain high-quality films.

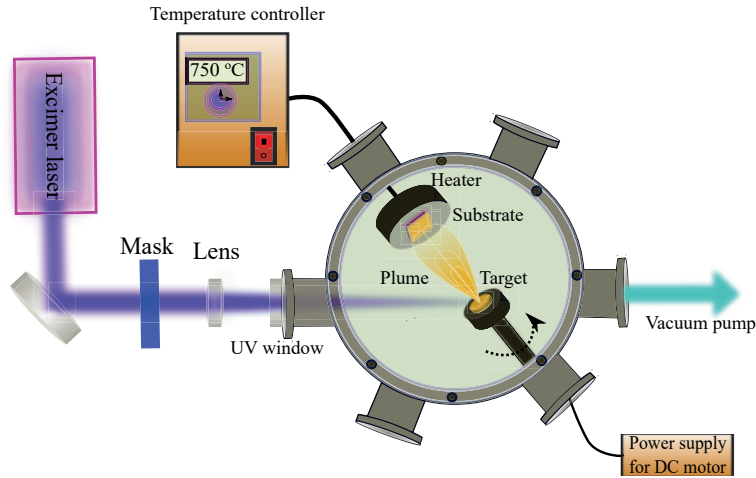


FIGURE 2.1: Sketch of the PLD setup at ICMAB, courtesy of Dr. Mengdi Qian.

The previously prepared substrate is placed exactly in front of the ceramic YBCO target at a distance of 52.5mm, inside of a vacuum chamber (figure 2.1). The substrate is heated up to 800°C in a partial pressure of 0.3 mbar of oxygen to guarantee phase stability. This ambient gas also reduces the kinetic energy of the particles of the plume and favours a proper deposition. The laser beam enters the chamber through a UV window and is focused on the target using a lens, getting a spot area between 1 and 2 mm². The energy of the laser is set so the fluence (energy per area unit) is 2 J/cm². The frequency of pulses is 5 Hz and the number of pulses will depend on the the expected thickness. From a previous calibration we got a linear dependence between the number of pulses and the thickness, 26 pulses per nanometer, valid at least for thicknesses between 10 and 250 nm. When growth is finished we set a cooling ramp from 800°C to 600°C with a rate of 15K/min and with a partial pressure of 400 mbar of oxygen. At this temperature the incorporation of oxygen into the YBCO is favoured and we get well oxygenated, optimally-doped, samples. After this the sample is cooled directly from 600°C to room temperature with ambient pressure (figure 2.2).

In case we aim to obtain under-doped films, the first ramp is skipped and the sample is directly cooled from 800°C to room temperature at

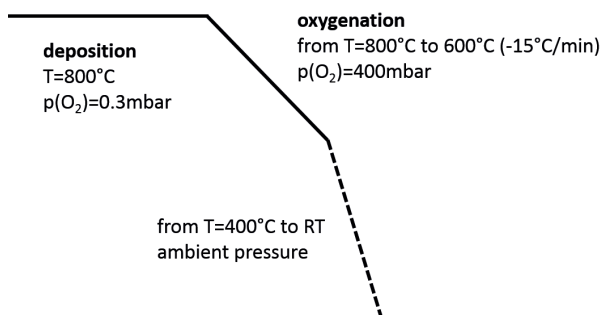


FIGURE 2.2: Profile of the PLD growth process.

ambient pressure. Another way to change the initial oxygen doping is by heating an optimally-doped sample up to 600°C in air. Depending on the time spent in this conditions we can control the oxygen content of our films.

Some advantages of the PLD technique are the simplicity and control of the process and the direct stoichiometric transfer from the target to the film. With this technique we could obtain samples from 50nm to 200nm with good physical properties. Sample growth was performed by the technicians of the PLD facilities at the Thin Film Laboratory at ICMAB.

2.1.3 Chemical solution deposition (CSD)

Chemical solution deposition (CSD) is a multi-step deposition technique that stands out due its simplicity, low cost, versatility and scalability, when it comes to epitaxial thin film growth [76, 80, 81], with great success in obtaining ferroelectric [82] and ferromagnetic structures [83, 84] and also superconducting coated conductors (CCs) [85]. A sketch of the steps of the process is shown in figure 2.3. In the case of CSD, I grew all the YBCO samples used in the Thesis, following the standard growth procedure optimized within the group.

The first step is the preparation of the stoichiometric solution, containing the precursors and solvents suitable for the material to be grown. The salts containing the final species have to keep the correct stoichiometric proportion according to the YBCO composition. The molar concentration of the solution will determine the thickness of the film, so we used several diluted versions of the original solution to be able to grow with different

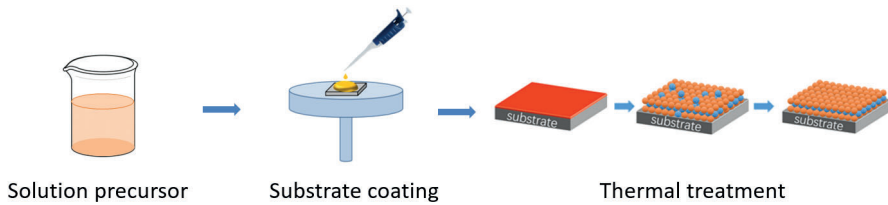


FIGURE 2.3: Sketch of a typical CSD growth process, courtesy of Dr. Hailin Wang.

thicknesses. The precursor solution was prepared by the group technicians and consist on a metal-organic solution of trifluoroacetate (TFA) salts [86, 87].

The second step is the deposition of the solution. It is carried out in a laboratory with controlled humidity and inside of a fume hood, where low humidity, below 10% is guaranteed. Using a special syringe with micrometric precision we deposit a volume of 15 micro-liter of the solution on a previously treated substrate, placed in the sample holder of a spin-coating equipment. The parameters of the spinning were total spinning time of 2 minutes, speed of 6000 revolutions per minute (rpm) and acceleration time of 1s (the time spent to reach the spinning speed). After this we put the substrate on a hot plate with a temperature of 70°C for 10 minutes. This will evaporate the solvents.

The third step is thermal treatment known as pyrolysis that happens at low temperatures, 310°C in this case (see figure 2.4). The substrate is placed in a quartz tube inside of a tubular furnace with oxygen flow of 0.075 L/min. During the heating, from 110°C on, water vapour is also present to guarantee a proper content of Cu. The water vapour flow is stopped after the pyrolysis takes place, in the cooling down ramp. In this step the organic species are decomposed and eliminated, and only intermediate phases of $Ba_{1-x}Y_xF_{2+x}$ and CuO remain.

The fourth and final step is a second thermal treatment at higher temperatures, at which the oxide crystallizes. It is illustrated in figure 2.5. We introduce the pyrolysed film again in a quartz tube inside of a tubular furnace, in dry mixed atmosphere of O_2 and N_2 being the total pressure

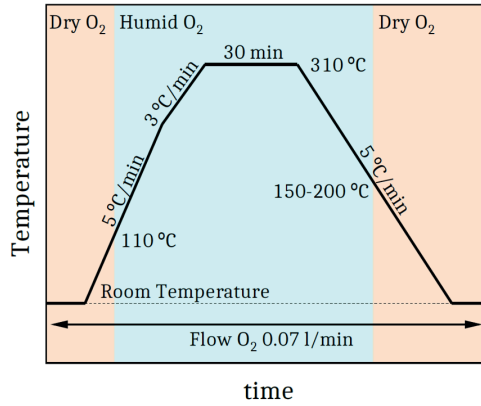


FIGURE 2.4: Thermal profile of the pyrolysis process.

1bar and partial pressure of oxygen $p(\text{O}_2)$ 0.2 mbar. The temperature is increased until the growth temperature (800°C) setting a humid atmosphere to decompose the BaF_2 and remove the fluorine. For the YBCO to crystallize we do a dwell at the growth temperature. Afterwards the temperature is decreased, in again a dry atmosphere of O_2 and N_2 changing to just O_2 at 600°C . The film is finally oxygenated with a high oxygen flow doing a dwell at 450°C , the oxygenation temperature. The oxygen enters the YBCO structure, that changes from tetragonal to orthorhombic, getting a superconducting YBCO thin film. Finally we cool the system to room temperature.

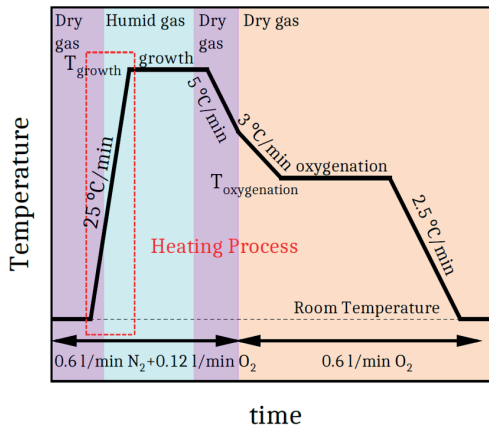


FIGURE 2.5: Thermal profile of the growth process.

2.2 Basic structural and physical characterization

After the YBCO film growth, we performed a basic characterization to determine the composition, crystal orientation, thickness, transport and magnetic properties of the films.

2.2.1 Composition and structural analysis

X-ray diffraction measurements were used to characterize the structure of our samples after growth, in their pristine state. The wavelength of the X-ray is of the same order of magnitude as the interatomic distances of the crystal structures that we are going to study, between 0.1 and 100 Å. The incident radiation is scattered by the electrons in the atoms of the structure. The diffraction peaks generated by the constructive interference can be measured at certain angles θ , the ones fulfilling the Bragg condition $n\lambda = 2d\sin\theta$ [88], being λ the wavelength of the incident light, n the diffraction order, and d the distance between crystal planes. The result is an X-ray diffraction pattern, characteristic of each material.

This measurements were performed by technicians of the X-ray Diffraction Laboratory at ICMAB, using a $\theta - 2\theta$ configuration (figure 2.6), using an angle step of 0.02° from 10° to 80° and Cu K_α radiation with wavelength 1.540560 Å.

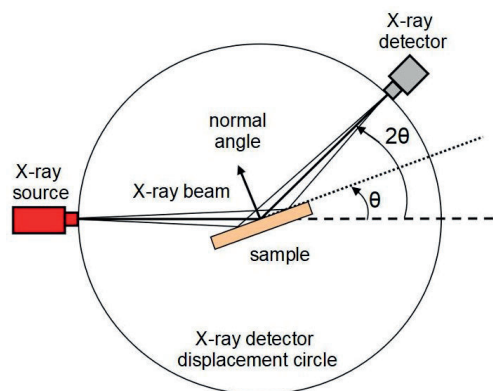


FIGURE 2.6: Sketch illustrating the configuration of the XRD measurements adapted from [89].

In the case of the samples grown by PLD their composition depends on the composition of the target and the growth conditions. Since the growth process is standardised and we use always the same target, we do not need to check the composition of every sample. We got the expected results when we did it. On the other hand, in the case of the samples grown by CSD their composition depends on the composition of the stoichiometric solution, so a X-ray diffraction measurement was performed when the solution was changed.

Regarding the epitaxial growth, we used θ - 2θ X-ray diffraction measurements from 10° to 80° to detect the crystal orientation. In all the samples only the contributions of the (00l) reflections of YBCO layer and the LAO substrate were detected, with no secondary or polycrystalline phases, indicating the epitaxial growth of the films (see figure 2.7).

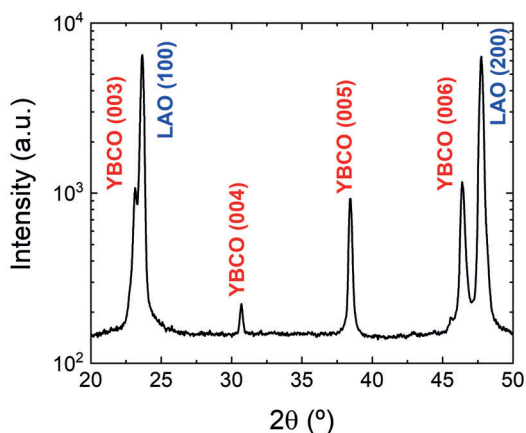


FIGURE 2.7: $\theta - 2\theta$ scan of a 250 nm YBCO epitaxial film grown on LAO substrate.

2.2.2 Measurement of thin film thickness

The thickness of the samples determines the geometry of our devices so it can be a crucial parameter in the analysis of the results.

The thickness of the films grown by PLD depends on the parameters of the deposition. In our case growing parameters were not varied to

guarantee epitaxial growth and optimal properties so thickness is proportional to the number of pulses. We used previous calibration performed in the group to determine the final thickness required. Regarding the samples grown by CSD, we also used the same growing parameters and the thickness is determined by the concentration of the solution with a linear dependence also calibrated.

Sample thickness for both PLD and CSD films was checked periodically to confirm the calibration parameters. Several techniques can be used to determine the film thickness: X-Ray reflectometry (XRR) [90], atomic force microscopy (AFM) or profilometry. We used profilometry which was able to accurately measure the range of thicknesses we used and was a very accessible equipment in our lab.

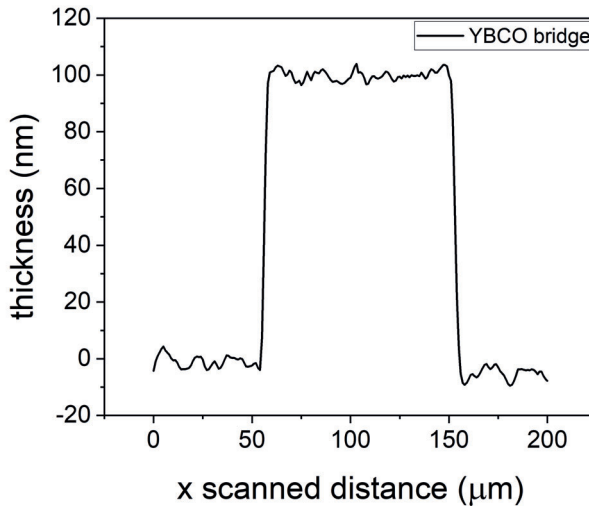


FIGURE 2.8: Profilometry scan of a bridge of a 100 μm wide in a 100 nm thick YBCO sample.

Since the thin film covers the whole surface of the substrate we need an etched part of the sample to measure the thickness. We can do this etching with some lines previously lithographed in a part of the sample. Another option, more practical, is by using the bridge of one of the patterned devices. In both cases we used a wet etching which removes the YBCO but do not affect the substrate in order to obtain the right value of the thickness.

The profilometer located in our cleanroom has a diamond tip that is in contact with the sample during the whole scan, applying a force of 0.5 mg. Although this force should not affect the bridges of our devices we did the profilometer scans after using them for all the required experiments in order to prevent any damage. Usually we repeated the scan in different points along the same bridge to get more statistics. The scan is designed so that the tip starts in an etched part and goes in perpendicular direction to the bridge, steps over it and falls to the etched part on the other side of the bridge (figure 2.8).

2.2.3 Magnetic characterization of YBCO films

The basic characterization of the magnetic properties of our thin films was performed at the *Low temperatures laboratory* at ICMAB using a SQUID (Superconducting QUantum Interference Device). This measurement technique takes advantage of the Josephson effect [91] to detect very small magnetic fields. In particular a DC-SQUID [92] was used, with a set of pickup coils in the middle of a solenoid superconducting magnet. It has a vacuum system and it can reach up to 7T and go from 1.8K to 400K thanks to a helium cryostat. It permits measuring magnetic moments with a very high accuracy ($10^{-9} Am^2 = 10^{-6} emu$).

The sample is placed inside the coils and is magnetized using an uniform DC magnetic field. Afterwards it is mechanically moved along the coils (x-pos.) parallel to the external magnetic field (B_{ext}) inducing a current proportional to the variation of magnetic flux that is amplified and converted into a voltage signal (V_{SQUID}), proportional to the magnetization of the sample (figure 2.9). From magnetization measurements we can extract different information of our samples, depending on the conditions applied.

Critical temperature and critical current density

In order to characterize the performance of YBCO thin films we measure the critical temperature T_c and the critical current density as a function of the temperature ($J_c(T)$), since they are good indicators of the quality and

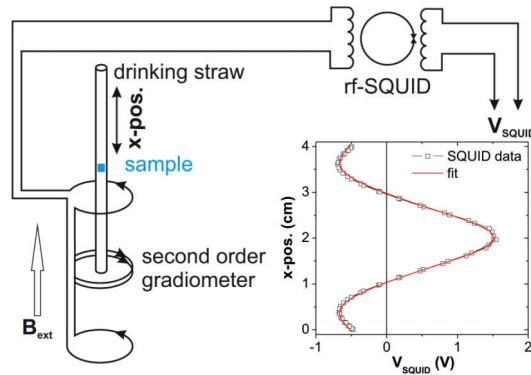


FIGURE 2.9: Schematic setup of a SQUID magnetometer with second order gradiometer. The inset shows the SQUID response V_{SQUID} versus sample position (x -pos.) [93].

the doping level.

In the phase diagram shown in figure 1.11 the relation between doping and T_c can be seen. To determine T_c we do a zero field cooled (ZFC) measurement, i.e. we cool the sample from RT to 10K with no magnetic field applied. At this temperature a small magnetic field of 2 Oe is applied and will be kept constant for the rest of the measurement. Then we measure the magnetization as a function of the temperature from 10K to 95K. At low temperature the superconductor expels the magnetic field from its interior, and hence the measured magnetization is negative, confirming the expected diamagnetic behaviour. Close to T_c the signal goes to zero and above T_c vanishes since the material is not in its superconducting state anymore. The value T_c can also be obtained from transport measurements, doing a resistivity versus temperature measurement by using a van der Pauw configuration [94] or in a 4-point configuration. T_c of all patterned devices has been checked by using the latter one. We also systematically used SQUID ZFC magnetization measurements to control the critical temperature of plane films since this technique does not require any lithography or bonding. There are different criteria that can be used to extract the value of the T_c . For the magnetization measurements we chose the temperature at which the magnetic moment is smaller than 10^{-4} emu (or 10^{-7} Am²) and the mid-point criterion [95] for the resistivity measurements. In figure 2.10 we plotted the normalized magnetization measured in several YBCO samples, all of them with good T_c values of 90K.

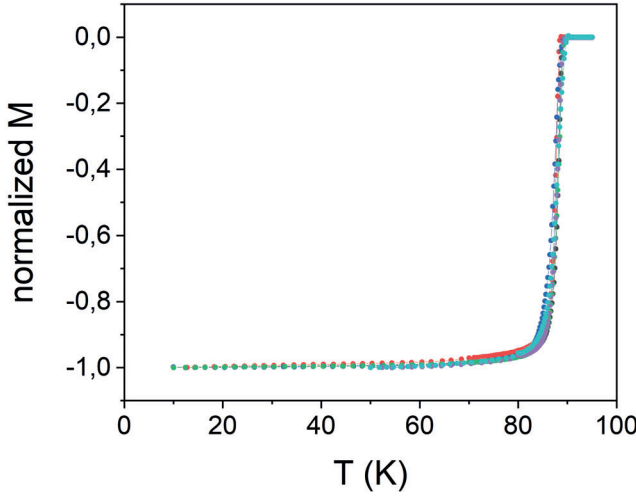


FIGURE 2.10: Magnetization measurements used to determine T_c for different YBCO thin films.

In order to obtain the critical current density J_c of the films we perform a Field cool (FC) measurement where the sample is cooled with an applied field of 3×10^4 Oe perpendicular to the surface of the sample down to 5K. Then the magnetic field is removed, leaving the sample in a remanent state and the value of the magnetization is recorded while warming it up to 95 K. The value of the magnetization is directly related to J_c according to Bean's critical state model [96]. We calculate it using the equation 2.1 for a square thin film, knowing its thickness and dimensions (being a the the length of one side of the sample and t the thickness). In figure 2.11 we plotted the J_c versus temperature obtained for several YBCO samples.

$$J_c(T) = \frac{3\Delta M(T)}{a} = \frac{6m(T)}{a^3 t} \quad (2.1)$$

For all investigated samples the J_c values obtained at 77K self-field are between 1 and 4 MA/cm², corresponding to high quality optimally doped YBCO thin films.

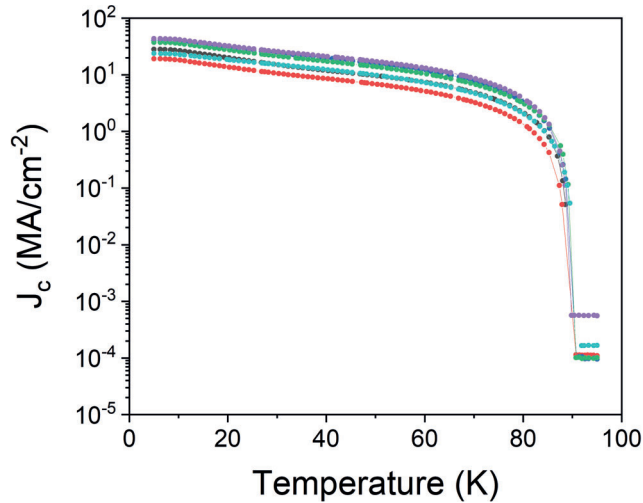


FIGURE 2.11: J_c vs temperature curves obtained for different YBCO thin films.

2.3 Device fabrication

After thin film growth and basic characterization we followed a multi-step process to fabricate several YBCO structures with different geometry and contact distribution. We fabricated top-top and top-bottom devices by using the lithography tools available in the Clean Room facilities at ICMAB.

2.3.1 Photo-Lithography

The lithography is a process used to print or transfer a pattern to a certain film, in our case YBCO films. To do that we may perform several steps all of them keeping the sample in a room with adapted yellow light.

Pattern design

First of all, we use a special software (CleWin5) to design the pattern or layout that we want to transfer, adapting it to the area of our samples and the dimensions of the devices that we want to study, with micrometric precision. An example is shown in figure 2.12, with twenty devices.

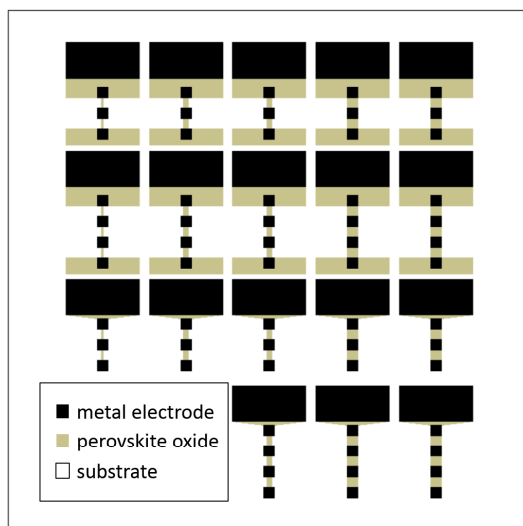


FIGURE 2.12: Example of lithography pattern or layout.

Photoresist deposition

The second step is depositing the photoresist on our sample. This is a polymeric material sensitive to the UV light of our lithography system. A positive photoresist was used, meaning that the areas exposed to the light become dissolvable for a developer that we use later, so that the only parts that will be protected by the photoresist are the ones not exposed the UV light.

First samples were cleaned with the organic solvents acetone, ethanol and isopropanol, using a nitrogen spray gun to dry it. The photoresist was deposited by spin-coating, using a dropper. The parameters were optimized according to the instructions of the manufacturer to obtain a flat layer of photoresist. The speed used was 5000 rpm and the total spinning time 25 seconds, getting a uniform layer with a thickness of 1mm. After the deposition the sample was placed in a hot plate for a soft-bake of 1 minute at 90°C to remove the solvents.

Light exposure or writing

In this step the sample was placed in the sample holder of the lithography system (Micro-Writer ML3 from Durham Magneto Optics Ltd.) which enables a direct-writing of the mask to the photoresist by using a laser-assisted technology. First an alignment and a focus of the writing lasers at the center of the sample was performed. Then the pattern to be transferred was uploaded and the rest of parameters were set according to the characteristics of the pattern. We had to calibrate the sample exposure depending on the feature size or the geometries. A precision in the range of one micrometer was obtained after proper optimization.

Photoresist development

After the writing step the sample was introduced in a developer made of tetramethyl ammonium $C_4H_{12}N^+$ diluted in water (2%) for 1 minute. This process was stopped introducing the sample in distilled water and afterwards it was dried with the nitrogen spray gun. We checked if the process was complete using an optical microscope with a UV filter light to prevent any exposition of the photoresist.

After these first steps the sample parts still covered with the unexposed photoresist are protected for a later metal deposition and a chemical or physical etching (see figure 2.13). AT this step we can follow two different processes, metal deposition and lift off or sample etching, depending the final objective.

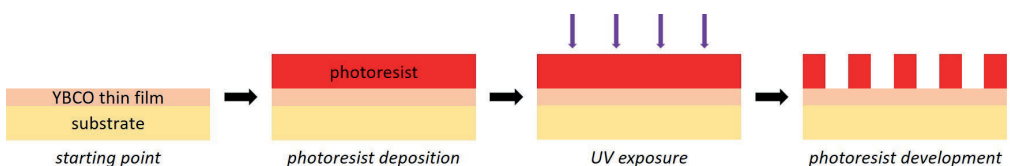


FIGURE 2.13: Sketch of the first steps of a device fabrication.

Chemical and physical etching

There are two possible options to get ride of the unwanted material after the photoresist development, leaving the YBCO patterned tracks below the

non-exposed photoresist (see figure 2.14): chemical etching and physical etching.

In chemical etching, the YBCO sample was introduced in diluted orthophosphoric acid (H_3PO_4) during a certain time, depending on the concentration of the solution used and the thickness that we want to etch. A calibration of the etching rate may be used for each concentration. Since this is a very isotropic process, it is not useful for very small patterns (few microns) is very appropriated when we want to define features larger than 10 microns since it is simple, fast, and cheap. This procedure was used when the minimum size of our patterns was equal or larger than $10\mu\text{m}$. The etching was stopped by introducing the sample in distilled water for few seconds. The material protected under the photoresist and the resist were not affected by the acid solution.

In physical etching the sample was introduced in an ion-milling chamber, where certain vacuum conditions were set in the presence of an inert gas, Argon (Ar) in our case. Ar^+ ions are emitted from an ion gun and are accelerated towards the sample thus removing the YBCO material from the surface. The pressure, the flow of ions and the accelerating voltage, parameters have been optimized giving a certain etching rate for the different species (e.g. $\sim 12\text{nm}/\text{min}$ for the YBCO). The photoresist can be affected by the Ar ions, but its etching rate is much slower than the one of YBCO thus protecting the layer. Since this technique is very anisotropic higher resolution patterns could be fabricated. The physical etching was used for patterns with very small minimum sizes, less than $10\mu\text{m}$. The collisions of the Ar ions during the milling can heat the sample, raising its temperature up to values that could deoxygenate or damage the material. Short runs with breaks of some minutes were done in order to dissipate the heat. To stick the sample to the holder a drop of silver paint was used, also helping to dissipate the heat.

In both cases in order to check that the whole thickness of our YBCO thin film was removed, the resistance of the etched parts was measured and compared with the one of the bare substrate. After the edge process, we removed the photoresist which was protecting the sample by introducing it in an ultrasonic bath with acetone.

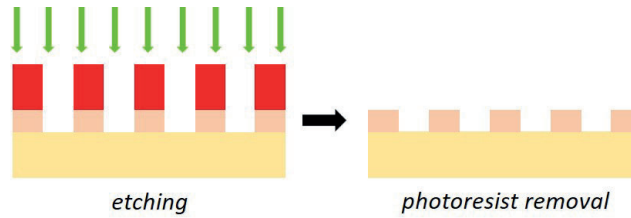


FIGURE 2.14: Sketch of the etching process.

Metallic electrodes

Metallic electrodes to be used for electric measurements were fabricated by sputtering and lift-off. The first step is the transfer of the pattern to the photoresist and its development to expose the parts of the sample where we want to put the electrodes. After the resist development we deposit the metal by using a DC sputtering integrated in the same chamber that we use for Ar milling. The sample was attached to the holder and the chamber was pumped down to the required vacuum (10^{-6} mbar) and plasma conditions. In this case a metal target (silver *Ag* or gold *Au*) is bombarded by accelerated ions of an inert gas (argon). The metal atoms are ejected to the sample, that is in front of the target at a certain fixed distance. A previous calibration was performed to set the deposition rate and achieve a good attachment electrode-sample with low contact resistances ($\sim 10^{-2} \Omega \cdot \text{cm}^2$). The deposited metal is in contact with the surface of the YBCO only in the parts where the photoresist was exposed to UV light and developed. After the sputtering process the sample was introduced in an ultrasonic bath with acetone for a lift-off process where the photoresist and the metal on top of it will be removed, remaining only the desired electrodes (figure 2.15). The typical dimensions of the electrodes were 50 to 100 nm thickness and $100 \times 100 \mu\text{m}^2$ area. It is important to note that the effective area of the contact will depend on the dimensions of the device. When depositing a $100 \times 100 \mu\text{m}^2$ contact on top of a $10 \mu\text{m}$ wide device, the effective area will be $10 \times 100 \mu\text{m}^2$.

In some experiments contacts with low contact resistance were needed. For that, we sputtered contacts with a thickness between 200 or 300 nm and dimensions of several hundreds of μm . Moreover, a thermal treatment was performed after the electrode deposition to reduce the contact resistance. In this case the sample was introduced in a quartz tube with a constant

flow of oxygen of 0,15L/min at 450°C for one hour. The contact resistance after the annealing was reduced to $\sim 10^{-8}\Omega \cdot cm^2$.

Similar switching performances were obtained using silver and gold electrodes, thus excluding any possible effect of silver diffusion within the sample in the switching behavior.

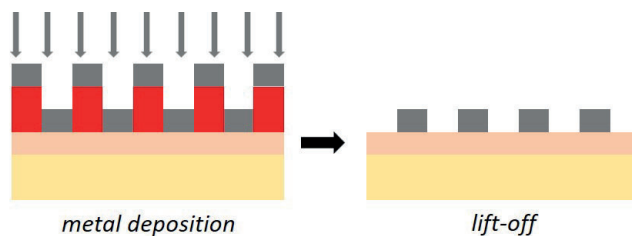


FIGURE 2.15: Sketch of the metal deposition process.

2.3.2 YBCO film lamination for top-bottom devices

In the case of the top-bottom YBCO devices the fabrication was not that simple since if we want an epitaxial thin film we should use a substrate with good epitaxy and thus it cannot be directly grown on top of a metallic substrate which could be used as bottom electrode. In order to obtain top bottom devices we exfoliated a commercial coated conductor from THEVA manufacturer. Figure 2.16 shows a sketch of a coated conductor cross section which consists on a substrate tape of a metallic alloy (hastelloy) of thickness $40\ \mu m$, several buffer layers of different oxides that bring the required epitaxy to the substrate, the YBCO film, and an Ag protective layer of $2\ \mu m$. The first buffer layer is a MgO layer textured by inclined substrate deposition covered with a top buffer of 20 nm thick $LaMnO_3$ (LMO) optimized for YBCO grown. A $3\ \mu m$ YBCO film was grown on top of the buffers with PLD. Finally, the whole stack is covered with a coating of copper of thickness between 20 and $40\ \mu m$ which assures a good electrical and mechanical stabilization of the coated conductor. In particular, it prevents the coated conductor from physical damage and avoids undesired quenches since it is a very good heat conductor. We used a mechanical process of delamination, optimized by other members of the group, to remove the copper in the sides and separate the stack of Cu/Ag/YBCO in the union of the top buffer layer and the YBCO layer. Turning it upside down we get a flexible YBCO epitaxial

layer of $3\ \mu\text{m}$ on top of a silver and copper layer that will be used as bottom electrode.

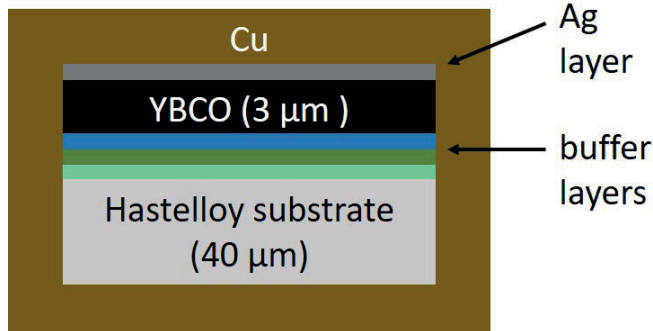


FIGURE 2.16: Cross section of the commercial coated conductor that was subsequently delaminated to obtain the YBCO epitaxial layer on top of a Ag over Cu bottom electrode.

In order to pattern devices and deposit contacts we need it to lay on a rigid and flat surface. So, we glued the YBCO/Ag/Cu stack it on top of a silicon substrate using a special resin (see figure 2.17) and we patterned the top electrodes on top of the YBCO.

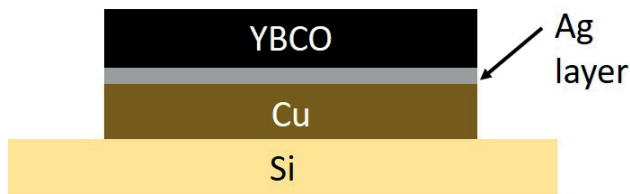


FIGURE 2.17: Sketch of a YBCO sample after the delamination process, glued on top a Si substrate.

2.4 Electrical Transport Measurements

Field-induced MIT and resistive switching effects in the fabricated devices have been studied by means of voltage or current pulses.

Physical Properties Measurement System (PPMS)

Along the thesis several electric transport measurements were performed with different objectives using a 2-point or a 4-point configuration. Most of them were carried out in Physical Properties Measurement System (PPMS) from Quantum Design, located in the Low Temperatures and Magnetometry Service Laboratory at ICMAB. This equipment has a vacuum chamber with a helium cryostat that allows us to work with good precision in the range 1.8 K to 400 K, controlling the temperature of the sample with a thermometer placed right below the sample holder. It is equipped with a superconducting magnet that can reach up to 9T with a resolution of 0.1mT.

The 4-point configuration consists on two external electrodes to inject the current and intermediate contacts to measure the voltage. This configuration was used in transport measurements where we wanted to avoid the contribution of the contact resistance and hence measure the bulk resistance of a certain volume of the material. We also used these configuration to measure the temperature dependence of the resistance (obtaining the typical RT curves and being possible to determine its T_c). The voltage was measured with the nanovoltmeter of the PPMS, applying an AC or DC current in the range of $10\mu\text{A}$ to 2A , with a resolution of $0.1\mu\text{A}$. In most of the cases we applied an AC current of 0.01 mA and frequency 33 Hz . A higher current was applied when signal was too low, always whit a compliance current of 0.1 A .

RT curves were measured in the same way. Regarding the temperature sweep, the normal-state region (usually from 95K to 300 K) was scanned at the highest speed, using a ramp of 20 K/min and measuring the resistance every 2 K . In the region close to T_c the ramp was reduced to 0.5 K/min to ensure temperature stabilization and the resistance was measured every 0.1 K . This way we can determine the value of the T_c with more precision. The range of scanned temperatures would depend on how deoxygenated was the sample measured. As we mentioned before the mid-point criterion [95] was used to determine the T_c .

The software used for the PPMS measurements was the one provided by the manufacturer and meets all our requirements, being possible to create different sequences that allowed us to automatize the procedure.

Keithley 2450 Source Measure Unit (SMU)

The resistive switching loops were measured by means of an external sourcemeter (Keithley 2450), with the sample placed inside the PPMS. In this way we could perform magnetic field or temperature dependent measurements by using the PPMS cryostat.

Current-voltage (I-V) and resistance-voltage (R-V) curves studied in chapters 3 and 5 were obtained with different 2-point configurations (top-top or top-bottom), applying voltage sweeps of 100 points going from 0 V to the desired voltage and from that voltage back to 0 V with also 100 points, with a compliance current of 0.1 A. Regarding the time length of the sweeps it depends on a parameter of the SMU called NPLC (number of power line cycles) which determines the power line induced AC noise integration time for each applied voltage. By reducing the NPLC the speed of the measurement is also increased but losing accuracy. We tested different values and found still high accuracy with voltage sweeps of 100 points of time length of 2 seconds. This time could slightly increase if a high voltage is applied (higher than 10 V).

2-point resistance measurements were also performed occasionally with this SMU applying a DC current of 0.01 mA, using the PPMS for temperature scan and obtaining the corresponding RT curves.

Keithley 2601B Pulser/SMU

An important part of the 2-point measurements in both top-top and top-bottom configuration in chapter 5 (sections 5.3 and 5.4) were done using another external SMU, the Keithley 2601B Pulser/SMU. It allows us to apply short voltage (or current) pulses of duration in the order of 100 μs or higher and customize the profile of the pulses and trains of pulses, detailing the number of pulses, input voltage (or current), bias voltage, t_{on} and t_{off} . In our experiments we used only voltage pulses with duration of ms or higher. More features of this SMU could be exploited in future works.

LabVIEW programs

In order to do the measurements with both SMUs we designed different programs using *Laboratory Virtual Instrument Engineering Workbench* (LabVIEW), a system-design platform and development environment for a visual programming language from National Instruments. This gave us the possibility of customizing the measurements for our purposes and automating them.

Electromigration experiments

The electromigration runs from the experiments depicted in 4 were mainly performed in collaboration with the team of Prof. A. Silhanek from Université de Liège, using their own setup and home made software. The voltage bias is ramped up while monitoring the change in conductance dG/dt and keeping it in a preset range with a feedback loop, measuring with a nanovoltmeter and an amperemeter. A detailed explanation of the process followed can be found in [97, 98].

Wire-bonding

We used the wire-bonding technique to connect the electrodes to the desired sample holder. Figure 2.18 show a typical puck used with different contacts which can be connected to the experimental setup (PPMS or external voltage or current sources) using normal wires or BNCs. In order to easily reconfigure the pins of the puck to perform measurements in different regions and with different configurations we fabricated a "switch box" interconnected between the puck and the electronics of the PPMS or the external SMUs.

The connection between the pads in the puck and the micro-metric electrodes patterned on top of the devices were done with an ultrasonic wire-bonder. This technique consists on a needle with an aluminum (Al) wire of tenths of microns of diameter which is pressed against the electrode and attached using ultrasound vibrations and pressure. The bonded wire on the sample was extended to the desired pad of the puck and connected there using the same procedure.

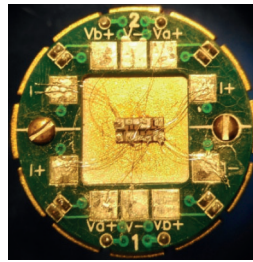


FIGURE 2.18: YBCO sample wired to a PPMS puck.

2.5 Oxygen doping characterization

2.5.1 Hall measurements

Hall effect measurements were performed in order to measure carrier concentration and hence determine the oxygen content (or doping) of a track, or the changes induced in our experiments. Previous measurements can be found in the literature for YBCO and other cuprates [99–101] also to measure mobility and scattering characteristics.

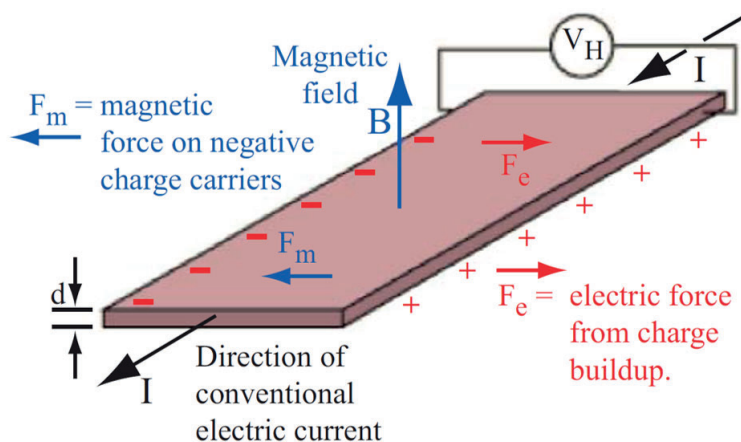


FIGURE 2.19: Sketch of the Hall effect, extracted from [102].

The Hall effect [103] is the appearance of a measurable transverse voltage in a conductor when a magnetic field is applied perpendicular to the direction of the electric current. The charge carriers with velocity \vec{v} flowing in the direction of the current I are deflected to one side of the conductor due the Lorentz Force \vec{F}_L , perpendicular to \vec{v} and the magnetic field \vec{B} following

the right hand rule for cross products. The accumulation of charge carriers in one side generates an electric field \vec{E} and hence a transverse voltage known as Hall voltage V_H (see figure 2.19).

The Lorentz force, given by formula 2.2, will finally be zero when an equilibrium is reached ($\vec{F}_L = 0$).

$$\vec{F}_L = \vec{F}_e + \vec{F}_m = q(\vec{E} + \vec{v} \times \vec{B}) = 0 \quad (2.2)$$

In the case a p-type conductor where the carrier are holes the q in the formula is equal to elementary charge of the electron e with positive sign. Solving the equation an expression to calculate the density of carriers n (number of carriers per volume unit) and its sign is obtained, so one can distinguish if the free carriers are electrons or holes.

$$n = \frac{I}{ed \frac{dV_H}{dB}} \quad (2.3)$$

This expression depends on the applied current (I), the charge of the electron (e), the thickness of the sample (d) and the slope of the linear variation of the Hall voltage with the magnetic field.

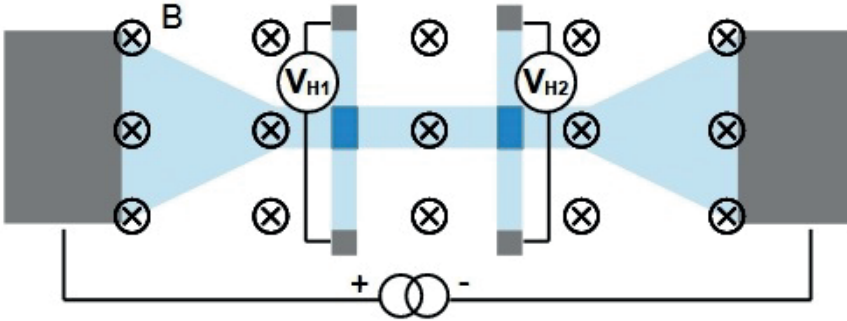


FIGURE 2.20: Example of a Hall measurement. The electric current from the left to the right of the device with an applied magnetic field B . The Hall Voltages V_{H1} and V_{H2} are measured in the crossing with the two transverse structures (dark blues parts).

Hall measurements were performed in a PPMS at constant temperature (at RT or at 105 K depending on the experiment) applying a magnetic field ramp from -9 T to +9 T along the c-axis, this is, perpendicular to the sample

surface (see figure 2.20). The resistance measurements were done using a 4-point configuration and the parameters depicted in section 2.4.

2.5.2 Raman spectroscopy

Micro-Raman spectroscopy is a useful technique for the local characterization of oxygen doping in YBCO thin films. The spatial resolution of this technique is of the order of $1\ \mu\text{m}$, much higher than the one obtained through Hall measurements which in our case was of the order of tenths of microns.

Raman effect [104] is the inelastic scattering of light (photons) by a material, creating an elementary excitation in the material, a Stokes process. If the material was previously excited this inelastic scattering can annihilate an elementary excitation. This would be an anti-Stokes process. The nature of the excitation can be a phonon (vibrational) or a plasmon (plasma oscillation), etc. In this work we focus on the Raman scattering by phonons in YBCO. An incident photon excites the material into an intermediate state creating an electron-hole pair, which is scattered into another state emitting a phonon, and then it recombines with the emission of a scattered photon [105]. The phenomenon is illustrated in figure 2.21

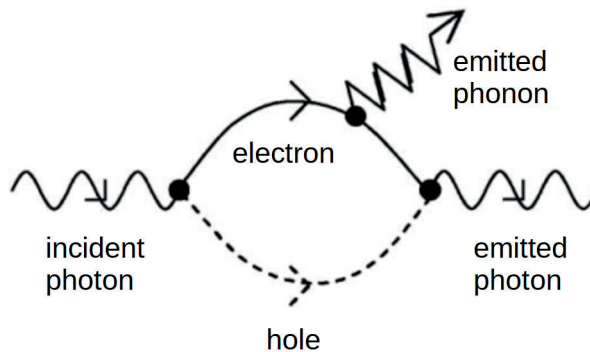


FIGURE 2.21: Feynman diagram of a Stokes Raman scattering. In the case of an anti-Stokes process the diagram is the same but the phonon is absorbed instead of emitted. Adapted from [105].

In order to distinguish the photons from the elastic scattering (Rayleigh scattering) delicate optical systems are needed. The shift between the frequency, and hence the energy, of the incident laser light and the one

we detected is correlated to the phonon excitation in our material. In this sense, usually infra- red and visible light are used.

The peaks obtained in the measured Raman spectra are related to the different vibration modes. In orthorhombic YBCO five z-polarized phonons can be found (see figure 2.22). The vibration of the barium (Ba) atom at frequency 115 cm^{-1} , the copper Cu(2) atoms at 150 cm^{-1} the O(2) and O(3) oxygen atom at 340 and 440 cm^{-1} , and the O(4) apical oxygen at 500 cm^{-1} . The two frequencies of O(2) and O(3) involve both oxygen atoms, the symmetric vibration of atoms O(2,3) at 340 cm^{-1} and the antisymmetric vibration of atoms +O(2,3) at 440 cm^{-1} .

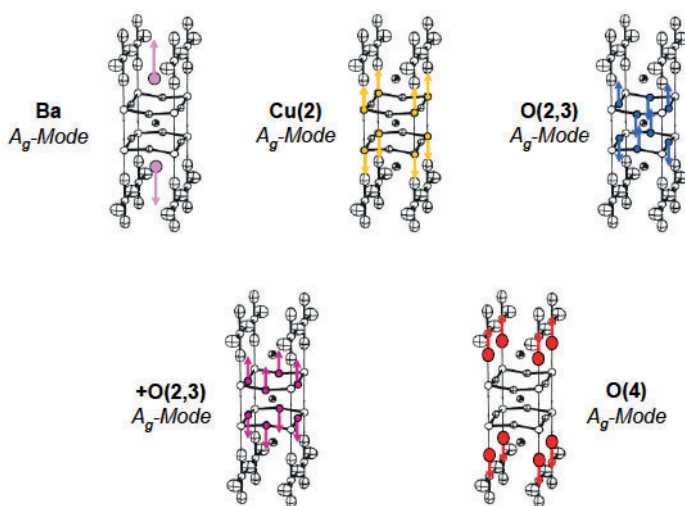


FIGURE 2.22: Schematic representation of z-vibration of optical active Raman modes of YBCO (extracted from [106]).

The +O(2,3) mode at 440 cm^{-1} in optimally doped YBCO spectra is not easy to observe because is weak at room temperature [107], but its intensity increases in the low oxygenated regions. The O(4) mode at 500 cm^{-1} accounts for the c-axis motion of the apical oxygen atoms bridging the CuO chains and the CuO₂ planes [108, 109]. It can be found in both tetragonal and orthorhombic YBCO [110] and it strongly depends on oxygen doping. The spectral range used to the characterization of YBCO films was among $100 - 600\text{ cm}^{-1}$ (see figure 2.23), where the five modes can be seen.

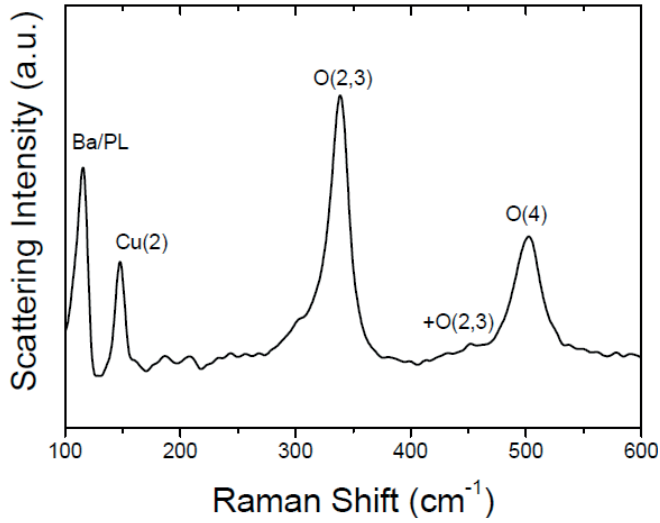


FIGURE 2.23: Raman spectrum of an epitaxial optimally doped YBCO thin film with the O(4) mode at 500 cm^{-1} . The Barium A_g -mode is overlapped with the plasma line at 117 cm^{-1} . Extracted from [111].

From the spectra obtained the value of the frequency of the O(4) mode was extracted by fitting the curve in the range from 375 to 575 cm^{-1} (figure 2.24). There are two peaks, the $+O(2,3) - A_g$ and $O(4) - A_g$ modes, and both correspond to Lorentzian profiles. We used the equation 2.4 to fit them.

$$I_{A_g} = \frac{2A}{\pi} \frac{\gamma}{4(\omega - \omega_0)^2 + \gamma^2} + \text{const} \quad (2.4)$$

being A the area of the curve, ω_0 the phonon frequency, γ the Full Width at Half Maximum (FWHM) of the profile and “const” a constant background term.

We can compare the values of the frequency of the O(4) mode to the values in the literature. Nevertheless, it is very interesting and more visual to relate this values to the oxygen content ($7-\delta$). A shift in the phonon mode frequency ω_{O4} is originated in the variation of the c-cell parameter with the oxygen content. When the latter decreases there is a bond softening and the unit cell expands, so the c-cell parameter increases and therefore the phonon frequency decreases too.[109, 112].

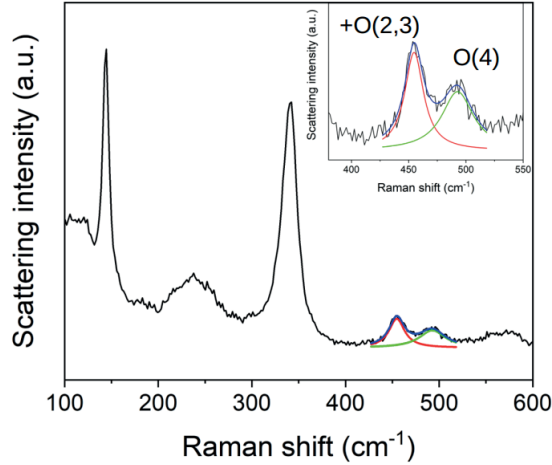


FIGURE 2.24: Fit of a Raman spectrum measured in a point of a deoxygenated channel. The peak of the O(4) mode is around 491 cm^{-1} . Inset shows a zoom of the fitted part of the spectrum.

A simple empirical law was used to calculate the oxygen content¹ as a function of the O(4) phonon frequency measured in the experiments. The equation 2.5 was calculated in [108] using experimental data points from Raman spectroscopy measurements from different authors using oxygen-deficient YBCO samples and an argon laser with wavelengths 488 and 514 nm (very similar to the ones we used).

$$\delta = 13.58 - 0.027\omega_O \quad (2.5)$$

Many works using Raman spectroscopy in YBCO can be found in the literature, with different objectives such as studying the strain in thin films [113], quality control for device production [114], determination of the degree of epitaxy of thin films [115] or quantification of oxygen content [113, 116–119]. A deep study in YBCO thin films was carried out in this group to study the composition with different growth techniques, as well as the presence of impurities, defects or secondary phases (see [111]).

Two different micro-Raman set-up equipments were used. One systems is located at the Universitat Autònoma de Barcelona (UAB). In this case measurements were performed with the guidance of Dr. Narcís Mestres.

¹Note that the value of δ determine the oxygen content according to $YBa_2Cu_3O_{7-\delta}$

The equipment was a Jobin-Yvon T64000 Raman spectrometer with a detector charge-coupled device (CCD) detector, cooled with liquid nitrogen. The system was attached to an argon-laser line of 514.5 nm and a metallographic microscope Olympus with three plano-achromatic objectives (we used the x100) focusing to a $1\mu\text{m}^2$ spot. The measurements were done at room temperature and using a backscattering geometry. In order to avoid damaging the sample through laser-induced local heating the power on it was kept below 1mW. With this setup a resolution of $\sim 2\text{ cm}^{-1}$ was attained. The other system used was located at the cleanroom facilities of IMB-CNM under the supervision of Dr. Gemma Rius. This system consists of an Xplora Horiba Jobin-Yvon micro-Raman spectrometer using the backscattering geometry at room temperature. A high sensitivity digital air cooled CCD (charge-coupled device) was used as detector. For the excitation a 532 nm laser line with a x100 magnification lens was used, focusing to a $1\mu\text{m}^2$ spot and keeping again the power lower than 1 mW to avoid possible damage in the sample due to local heating induced by the laser. The polarization of the electric field of the incident and scattered light was kept parallel to the crystallographic a-axis of the YBCO layer. The resulting resolution for this configuration was $\sim 2\text{ cm}^{-1}$.

With the used laser wavelengths, the penetration depth of light inside of YBCO film is about $\sim 80\text{ nm}$.

2.6 Numerical simulations

Numerical simulations of the field-induced oxygen diffusion in the YBCO structures were performed using the partial differential equation solver developed by COMSOL multiphysics. The model used introduces two interactions: the first one accounts for the conventional diffusion of oxygen ions in a vacancy field in a thermally activated framework, reflected in the diffusion coefficient which depends on the temperature. The other one accounts for the electrical nature of the oxygen anions, that can move inside the material, permitting the electrically driven diffusion induced by the electric field generated when applying an external bias voltage.

Charge neutrality in the system is assured since the metallic behavior of the system permits a local charge balance by mixed valence states.

We used a rectangular domain of width x parallel to the a-b planes with $x \in [0, 520] \mu m$ and thickness y parallel to the c-axis with $y \in [0, 10] \mu m$. The two top contacts are located $35 \mu m$ away from both limits of the domain, and both with a length of $40 \mu m$, and they are not part of the simulation domain. The bias voltage is applied to the left contact while the one on the right is grounded.

The following assumptions were made in the model:

1 A diffusion equation in a continuous medium approximation is assumed. The diffusion coefficient is anisotropic, with a ratio $D_x/D_y = 10^6$ (see table 2.1) [120], that describes an anisotropic oxygen diffusion along the CuO_2 planes and across them, no matter the diffusion mechanism, as is observed experimentally.

2 The concentration of oxygen ions that can be diffused is determined considering the maximum and minimum oxygen stoichiometry in YBCO, 7 and 6, with $\delta \in [0, 1]$, taking into account the volume of the structures orthorhombic and tetragonal (4.03×10^{28} and $3.41 \times 10^{28} ions/m^3$, respectively). The concentration in the pristine state is considered homogeneous ($c_0 = 3.6 \times 10^{27} ions/m^3$). Considering that only the oxygen in excess to the tetragonal composition can contribute to the oxygen diffusion, the variation in the oxygen concentration can vary between $c = 0$ and $c = 6.26 \times 10^{27} ions/m^3$.

3 Oxygen vacancies are redistributed within the system, with no exchange of oxygen with the exterior.

4 The material is considered an electronic conductor in which the electric resistivity is directly correlated to the local oxygen concentration. The local conductivity is a linear function dependent on the oxygen, describing the conductivity change between the underdoped and the optimally doped states [100, 121]. See table 2.1.

5 The electric field is defined through the Ohm constitutive equation as a function of the current density J and the electronic conductivity σ , neglecting the contribution of the ionic conduction (see equation 2.7). The electronic carrier concentration distributes maintaining the local charge

compensation.

6 The diffusion coefficient D and the electronic conductivity σ are anisotropic, higher along the a-b planes (x-axis). See table 2.1.

7 The contact surface conductivity was considered parabolically distributed in order to soften the contact discontinuity in the pad edges.

Equation 2.6 shows the evolution in time of the oxygen concentration in each point of the domain:

$$\dot{c} = \nabla(\mathbf{D} \cdot \nabla c + z \cdot \mathbf{u} \cdot F \cdot c \cdot \nabla V) \quad (2.6)$$

being \dot{c} the time derivative of the concentration, \mathbf{D} the diffusion tensor, z the charge number of oxygen ions, \mathbf{u} the Nernst-Einstein ratio ($\mathbf{u} = \mathbf{D}/RT$), and F the Faraday number. The electric potential can be deduced from the constitutive and the charge conservation equations as

$$\mathbf{E} = -\nabla V = \frac{\mathbf{J}}{\sigma} \quad \text{and} \quad \nabla \cdot \mathbf{J} = \rho \quad (2.7)$$

being \mathbf{J} the electric current density, σ the electronic conductivity and ρ the electronic charge density.

The following table includes the parameters used in the simulation:

effective variation of oxygen concentration	$c = 0 - 6.26 \times 10^{27} \text{ ions/m}^3$
initial oxygen concentration	$c_0 = 3.6 \times 10^{27} \text{ ions/m}^3$
electronic conductivity	$\sigma_x = 10^2 \text{ S/m}; c < 3.01 \times 10^{27} \text{ ions/m}^3$ $\sigma_x = 1.54 \times 10^{-22} (c - 3.01 \times 10^{27}) + 10^2 \text{ S/m};$ $(3.01 < c < 6.26) \times 10^{27} \text{ ions/m}^3$
diffusion Tensor	$\sigma_x = 10\sigma_y$ $D_x = 10^{-7} \text{ m}^2/\text{s}$ $D_y = 10^{-13} \text{ m}^2/\text{s}$
contact surface conductivity	$10^7 / [(x - x_0)^2 + 10] \text{ S/m}; x_0 = \text{contact center}$

TABLE 2.1: Parameters used in the simulations.

Chapter 3

Field-induced oxygen migration in YBCO films

In this chapter we investigate the possibility of modulating a reversible and non-volatile resistive switching effect in YBCO superconducting thin films. The switching effect is generated through a metal-insulator transition (MIT) induced by means of electric field-induced oxygen diffusion that changes the carrier concentration and the associated electrical properties.

The mechanism behind the generation of an electrochemical MIT in metal oxides is still not clear although it is associated to a local migration of oxygen vacancies, usually produced in confined filaments or homogeneously distributed interface effects [15–17, 122, 123]. In metallic perovskite oxide thin films however, volume phase resistive switching effects have been observed, inducing homogeneous MIT through the sample thickness [14, 15].

In this work we explore this volume MIT modulation and analyze the properties of the material after the switching and the extension of the switching event. Designing devices with different geometries we study the possibility of inducing lateral or vertical oxygen diffusion, taking advantage of its anisotropy, and exploring its potential to create transistor-like devices. The superconducting properties of the material are also analyzed by producing the resistive switching effect at a temperature below the critical temperature (T_c). Volumetric superconductor to insulator transition (SIT) may be induced with the possibility of switching ON and OFF the superconducting state in transistor-like devices with a loss-less superconducting channel.

We designed devices with top-top configuration adapting the geometry, lateral dimensions and thickness of the bridges and the contact areas to achieve different functionalities. A 2-point configuration was used to induce the resistive switching and study the influence of different parameters on it. We also did electrical transport measurements using a 4-point configuration in order to determine the oxygen diffusion in the bulk, both vertical and lateral, generated by applied external voltage. They were also used to check the changes in T_c since it is directly related to the oxygen content. Micro-Raman spectroscopy measurements were also carried out to study the oxygen diffusion along the bridges and quantify the local oxygen content as a complement to the transport measurements. A theoretical model was developed to understand the oxygen dynamics in our YBCO thin films, beyond other theoretical studies in which the mechanism playing a role is the modulation of a Schottky depletion layer or the formation of a conductive filament [124–129]. We got satisfactory results in agreement with our transport measurements and micro-Raman experiments.

3.1 Device fabrication

The devices used in this chapter were patterned in YBCO films with thicknesses between 50 and 250 nm. Devices with tracks 1000 μm long and 1 to 100 μm wide were fabricated. Figure 3.1 shows a generic device that offers the possibility of using different configurations to induce vertical and lateral oxygen diffusion. The big grey contacts (A_1 , A_2 , A_3 and A_4) are 200 to 300 nm thick and annealed, while the rest (A_5 , A_6 , B_1 , C_1 and C_2) are thin (50 to 100 nm thick), not annealed and with smaller area. We used a 4-point configuration in order to measure the changes in bulk resistance or the changes in the temperature dependence of the resistance and the T_c . A small current is applied between contacts A_1 and A_2 and the voltage is read using A_3 and A_4 or A_5 and A_6 . The pink-colored contacts were used as gate electrodes to induce the resistive switching always in top-top 2-point configuration. By using two small not-annealed contacts switching effects will be induced in the two gates. On the contrary, we can use one large annealed contact with a small gate if we want to induce the resistive switching just below the gate. In this case, the large area and the better contact resistance avoid any switching below the large annealed electrode.

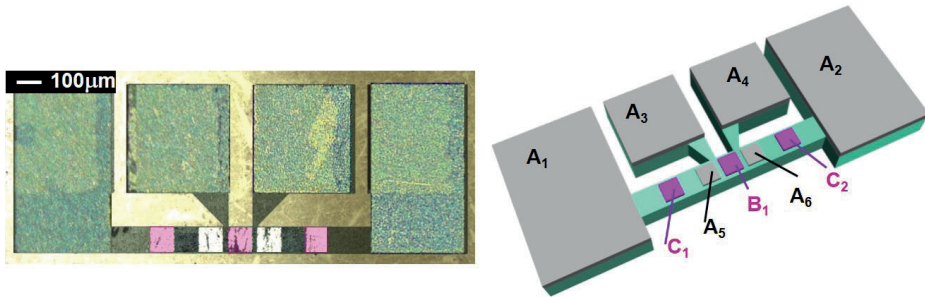


FIGURE 3.1: Optical image and sketch of a multielectrode device. Grey contacts are used to do 4-point measurements while pink-colored contacts are used as gate electrodes to induce the resistive switching.

In order to study the oxygen diffusion, we designed two different kind of devices (see figure 3.2). VERT-gate devices were designed to study the vertical oxygen diffusion (along the c -axis). In this case the switch is induced only in one gate (B_1) with the help of a non-switching contact A_i . An evaluation of the gate-tunable volume located below the gate (R_{vol}) is done using a 4-point configuration, applying a small current between drain and source (A_1 and A_2) and using two other contacts to measure the voltage, placed close to the switching gate (A_3 and A_4 or A_5 and A_6). LAT-gate devices were designed to study the lateral oxygen diffusion (along a - b planes). The resistive switching is induced applying a voltage between gates C_1 and C_2 and again a 4-point measurement is done to evaluate a gate-tunable volume (R_{vol}) located between the gates applying a small current between source and drain (again A_1 and A_2) and using two other contacts to measure the voltage, placed in the middle of the two switching gates (again A_3 and A_4 or A_5 and A_6). The voltage contacts are not indicated in the sketches of figure 3.2 for simplicity, but they are indicated in the general sketch shown in figure 3.1.

The characterization of the devices was performed in different ways depending on the objective of the experiment. In order to study the characteristics of the resistive switching in YBCO and the influence of different conditions and parameters on it, two point-measurements were carried out to obtain R - V , I - V and $R(T)$ curves. Voltage sweeps were applied usually going from 0 V to the desired voltage in 100 steps, which take around 10

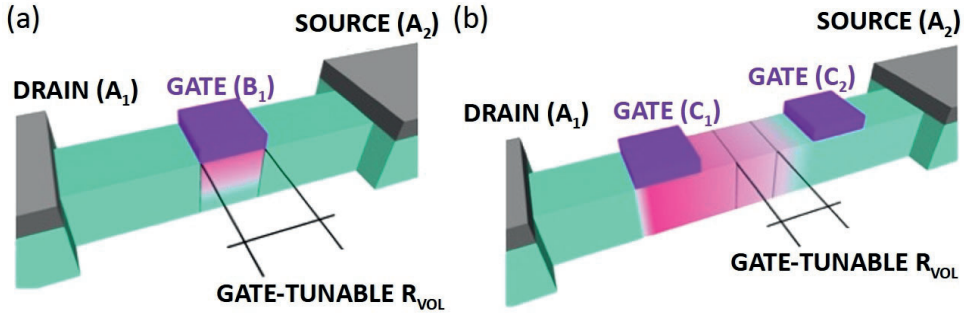


FIGURE 3.2: Sketch of both (a) a VERT-gate device and (b) a LAT-gate device. A small current is applied between source and drain. The contacts to measure the voltage in R_{vol} are not included in this sketch for simplicity.

seconds, with a compliance current of 0.1 A. All measurements were done in a top-top configuration. The temperature dependence of the resistance of switched contacts was measured using a 2-point configuration with the help of a non-switched electrode applying a small dc current of 10^{-5} A. The volume resistance changes were measured in a 4-point configuration by applying an ac current of 10^{-5} A. Measurements at different temperatures were performed by using the PPMS cooling system.

3.2 Resistive switching characteristics

Figure 3.3 shows the I-V curves in a semilogarithmic scale measured in a 250 nm thick and $30 \mu\text{m}$ wide VERT-gate device applying voltage sweeps of $\pm 5\text{V}$ at 100 and 400 K. The switching loops show a non-volatile bipolar behavior. Starting from the pristine low resistance state (LRS) a negative voltage is applied (1), switching to the high resistance state (HRS). This new state is non-volatile, as is preserved when sweeping the voltage back to zero (2). In a subsequent positive voltage sweep the system switches back to the LRS (3) and this state is also non-volatile since it is preserved when sweeping the voltage back to zero (4). If we apply a positive voltage in the pristine LRS system there is no change induced since in this state it is already optimally doped and it is hard to introduce more oxygen on it.

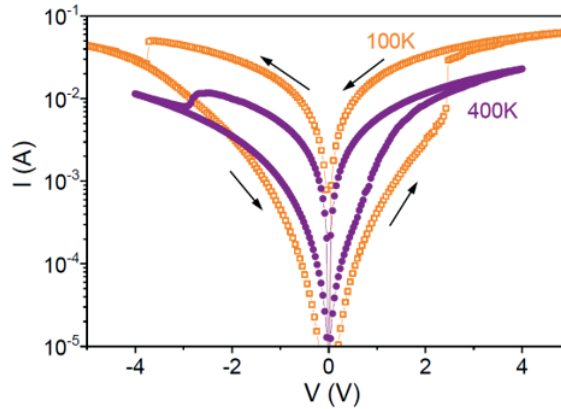


FIGURE 3.3: Semilogarithmic I-V hysteresis loops measured in a 250 nm thick and 30 μm wide VERT-gate device at 100 and 400K. Numbers and arrows indicate the voltage sweep evolution.

The associated R-V hysteresis loops measured at different temperatures show the same behavior (see figure 3.4). Large resistance changes can be induced using low voltages. Moreover we observe that the hysteresis clearly increases at low temperatures although the influence of the temperature in the voltage where the switching is induced is not clear. At higher temperatures the oxygen mobility is higher so less voltage would be expected to be needed for the switching. This trend is fulfilled for all temperatures except from the lowest one (100 K) at negative voltages. More statistics should be performed in order to investigate this effect. A common feature for all temperatures is that there is an asymmetric behavior regarding the voltage needed to switch to the LRS and the voltage needed to switch to the HRS. This was found for every tested device and will be discussed later in the theoretical model. The inset displays the non-normalized R-V curve measured at room temperature (300 K), showing that the resistance ratio at low voltages is around 2 orders of magnitude.

An evaluation of the conduction mechanism in the metal-oxide interface was done by plotting the derivative $d(\ln I)/d(\ln V)$ as a function of $V^{0.5}$ (see figure 3.5). In the LRS the derivative is almost constant and equal to 1, with a small deviation at 100K for high voltages. This is consistent with the ohmic behavior expected for a metal, as it is optimally doped YBCO. In the HRS the

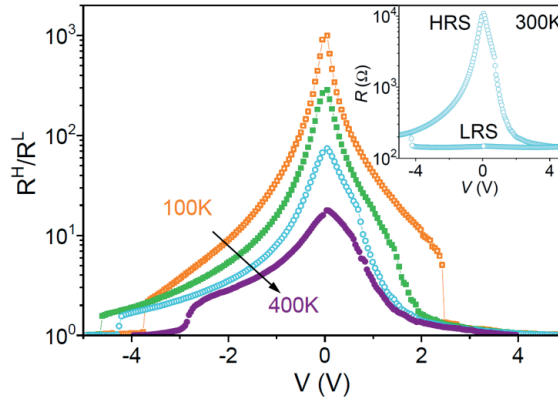


FIGURE 3.4: High resistance state and low resistance state ratio as a function of the bias voltage for different temperatures. Inset shows the hysteresis loop measured at 300 K.

behavior cannot be described by a single electrode or bulk limited mechanism [130, 131].

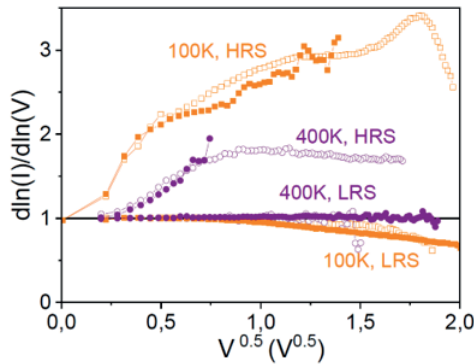


FIGURE 3.5: Derivative of $\ln I$ respect to $\ln V$ as a function of $V^{0.5}$ at 100 K (orange squares) and at 400 K (circles) measured when applying positive voltages (solid symbols) and negative voltages (open symbols).

The increase in the R_H/R_L ratio when lowering the temperature can be explained through the temperature dependence of R_H and R_L , which is plotted in figure 3.6. These curves were obtained by applying a current of $10^{-5} A$ in a two-point configuration with the help of a non-switched large electrode. In the case of LRS the resistance decreases with temperature,

characteristic of a metal, and presents a superconducting transition at 90 K. This is the expected behavior for an optimally doped superconducting YBCO film. The resistance measured below T_c corresponds to the contact resistance and is of the order of $10\ \Omega$. With resistive switching the system suffers a metal- insulator transition (MIT). In the HRS the resistance increased with the temperature, which is the expected behaviour for an insulator. The resistance at 300 K increased more than two orders of magnitude. Both things are compatible with an oxygen-deficient (or underdoped) YBCO, with $\delta > 0.65$ [100, 121]. In this device the resistance ratio is close to two orders of magnitude at 400 K, a little higher than in the device of figure 3.4. The different temperature dependence of the resistance in both the HRS and the LRS accounts for the differences in the hysteresis loops in figures 3.3 and 3.4 respectively.

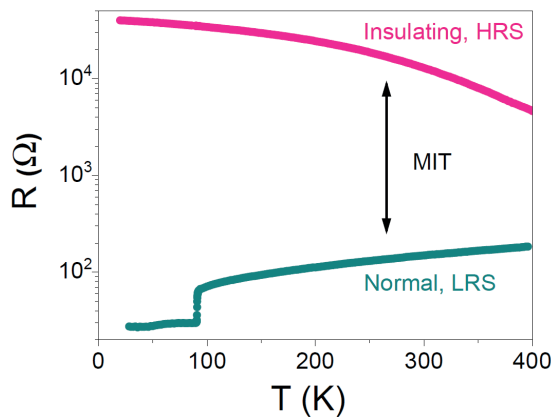


FIGURE 3.6: 2-point measurement temperature dependence of the high resistance state R_H and the low resistance state R_L in 250 nm thick and $30\ \mu\text{m}$ wide VERT-gate device.

The resistance ratio in both low and high temperatures can be increased by reducing the area of the gate electrode. Figure 3.7 displays the hysteresis loops obtained for gate electrodes with different areas. There is a significant increase of the hysteresis with decreasing areas, and this happens even applying lower gate voltages. The change in resistance can reach six orders of magnitude for a contact of $1\ \mu\text{m}^2$ area (hysteresis loop with black circles). The value of the resistances in both the LRS and the HRS were measured using a low voltage (0.1 V) in order not to change the state of the contacts. They were plotted as a function of the gate area in figure 3.7 (b). This area

dependence of the resistance can be explained assuming that the switching effect is homogeneously distributed underneath the electrode, excluding the filamentary switching mechanism typical in many oxides [132].

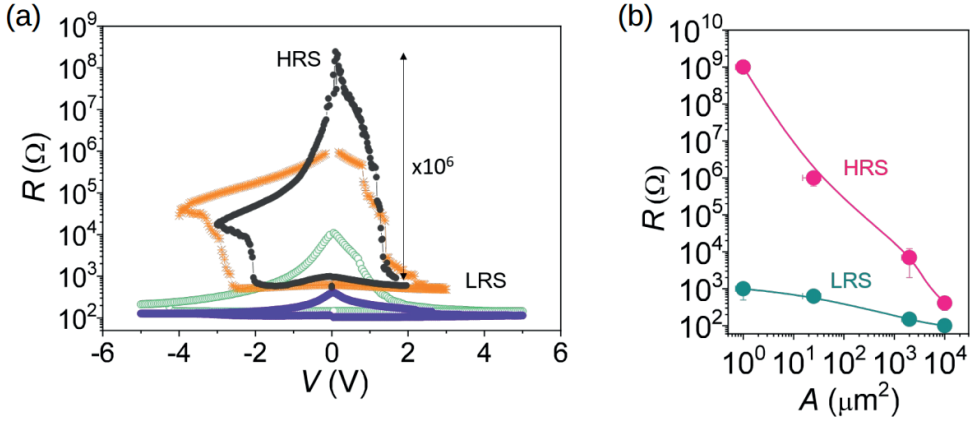


FIGURE 3.7: (a) Semilogarithmic R-V hysteresis loops measured in devices with different gate electrode areas. Orange stars for a contact area of $25 \mu\text{m}^2$, green empty circles for a contact area of $10^3 \mu\text{m}^2$, purple solid circles for a contact area of $10^4 \mu\text{m}^2$ and black solid circles for a contact area of $1 \mu\text{m}^2$. (b) Resistance at the HRS and LRS for the four gate areas, measured at 0.1 V).

Another interesting feature that can be exploited in these systems is the possibility to modulate the resistance by applying minor hysteresis loops. By applying different maximum voltages intermediate resistance states may be induced, each one related to a different oxygen content. In figure 3.8 several minor I-V loops measured in a 100 nm thick and 100 μm wide VERT-gate device are plotted. We observe that starting from a high resistance state the resistance can be reduced to different states by increasing the applied voltage. Inset shows the temperature dependence of the different resistance states obtained, which was measured in a 2-point configuration with the help of another non-switched electrode. An analog modulation of the resistance obtained through minor loops was already observed in other perovskites [14, 24, 133, 134].

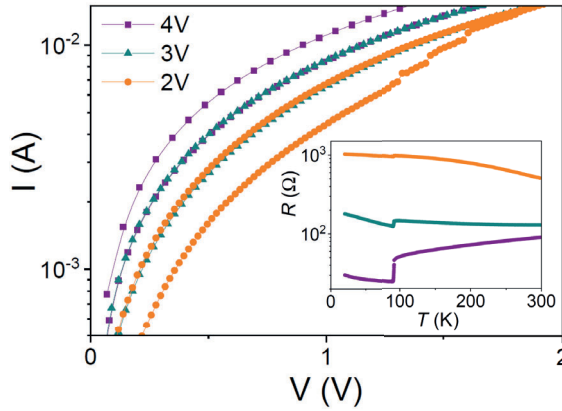


FIGURE 3.8: Minor loops measured of 2 V, 3 V and 4 V in a 100 nm thick VERT-gate device. A zoom in the voltage axis was done to show the switching in detail. Inset displays the temperature dependence of the three resistance states obtained.

A similar experiment was performed in a 150 nm thick and 10 μm wide VERT-gate device in order to evaluate the retention of the switching states. By applying different maximum voltages, different minor hysteresis loops were obtained (see figure 3.9 (a)). The evolution of the non-volatile resistance states with time was measured by using a low voltage (0.1 V) in order not to change the state. We observe that all the induced resistance states are very stable showing very good retention times (see figure 3.9 (b)), very suitable for multilevel memory performance or neuromorphic computing applications.

In the case of LAT-gate devices, having two switching gates the R-V and I-V curve obtained are more complex, since the complementary changes of the resistances of both electrodes are involved [125, 135]. For a given polarity one of the gates switches to the LRS and the other to the HRS and vice-versa. The following measurements were performed in a straight channel of width 50 μm and two gates separated by a distance of 200 μm . When applying a positive voltage, the contact with a positive bias incorporates oxygen and switches from the HRS to the LRS. This happens at a certain voltage, that we call V_{set} . The contact with a negative bias loses oxygen and switches from the LRS to the HRS. This also happens at a certain voltage, that we call V_{reset} . In figure 3.10 these voltages are indicated, for both contacts. It should be noted that V_{set} is lower than V_{reset} . This feature, which was always

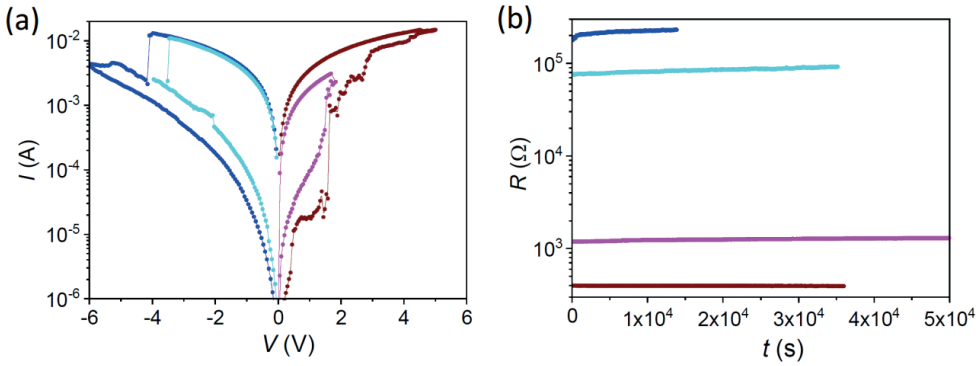


FIGURE 3.9: (a) Semilogarithmic resistance hysteresis loops measured in a 150 nm thick and 10 μm wide VERT-gate device that induce different resistance states. (b) Retention times for the obtained multilevel resistance states.

observed in all the measured devices is due to a faster motion of oxygen ions in the regions with lower conductivity, the ones in the HRS, and will be discussed later on. After sweeping the voltage to a certain value, in the way back to zero there are no more transitions, meaning that both contacts remain in the same non-volatile resistance state. The switching behavior is interchanged when applying a negative voltage. In this case, the contact with a negative bias switches from the HRS to the LRS and the contact with positive bias switches from the LRS to the HRS. If both gates are identical, the values of resistance of the HRS and the LRS and the voltages V_{set} and V_{reset} will be equal and symmetrical loops are obtained, as it happens in figure 3.10.

If we use different switching gates, having a different area or being made of a different material, their switching performance will be different and hence HRS, LRS, V_{set} and V_{reset} will change depending on the switching direction, obtaining asymmetrical I-V and R-V curves. This behavior can be observed in figure 3.11 (a), where very different switching voltages and final resistance values are obtained with a remarkable asymmetrical loop. Figure 3.11 (b) displays the asymmetrical curves obtained when the maximum applied voltage for the negative polarity is higher than V_{set} but lower than V_{reset} while for the positive polarity we apply a voltage higher than V_{set} and V_{reset} . By doing so, we switch just one of the contacts while the other remains always at the LRS.

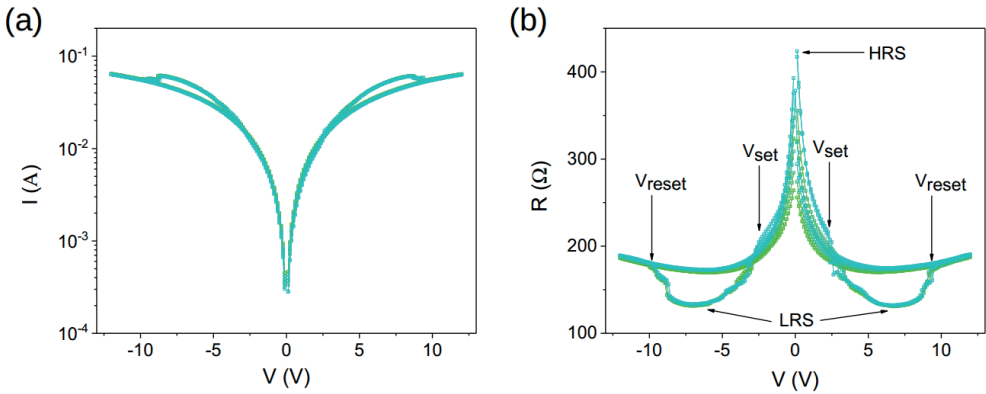


FIGURE 3.10: (a) I-V and (b) R-V symmetrical curves obtained in a two-point measurement in a YBCO channel $50 \mu\text{m}$ wide with two identical gates separated $200 \mu\text{m}$.

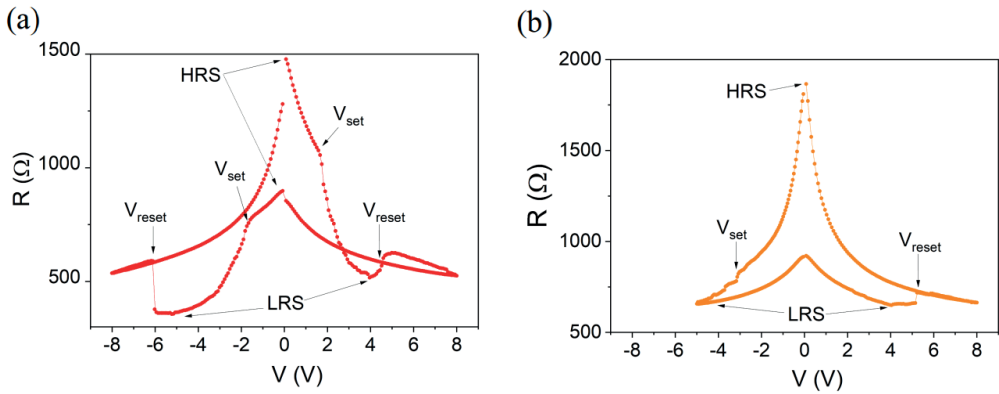


FIGURE 3.11: Asymmetrical R-V curves obtained (a) by applying symmetrical voltages in a device with two contacts with different switching performance, and (b) when applying asymmetrical voltages, with $V_{set} < V < V_{reset}$ for the negative polarity.

In order to better evaluate the switching behaviour of LAT-gate devices we performed resistive switching measurements between two identical gates in channels with different widths and distances between gates. We aim to study the influence of these parameters on the values of LRS, HRS, V_{set} and V_{reset} . Only the minimum voltage needed to reach V_{reset} in both polarities was applied. In figure 3.12 (a) we can see that both V_{set} and V_{reset} increase with the distance between the electrodes with an almost linear dependence.

From a linear fit, we can extract a constant parameter for the set electric field $E_{set} \sim (1 - 1.5) \times 10^4 V/m$ and the reset electric field ($E_{reset} \sim (1.5 - 2) \times 10^4 V/m$). It is worth to note that for gates separated $10 \mu m$, voltages of the order of $V \sim 2V$ are needed, thus expecting very competitive voltages (lower than $1V$) for practical applications if the device dimensions are reduced. We also observe that the values of V_{set} and V_{reset} do not significantly change with the device width. On the contrary, the values of LRS and HRS are clearly modulated by the width as observed in figure 3.12 (b). As we indicated in 3.11, we take the minimum value of the resistance to determine the LRS and the resistance value close to 0 V for the HRS. Both LRS and HRS increase with decreasing channel width, with a nearly linear dependence, except for the narrower channels. This deviation may be explained by the presence of edge effects or other fabrication factors that become more critical at small width values. The linear trend observed is consistent with a volume resistive switching effect, as expected.

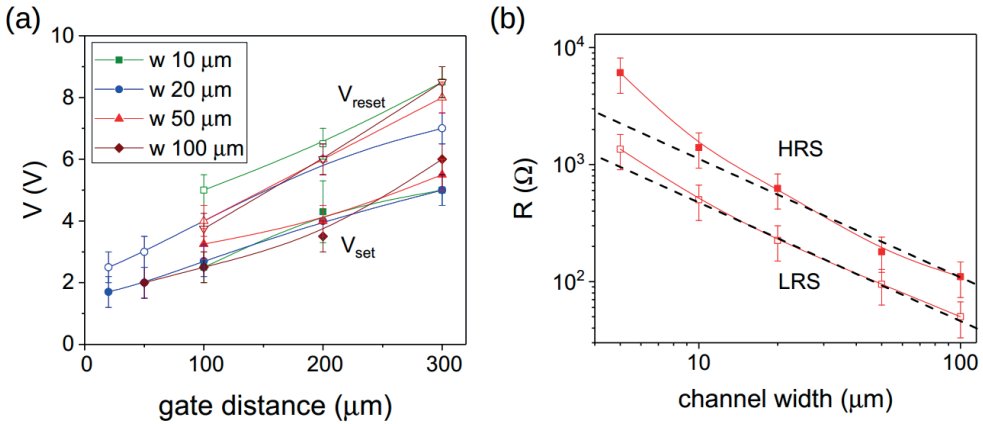


FIGURE 3.12: (a) V_{set} (closed symbols) and V_{reset} (open symbols) values as a function of the distance between the two switching gates, measured in devices of different widths. (b) LRS and HRS values as a function of the channel width. Dashed lines were included to illustrate the almost linear dependence.

3.3 Vertical oxygen diffusion

The experiments shown in the previous section were devoted to study the switching performance of one or two gates in a 2-point configuration. In this section we will study the oxygen distribution and associated change of the resistance at the bulk of the device. For that we will use devices with a transistor-like geometry (see figure 3.13) in which we tune the resistance of a drain-source channel with a gate. The volume change of the resistance below the gate is evaluated using a 4-point geometry by applying a very low reading current ($10^{-5}A$) within drain source and measuring the voltage using two electrodes connected to both sides of the gate. The devices with this configuration are called VERT-gate devices, and we have used them to study the field-induced vertical oxygen diffusion through the YBCO thickness.

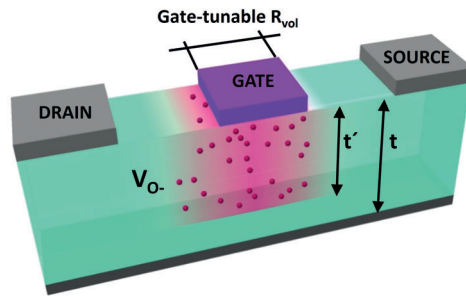


FIGURE 3.13: Sketch of the oxygen vacancy formation (V_{O-}) in a VERT-gate device, after switching the gate contact.

Figure 3.13 shows the expected oxygen diffusion in a VERT-gate device, with the diffusion of oxygen vacancies (V_{O-}) below the electrode when the gate is switched by applying voltage pulses. When a negative voltage is applied to the gate, oxygen migrates away from the electrode generating oxygen vacancies thus switching the volume to the HRS. The contrary happens if the polarity is reversed, oxygen moves towards the gate switching back the volume to the LRS.

Figure 3.14 (a) shows the evolution of R_{vol} in a 250 nm thick VERT-gate device, after applying several voltage pulses of $\pm 5V$ with positive and negative polarities in the gate electrode, at different temperatures. We see high and reversible changes in the four-contact resistance, meaning that we are generating electric-field induced volume oxygen doping in an

important volume below the gate electrode.

Assuming that a homogeneous switching below the electrode is induced and that the resistance at the HRS is much higher than the resistance at the LRS (as it can be seen in figure 3.6), the ratio of the volume resistance can be expressed as:

$$\frac{R_{vol}(HRS)}{R_{vol}(LRS)} = \frac{t}{t - t'} \quad (3.1)$$

being $R_{vol}(HRS)$ and $R_{vol}(LRS)$ the volume resistances of the bridge measured at the HRS and LRS respectively, t the thickness of the bridge and t' the switched thickness below the gate electrode (see figure 3.13). For this particular VERT-gate device we calculated the thicknesses of the switched volumes at different temperatures using the data from figure 3.14 (a) and plotted them in figure 3.14 (b).

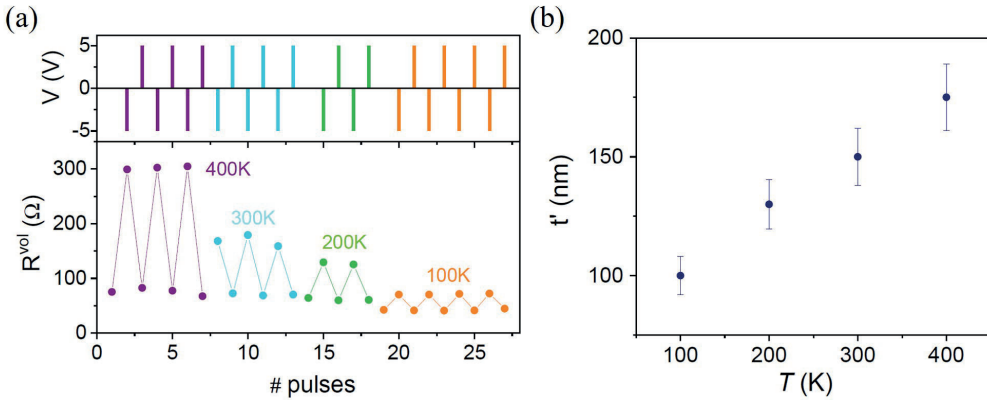


FIGURE 3.14: (a) Evolution of R_{vol} with different applied voltages at different temperatures. (b) Homogeneously switched thickness below the gate electrode calculated using equation 3.1, at different temperatures.

We observe that the volume that transits to the HRS increases with temperature, due to an increase of the oxygen mobility. Similar measurement performed in a device with lower thickness (VERT-gate 50nm thick and 30 μm wide) at 300 K, showed a ratio $R_{vol}(HRS)/R_{vol}LRS \sim 10^2$ (see figure 3.15). This very large ratio indicates that the whole thickness was transformed to an under-doped HRS after the voltage pulse. So, we can conclude

that designing a device with suitable geometry and thickness one can reversibly switch ON and OFF a drain source channel (superconducting channel if $T < T_c$) or part of it by properly tuning the applied voltage.

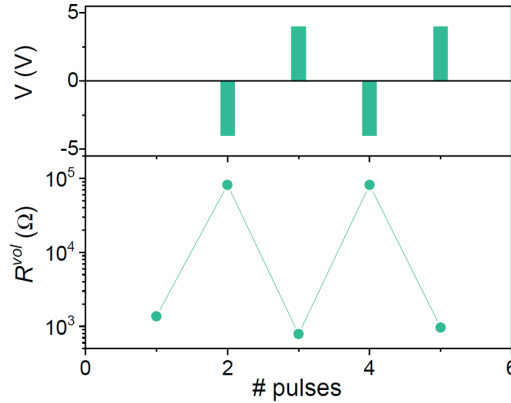


FIGURE 3.15: Applied voltages and volume resistance evolution measured in a 50 nm thick and 30 μm wide VERT-gate device.

Up to now, we have demonstrated that a reversible metal-insulator transition (MIT), with large resistance variations, can be induced above T_c by applying voltage pulses.

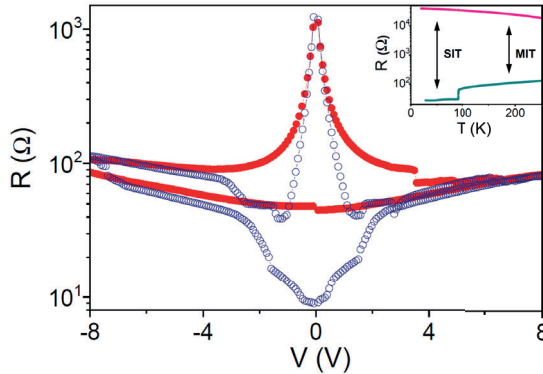


FIGURE 3.16: Switching loops obtained in a 250 nm thick and 100 μm wide VERT-gate device measured at 100K (orange dots) showing a MIT and at 80K (blue empty dots) showing a SIT. Inset illustrates both transitions.

The same effect can be induced by applying the voltage pulses below T_c thus generating a direct superconductor-insulator transition (SIT). Figure

3.16 shows the switching loops obtained in a VERT-gate device 250 nm thick and 100 μm wide at 100 K (above T_c) and at 80 K (below T_c). One clearly observes that reversible switching can be induced at both temperatures although the curve of the SIT switching loop is quite complex. We also observe an increase in the R_{HRS}/R_{LRS} ratio below T_c , as expected since the resistance drops at the superconducting state. The LRS value measured in the switching loop is attributed to the contact resistance.

3.4 Lateral oxygen diffusion

In this section we explore the possibility of inducing lateral oxygen diffusion through the YBCO channel by using two gates and taking advantage of the intrinsic anisotropic mobility of oxygen in cuprates. It is well-known that the oxygen diffusion coefficient along the $a - b$ planes (CuO_2 planes) is much higher than along the c -axis (across the CuO_2 planes), with a diffusion coefficient being up to six orders of magnitude higher ($D_{ab}/D_c \sim 10^6$).[120].

We designed a device with two gates in a top-top configuration, as depicted in figure 3.17 with a thickness of 100 nm and a width of 30 μm . In order to study the lateral oxygen motion within the device, we applied voltage pulses between the two gates while measuring the evolution of the volume resistance of the region within them by using external voltage contacts in a 4-point configuration.

Voltage sweeps of $\pm 15\text{V}$ were applied, obtaining the I-V and R-V curves plotted in figure 3.18. As we previously explained in section 3.2 (a) complementary switching behavior can be seen, since for both polarities if one contact switches to the LRS the other switches to HRS, and they do it in a reversible way. When applying a positive voltage, the contact with a positive bias switches from the HRS to the LRS (point 1 in figure 3.18), meanwhile the contact with a negative bias switches from the LRS to the HRS (point 2). Going back to zero voltage there are no more transitions, meaning that both contacts remain in the same resistance state. This behavior is interchanged when applying a negative voltage, the contact with a negative bias switches from the HRS to the LRS state (point 3) and the contact with positive bias switches from the LRS to the HRS state (point

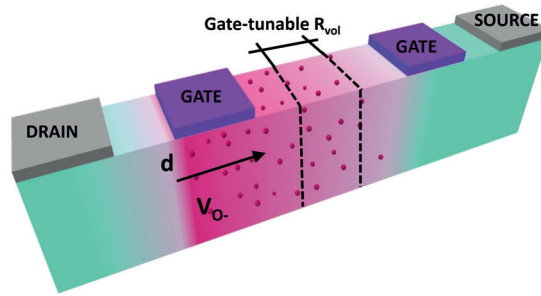


FIGURE 3.17: Sketch of the lateral oxygen diffusion induced in a LAT-gate device, with the left contact in HRS. The volume resistance will be measured in the region marked with black dashed lines in a 4-point configuration.

4). For this particular device we see that the value $V_{HRS \rightarrow LRS}$ is close to 4 V while the value $V_{LRS \rightarrow HRS}$ is close to 12 V. Thus, as previously described if the applied voltage is between $V_{HRS \rightarrow LRS}$ and $V_{LRS \rightarrow HRS}$ for one of the polarities ($V_{HRS \rightarrow LRS} < V < V_{LRS \rightarrow HRS}$) only one of the contacts can switch, while the other will remain in the LRS. The resulting asymmetrical loops are shown in the insets of figure 3.18.

Figure 3.19 shows the temperature dependence of the volume resistance of a region between the switching contacts (marked with dashed lines in figure 3.17) using a 4-point configuration after performing different switching cycles. The RT curve with black stars corresponds to the pristine state, with the expected sharp superconducting transition at 90 K. The RT curve with pink open circles was measured after a voltage of +15 V was applied between the gate electrodes. The behavior is still metallic, but the superconducting transition was shifted around 40 K. Nevertheless, there

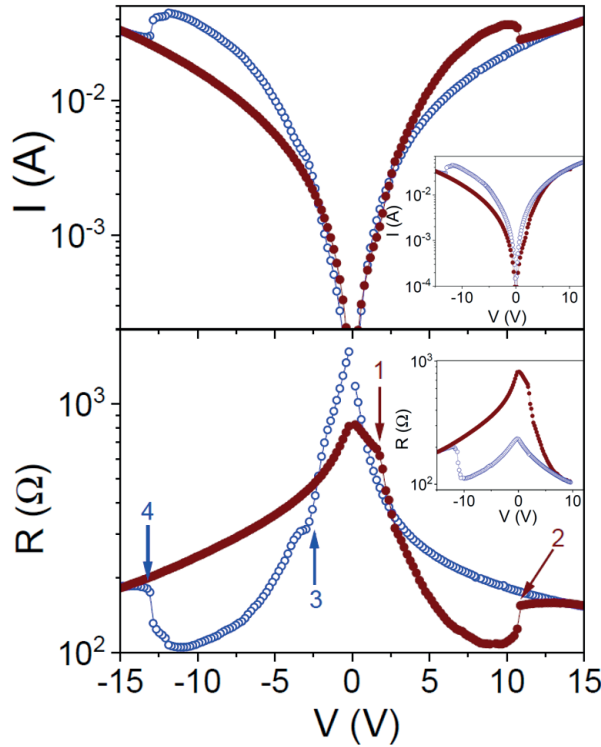


FIGURE 3.18: Semilogarithmic I-V (top) and R-V (bottom) in a two terminal LAT-gate device. Solid and open circles correspond to increasing and decreasing voltage sweeps, respectively. Arrows 1 and 3 indicate the complementary transitions from HRS to LRS of both gates. Arrows 2 and 4 indicate the complementary transition from LRS to HRS of both gates. The plots in the insets show the asymmetric curves obtained when only one of the contacts is switched.

is still a partial superconducting transition at around 80 K, meaning that not all the tested volume was driven to the same HRS. After applying a voltage of -15 V we measured the RT curve with green full circles, which again shows a sharp superconducting transition close to 90 K and even the normal state resistance (at 300 K) is lower than the one in the pristine state. It is important to note that a reversible change in the T_c of around 40 K was achieved, meaning that a good quantity of oxygen has been reversible diffused, hundreds of microns away from the switching contacts. In these experiments both lateral and vertical oxygen diffusion take place, so the modulation of the volume resistance depends a lot on the volume

of the drain-source channel considered. This kind of devices can be also interesting to emulate the transistor-like behavior, already mentioned in a previous section.

The evolution of the resistance measured in each of the gates using an external contact in a two-point configuration is plotted in the inset of figure 3.19. We clearly see that after applying a voltage of a certain polarity, the RT curve of one of the contacts shows an insulating behavior and the other a metallic (superconducting) behavior, corresponding to the contact in HRS and in LRS respectively. The opposite behavior is observed if the polarity is reversed. This measurement reinforces our interpretation of the I-V and R-V loops in figure 3.18.

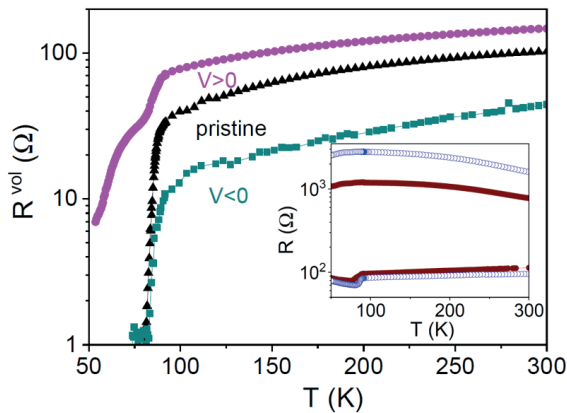


FIGURE 3.19: RT curves of the volume resistance in a LAT-gate device at the pristine state (black stars), after a positive voltage is applied (empty pink circles) and after a negative voltage is applied (green full circles). Inset shows the RT curve below both switching contacts after a positive voltage is applied (open blue circles) and after a negative voltage is applied (full red circles), measured in a two-point configuration.

Similar experiments were performed in a LAT-gate device (100 nm thick and 30 μm wide), but in this case we evaluated the change of the volume resistance in a region close to one of the two switching contacts instead of measuring the central part. Different voltages with both positive and negative polarities were applied, inducing several intermediate reversible transitions going from an under-doped insulating state to the optimally doped superconducting state (see figure 3.20). We also observe that in all the RT

curves a first transition at a temperature close to 90 K appears. This means that a part of the volume has not been switched to the HRS. The percentage of the un-switched volume decreases with increasing voltage. This could be exploited for multilevel memory performance, with potential application in neuromorphic computing.

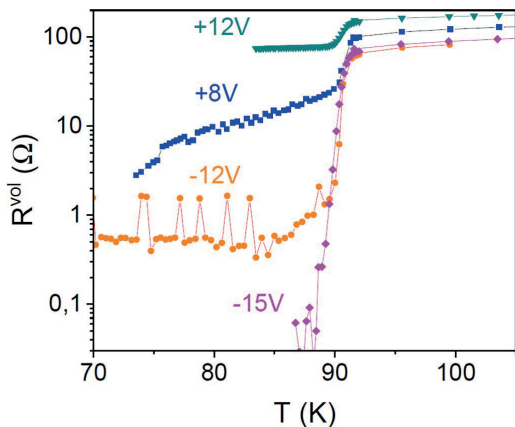


FIGURE 3.20: RT curves of the volume resistance in a LAT-gate device after applying different voltages, indicated at each curve.

3.4.1 Local evaluation of field-induced oxygen diffusion

Micro-Raman spectroscopy was performed to confirm the lateral motion of oxygen atoms in our devices, induced by resistive switching. This technique permits to measure the frequency of the phonon vibration modes in YBCO. In particular, a shift in the phonon mode frequency ω_{o4} is originated in the variation of the c-cell parameter with the oxygen content. When the latter decreases there is a bond softening and the unit cell expands, so the c-cell parameter increases and therefore the phonon frequency decreases too. See section 2.5.2 for more details about the technique, how we performed the experiments and analyzed the data.

As previously described in the experimental section, the linear dependence of the phonon frequency with oxygen content, can be used to calculate the local amount of oxygen using equation 3.2, an empirical law calculated in [108].

$$\delta = 13.58 - 0.027\omega_o \quad (3.2)$$

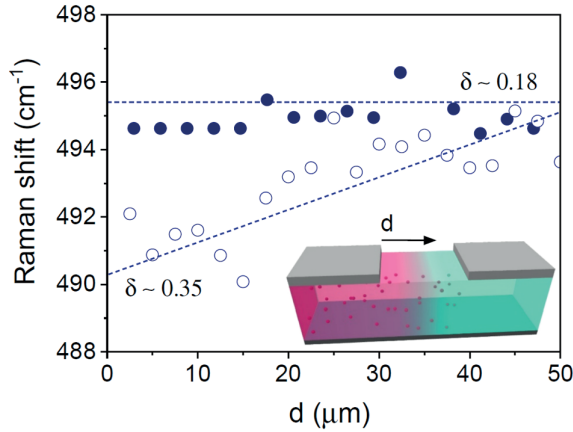


FIGURE 3.21: Raman phonon frequency measured at different points along the studied track both in pristine state and after switching the left contact to HRS. Inset shows the geometry of the track and an illustrative distribution of the oxygen vacancies (dark red points).

A patterned track in a 100 nm thick YBCO film with a length of 250 μm length and a width of 50 μm was used. Voltage pulses were applied between two contacts located at the edges of the track (see inset in figure 3.21). We recorded two linear scans along 50 μm at the centre of the track, one at the pristine state and another one after the voltage pulse. Figure 3.21 shows the evolution of the phonon frequency measured on the pristine state (closed symbols) were a constant value of about 495.4 cm^{-1} is obtained with a mean value of $\delta \sim 0.18$, in agreement with an optimally doped state. Measurements performed after switching the left contact to the high resistance state (HRS) (open symbols) show a clear evolution of the oxygen doping, with a value of $\delta \sim 0.35$ at the region close to the switched contact, confirming the formation of oxygen vacancies.

A quantitative evaluation of the lateral distance of oxygen diffusion in our LAT-gate devices has been performed by reversibly switching one of the contacts, using the minimum voltage sweep rates available in the experimental setup used ($\tau \sim 100\text{ms}$) and checking that the volume resistance of

the central bridge located at a distance $d = 300\mu m$ is reversibly changed.

With these values we can determine a lower limit for the field-induced effective oxygen diffusion coefficient along the a-b planes ($D_{ab} \sim d^2/\tau$) at room temperature. The value obtained is $\sim 10^{-2}cm^2/s$, ten orders of magnitude higher than the ones reported for thermally activated oxygen diffusion in YBCO single crystals [136]. Such a high value can be understood considering the extremely large gradients of electric field generated between the HRS and the LRS regions, later calculated in numerical simulations and shown in figure 3.23 (b)). Assuming the obtained lower limit value of the electric field-induced oxygen diffusion, the estimated speed for switching of oxygen vacancies, along the a-b planes, in a device of hundreds of nanometers would be of the order of 10 ns, which is in the range of what is required for high performance, high-speed memory devices.

3.4.2 Numerical simulations

In order to better understand the dynamics of the oxygen and its role in the resistive switching phenomenon we did numerical simulations by using a model described in the experimental section. The model consider two contributions for oxygen diffusion: thermal activation and electric field induced oxygen motion. A scheme of the simulation domain can be seen in figure 3.22 (a), showing the two top electrodes and the boundary conditions applied, being J_n the electric current normal to the surface. The red dashed lines show the segment chosen to calculate the hysteresis loops depicted in (c). Blue dotted line shows the cross section used to calculate the I-V characteristics depicted in figure 3.24 (a).

Figure 3.22 (b) shows the evolution of the oxygen concentration (c) in 9 different steps of the simulation of a switching cycle. The colors in the main part of the simulation domain correspond to the oxygen concentration as is depicted in the scale bar. The color in the contacts correspond to the applied bias voltage (V_{bias}), with red color for the positive voltage and blue for the negative, with different intensities. A V_{bias} with a sinusoidal driving voltage of $\pm 2.5V$ at a frequency of 50 Hz is applied in the left contact, while the right contact is grounded. The nine stages were taken every 2.5 ms. Step #1 corresponds to a initial stable configuration, with no voltage applied ($V_{bias} = 0V$), with the left contact in the HRS and the right contact

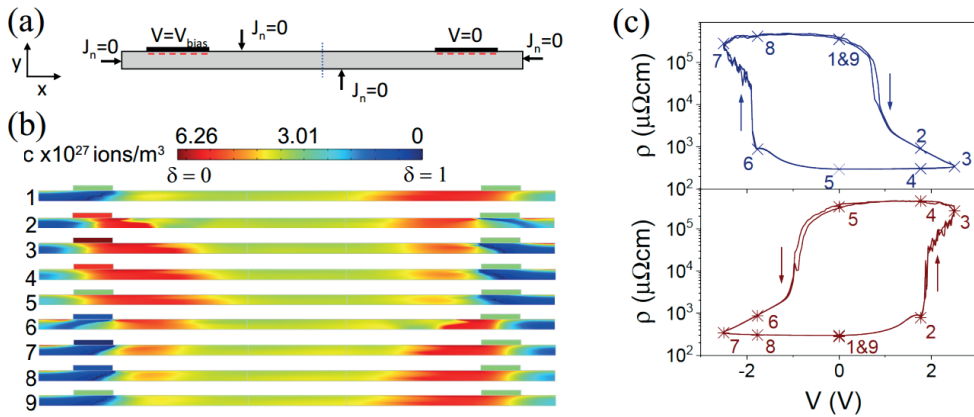


FIGURE 3.22: (a) Scheme of the simulation domain and the boundary conditions. Blue dotted line indicate the cross section and red dashed lines indicate the segment where the hysteresis loops in (c) were calculated. (b) Simulation of the evolution the oxygen concentration in different stages of the switching process, following the color scale (optimally doped to under-doped from red to blue). (c) Hysteresis loops of the resistivity in a segment below the left (top) and right (bottom) contacts. The numbers correspond to the ones in (b).

in the LRS. In step #2 we polarize the left contact with a positive voltage of +1.76V and we observe a clear enhancement of oxygen concentration at the bottom of the left contact and oxygen vacancies that are generated at the right one. In step #3 the voltage reaches its highest value (2.5 V) and both the HRS and the LRS areas are enlarged. It is worth noting that due to the material anisotropy imposed by the conductivity and diffusivity tensors (σ and D) and specially the large domain aspect ratio, ionic carriers move anisotropically, creating a lateral oxygen diffusion of hundreds of microns away from the contacts, as experimentally observed. In steps #4 and #5 we observe that the HRS and LRS areas remain while decreasing the voltage back to zero. This means that the effects are non-volatile and confirms our experimental results. In step #6 the polarity is reversed and we observe that the oxygen concentration decreases below the left contact (oxygen vacancies are created) and increases below the right contact. Steps #7 and #8 show the evolution of the oxygen concentration with a negative voltage pulse until the starting position is recovered at 0V (step #9). The enhancement/reduction of the oxygen concentration in the areas surrounding the

contacts occurs through the generation/annihilation of oxygen vacancies in the nearby region. The net change of the oxygen concentration in a given volume located along the bridge (away from the contacts) will strongly depend on the initial conditions of our system (contact resistance, initial oxygen doping, and lateral and vertical dimensions), offering high degree of freedom in device design.

Figure 3.22 (c) displays the evolution of the average resistivity determined considering a segment of $20\mu\text{m}$, placed $1\mu\text{m}$ below the contact, as indicated with red dashed lines in figure 3.22 (a). The upper plot corresponds to the region below the left contact and the lower one to the region below the right contact. The numbers correspond to each of the steps shown in figure 3.22 (b). The average resistivity is calculated using the diagonal values of the conductivity tensor, which is determined from the oxygen concentration at each point.

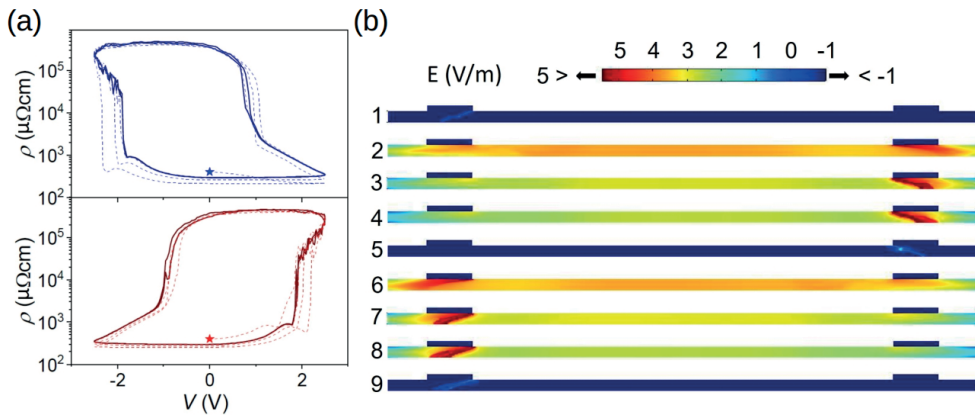


FIGURE 3.23: (a) Simulated hysteresis loops with resistance of the initial point is indicated with a star. Dashed lines show the evolution of the switching to a stable performance (solid lines). (b) Electric field induced at different stages of the switching process. The colors represent the value of the electric field in logarithmic scale.

The hysteresis curves correspond to stable switching characteristics, achieved after several loops, starting from an initial homogeneous oxygen concentration. All simulated hysteresis loops are shown in figure 3.23 (a), where the initial point is indicated with a star, and the loops evolve from

the ones with dashed lines to the stable loops plotted with solid lines. As expected a complementary switching behavior is found where for a positive voltage the region below the left contact switches to the LRS and the region below the right contact switches to the HRS. With negative polarity we obtain the opposite situation. Simulations also show that the transition from HRS to LRS occurs at lower voltages than the transition from LRS to HRS, which agrees with the experimental results. This asymmetry in the switching voltage, observed in all measured devices, is explained due to the fast motion of oxygen in the low conductivity regions where extremely large values of electric field are induced (see figure 3.23 (b)).

Figure 3.24 (a) shows the simulated I-V curves of the system determined considering the entire section of the domain (blue dotted line in figure 3.22 (a)). The red curve corresponds to the current measured when increasing the applied voltage and the blue curve corresponds to the current measured when decreasing the applied voltage. Figure 3.24 (b) shows the experimental I-V curves measured for the device described in figure 3.18), plotted in linear scale. Again, the close red symbols correspond to an increasing voltage sweep and open blue symbols to a decreasing voltage sweep. A good agreement between experimental and simulation is obtained thus validating our theoretical approach.

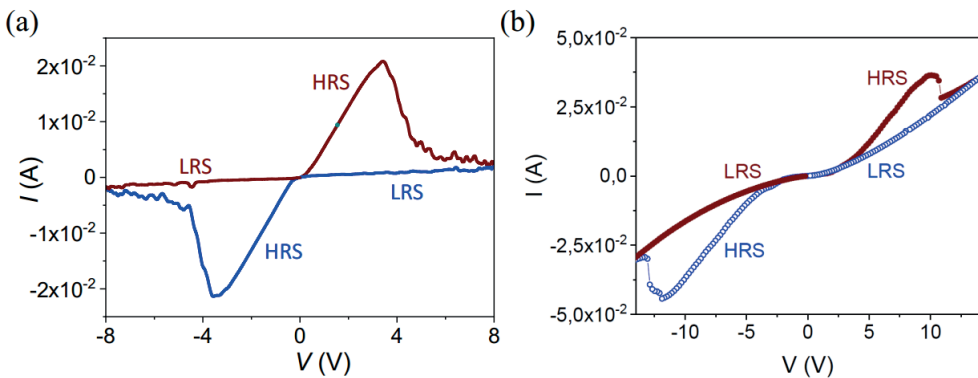


FIGURE 3.24: (a) I-V hysteresis loops from the simulations in the cross section of the domain. (b) I-V hysteresis characteristics shown in figure 3.18. In both graphs red and blue lines/symbols represent the sweeps performed by increasing and decreasing the voltage, respectively.

3.5 Conclusions

In this chapter we demonstrated the possibility of tuning the carrier density in YBCO thin films, through electric-field induced oxygen diffusion, with the possibility of attaining metal-insulator transitions, changes in T_c and other normal state properties, in a non-volatile reversible way. By means of electric transport measurements we could show that this effect is not only confined to the vicinity of the interface gate-film but it can reach tunable volumes of the material, and also that both vertical and lateral oxygen diffusion can be induced through proper device design. We also showed high performance bipolar reversible non-volatile resistive switching in our devices. When working below T_c we could induce direct superconductor-insulator transitions, meaning that we can locally switch on and off its outstanding macroscopic quantum coherence superconducting state.

Reversible field-induced oxygen doping effects were also confirmed with micro-Raman spectroscopy experiments and are in good agreement with the simulations performed in the frame of a theoretical model in which both the thermally activated diffusion and the electric field induced oxygen mobility within the film are responsible for the oxygen dynamics.

The switching properties of our devices can be used for the design of next-generation non-volatile resistive memory and logic devices with high flexibility. The acquired control of the volumic oxygen diffusion can be used to design multi-terminal transistor-like devices, ideal for gate-controlled logic or neuromorphic applications, with the possibility of exploiting its superconducting phase for tuning a zero-resistance channel. Fine control of the oxygen content in confined regions could be a very useful tool to systematically study the phases present in the complex doping phase diagram of cuprates by using a single material.

Chapter 4

Electromigration in YBCO thin films

The Electromigration (EM) effect is the migration of atoms in a conductor due to the directional momentum transfer of charge carriers. This is a thermally activated phenomenon which is particularly important in integrated circuits [137], where high current densities are applied, increasing with decreasing dimensions. It can also spoil plasmonic materials [138, 139] or spintronic devices if they have to sustain large current densities, like in domain-wall memories [140, 141].

In the case of superconducting nanocircuits, when working in the superconducting state, there is no interaction between the carriers (Cooper pairs) and the lattice, so there is no momentum transfer and hence no dissipation or electromigration effects. Furthermore, the superconducting critical current density (J_c) is usually much lower than the current density needed to trigger the electromigration, known as electromigration current density (J_{em}) [142]. However, cuprate high-temperature superconductors present a very high J_c and a weak atomic diffusion barrier for oxygen atoms to move [117, 143–145], thus lowering the value of J_{em} . This means that when reaching the dissipate state ($J > J_c$), J_{em} could be exceeded and electromigration effects can take place. In this case, the material may be deoxygenated or damaged, limiting the endurance of devices working at the edge of the superconducting dissipative state, such as single photon detectors [146].

In this chapter we aim to study the electromigration phenomena in micro-metric patterned YBCO bridges. Current stimulated oxygen diffusion will be induced by controlled electromigration processes and its

effect on the properties of the material will be evaluated by using different techniques such as, optical microscope imaging, transport measurements in properly designed devices (Hall and R(T) curves) and micro-Raman spectroscopy. We will compare the temperature dependence of both J_c and J_{em} to study the possible material damage when reaching the dissipative state. We also will explore the possibility of controlling the electromigration process for a selective migration of oxygen atoms that could be used to tune the oxygen content in YBCO, inducing a MIT as discussed in the previous sections. We will see that proper tuning of the electromigration effect can be used for a systematic study of the complex phase diagram of cuprates [147]. With this approach one can selectively tune the oxygen content in a single sample and thus one does not need to grow samples with different oxygen content to be compared.

4.1 Electromigration current density (J_{em})

Devices with a 4-point geometry (bow-tie shape) with a narrow bridge of width 1-2 μm and length 2-3 μm were designed and fabricated (see figure 4.1 (a)). YBCO films grown by chemical solution deposition (CSD) with a thickness of 100 nm were used. These devices were physically etched with an ion-milling system. The metallic electrodes on the devices were silver annealed contacts of thickness 200 nm and area $300 \times 300 \mu\text{m}^2$.

The EM studies were performed in collaboration with the team of Prof. A. Silhanek from Université de Liège, with a specifically designed experimental set-up. Using a homemade software, the voltage bias is ramped up while monitoring the change in conductance dG/dt and keeping it in a preset range with a feedback loop, measuring with a nanovoltmeter and an amperemeter. A detailed explanation of the process followed can be found in [97, 98]. It should be noted that the optimization of the electromigration process, the characterization of the temperature dependence of the electromigration current density in our YBCO patterned films and the optical imaging of oxygen motion was performed by the group of A. Silhanek at Liège. We include these measurements here for completeness [98, 148].

R(I) curves (figure 4.1 (b)) were measured at 110 K, right above T_c . At low currents the resistance has an almost parabolic behavior that can be

explained by the combination of Joule heating effects that rise the temperature and the temperature dependent resistance. For this particular sample, when current reaches 12 mA a change in the slope can be clearly observed, indicating that the electromigration has started. This is confirmed by the fact that from that point on, although less current is applied the resistance keeps increasing. Using the value of the current at which the electromigration starts (12 mA) and the dimensions of the bridge we can calculate the corresponding electromigration current density $J_{em} \sim 7.8 MA/cm^2$.

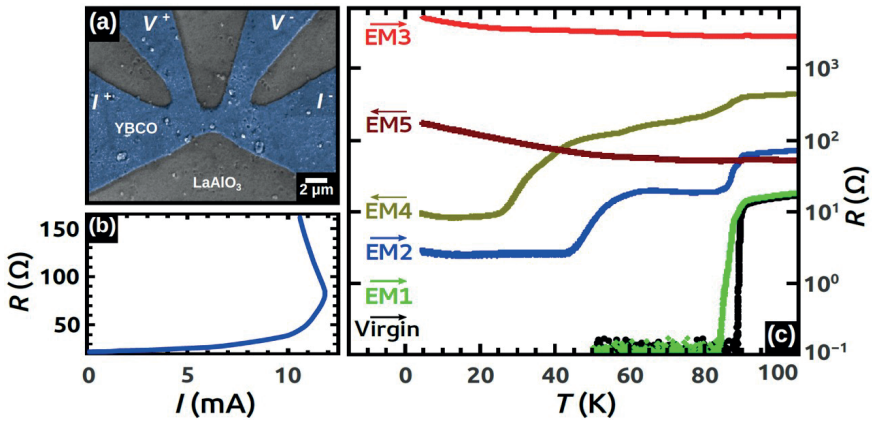


FIGURE 4.1: (a) SEM image of a YBCO device with 4-point "bow-tie" geometry. (b) $R(I)$ curve measured during the EM run at 110 K. (c) $R(T)$ characteristics after the different electromigration (EM) steps. The arrows indicate the current direction during the electromigration step.

Since we are interested on the influence of the EM in the properties of our YBCO films we measured a $R(T)$ curve with the sample in its virgin state and then after each EM run in the same device. As seen in figure 4.1 (c), after each electromigration the T_c decreases and the normal state resistance increases (EM1, EM2 and EM3). Both magnitudes are directly related to the local oxygen doping level [100, 121], so this scenario is compatible with that every electromigration run produces a displacement of oxygen atoms from the constriction, reducing the local doping [117, 149, 150]. After EM1 there is only a small decrease of T_c and an increase of the transition width as compared with the virgin state. In the $R(T)$ curve after EM2 a two-step shape is observed with a clear enhancement of the normal

state resistance. The two step behavior can be attributed to the existence of two parts of the bridge with different oxygen doping due to the fact that major electromigration effects are mainly happening in the narrowest part of the structure with higher current density. In the R(T) curve after EM3 an insulating behavior is observed, meaning that oxygen atoms have been displaced from all the bridge.

Assuming this scenario it is straightforward to think that if the polarity of the bias current is reversed the bridge can be “healed” through an antielectromigration (anti-EM) process. This is what happened in the case of voltage induced oxygen motion as discussed in the previous chapter, and worked considerably well with current stimulated atomic diffusion in elemental materials like platinum[149, 151–155]. An anti-EM run was thus induced in EM4 R(T) where we observe a reduction of the normal state resistance as compared with EM3 and the re-appearance of a two-steep superconducting transition meaning that we managed to partially heal the bridge. A second anti-EM run was induced in EM5 but in this case an insulator behavior was obtained with a slightly lower normal state resistance. Following runs degraded even more the properties of the device. It should be noted that in EM2 and EM4 the resistance of the sample remains finite at low temperatures and exhibit very broad transitions as temperature increases. This can be explained by the existence of an important gradient of the oxygen concentration along the bridge which results from the variation of the current density at different points of the bridge depending on the width.

The determination of the value of the electromigration current density J_{em} performed in the previous experiment is not accurate since resistance changes are not only associated to pure EM but also to heating effects. In order to assure a more accurate determination of J_{em} pulsed current measurements were performed, following the scheme in the inset of figure 4.2. They consisted on pulses with linearly increasing current I_{max} with constant width $\delta t = 1 \text{ ms}$ low current bias $I_{min} = 100 \mu A$ to monitor the resistance of the bridge between the pulses. The time separation between two consecutive pulses $\Delta t = 10 \text{ s}$ was chosen to ensure total thermalization of the sample to the surrounding bath temperature after every pulse. The time needed to achieve a thermal stationary state is in the order of nanoseconds but the time scale of an electromigration process depends

on the material [156] and is in the order of seconds. Similar procedure was followed in [157].

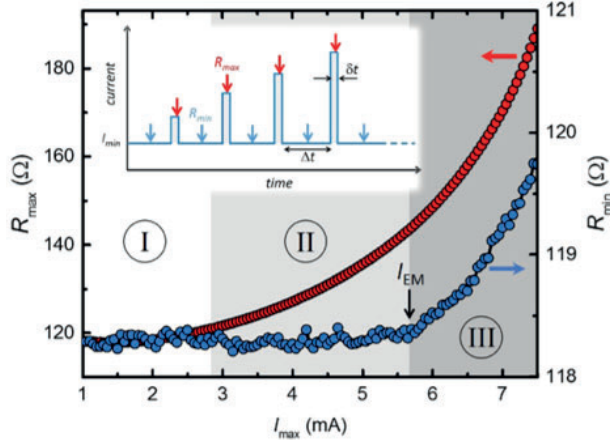


FIGURE 4.2: Inset: schematic representation of the EM procedure with pulsed current. Main panel: R_{min} (blue points) and R_{max} (red points) as a function of I_{max} for YBCO at 300 K. Regions I, II and III are represented with different colors.

In figure 4.2 we plot the values of the resistance as a function of I_{max} . Blue points show the resistance recorded between two consecutive pulses (R_{min}) and red points the value of the resistance recorded at the end of the flat top of the applied pulse. The measuring program stops the train of pulses when R_{min} increases 1%. Three different regimes in the graph can be differentiated. In region I, where I_{max} is low, $R_{max} = R_{min}$, meaning that Joule heating effects are negligible. In region II, with intermediate I_{max} Joule heating effects appear and the two measured resistance values are not coincident, being the one measured during the pulse higher ($R_{max} > R_{min}$). In region III a change in the slope of R_{min} can be observed. We define that value of I_{max} as the electromigration current I_{em} where electromigration process starts.

4.2 Critical current density (J_c) vs electromigration current density (J_{em})

In the following experiments we wanted to compare the temperature dependence of both the superconducting critical current density (J_c) and the electromigration current density (J_{em}).

We determined the J_c of our device by measuring the typical V(I) curves at different temperatures (see figure 4.3 (a)). Two different critical current densities were defined. J_{c1} is defined as the current density with which dissipation starts, when a voltage of $50 \mu\text{V}$ is reached. J_{c2} is the current density at which a jump to a highly dissipative state happens, marked with vertical arrows in figure 4.3 (a).

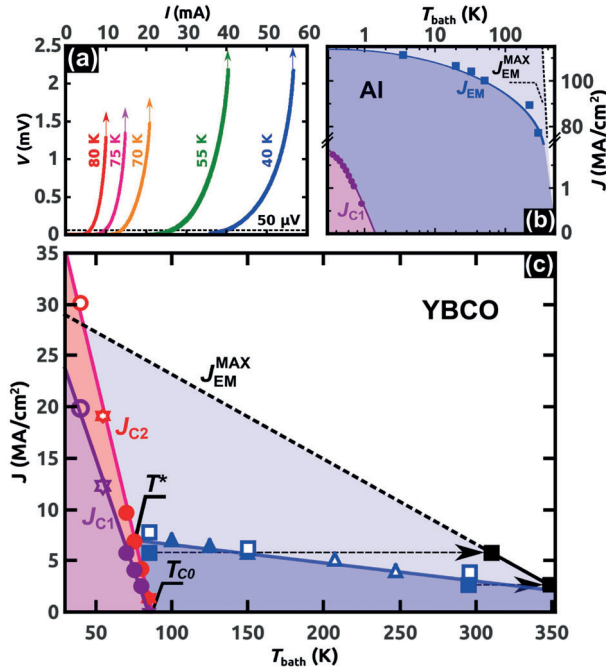


FIGURE 4.3: (a) V(I) characteristics at several temperatures used to determine the J_c . Critical current and electromigration current densities for Al (b) and YBCO (c) constrictions, as a function of T_{bath} .

In general, the electromigration current density for all superconducting devices is higher than critical current density $J_{em} > J_c$ for all the temperatures and thus electromigration effects are not an issue. In the case of aluminum (Al) $J_{em} \gg J_c$ as we can see in figure 4.3 (b). A similar trend is also observed in another cuprate superconductors, $La_{2-x}Ce_xCuO_4$ (LCCO). In this material J_{em} at 50 K is 13 MA/cm² [149], much higher than J_c at 0 K (~ 0.02 MA/cm²) [158].

However, in case of YBCO the critical current density may exceed J_{em} at some temperatures. Figure 4.3 (c) shows the measured points of J_{c1} , J_{c2} and J_{em} and the linear trend of them as a function of T_{bath} . In this experiment we should differentiate the temperature set in the cryostat (T_{bath}) from the actual temperature in the constriction (T_{local}) which may be much higher due to heating effects. We observe from the figure that the lines $J_{c2}(T_{bath})$ and $J_{em}(T_{bath})$ cross at a temperature $T^* \sim 75$ K. Thus, in the range of temperatures $T^* < T_{bath} < T_c$ it is possible to reach the normal state avoiding damaging due to electromigration effects if $J_{c2} < J < J_{em}$. On the other hand, for temperatures $T_{bath} < T^*$ degradation of the material due to electromigration can occur if no feedback loops are used to control the process. It should be noted that a substantial shift of the electromigration current up to $J_{c2} < J < J_{em}^{max}$ is expected if heating effects within the cryostat are reduced.

4.3 Selective tuning of the oxygen content in YBCO bridges

In this section we explore the possibility to tune the oxygen content in specially designed superconducting bridges through electromigration effects. This study complements the gate-induced electric field oxygen doping discussed in the previous chapter. In this case however, local oxygen doping will be induced through electromigration processes and analyzed by optical microscopy, Raman spectroscopy, and transport measurements.

4.3.1 Direct visualization of electromigration

In order to unveil the directed migration of oxygen atoms through electromigration effects we use optical imaging at cryogenic conditions at different points of the electromigration run. The $R(I)$ curve in figure 4.4 we observe that the the electromigration process starts at $I = 12 \text{ mA}$ (corresponding to $J_{em} \sim 8 \text{ MA/cm}^2$). The inset in figure 4.4 shows the time evolution of the circulating current were one can see that the process took several hours.

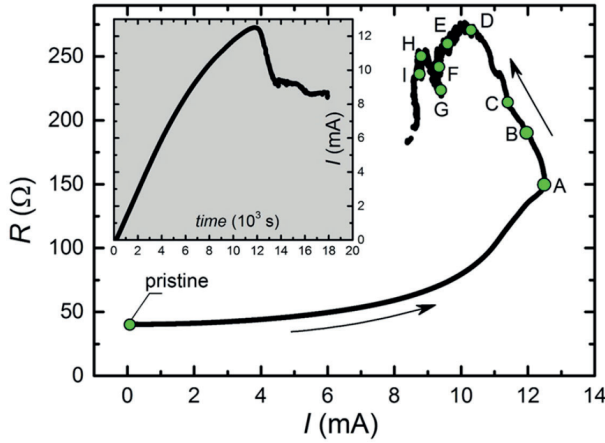


FIGURE 4.4: $R(I)$ curve measured during an EM process. The time evolution of the measurement is indicated by the black arrows. Inset: Time evolution of the current $I(t)$ during the same EM process.

Figure 4.5 shows false colored optical microscope differential images obtained at 105 K at different points of the electromigration run, revealing the evolution of the area affected by the electromigration process. The white lines delineated the borders of the device.

The evolution of the area affected by the EM is easily distinguished as darker regions, highlighted with vertical black arrows. As we will see in the following electromigrated region can also be identified using bright-field optical images since the oxygen-depleted zones in YBCO show higher reflectivity [117, 159]. We observe that changes in the optical response are more pronounced close to the cathode and thus the effect cannot be attributed to Joule heating because it should be symmetric. The main carriers

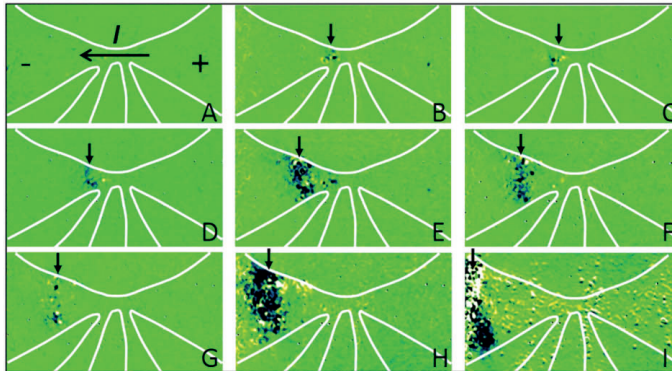


FIGURE 4.5: Differential images showing the evolution of the affected region. The polarity is indicated by the black arrow in figure A. The labels correspond to the points indicated in panel a. The white curve delineates the borders of the transport bridge, and the vertical black arrows indicate the mean position of the propagating front.

in the sample are holes which flow from right to left (towards the negative cathode) in the same direction as the oxygen vacancies. It should also be noted that there is a mixture of high-intensity and low-intensity points in the oxygen depleted regions which may indicate an inhomogeneous distribution of oxygen vacancies.

4.3.2 Transport measurements

Transport measurements were performed on 100 nm thick YBCO superconducting thin films grown either by chemical solution deposition (CSD) and pulsed laser deposition (PLD) with no main differences in the results obtained. Samples were patterned with a structure consisting of a narrow central bridge symmetrically surrounded by wider bridges, each bridge individually addressable by corresponding current and voltage contacts in a 4-point geometry. The central bridge has a width of $0.8\mu\text{m}$, the two symmetrically placed lateral bridges $3\mu\text{m}$ (see figure 4.6 (a)). A magneto-optical image of the device was obtained at $T=4.5\text{ K}$ and $\mu_0 H = 0.95\text{ mT}$, showing the expulsion of the magnetic flux from the superconducting patterned film. The light bright blue areas correspond to the regions with high magnetic fields (the substrate) and the dark areas correspond to the regions where

magnetic flux is expelled (patterned superconducting YBCO). The homogeneity of the magnetic flux expulsion denotes the absence of macroscopic defects and the high quality of our YBCO thin films.

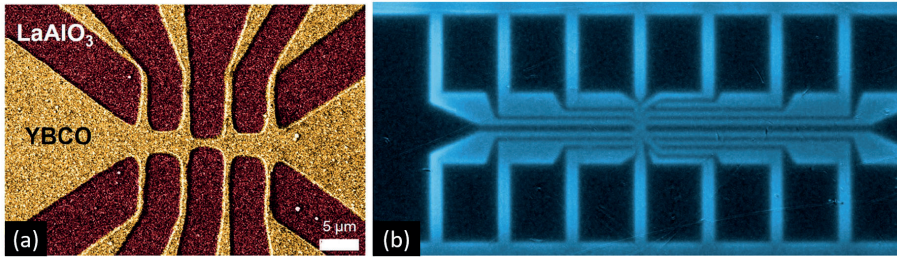


FIGURE 4.6: Scanning electron microscopy image of the central part of a three-bridges device. (b) Magneto-optical image of the whole device obtained at $T = 4.5 K$ and $\mu_0 H = 0.95 mT$.

$R(T)$ curves measured for each of the three bridges in the pristine state are shown in figure 4.7 (a). In order to facilitate the comprehension of the data, we colored in red the left bridge, in green the central bridge and in blue the right bridge (see the inset in figure 4.8 (a)), matching with the colors of the $R(T)$ curves. We plotted the normalized resistance $R(T)/R(200K)$ for a better comparison. The non-normalized resistance of the central bridge was 3.25 times higher than the other as expected considering the width reduction. There is a perfect overlap between the three curves showing that sample has not been damaged during the patterning process.

Electromigration runs were performed with cathode on the left side and the anode in the right side. Figure 4.7 (b) shows the normalized $R(T)$ curves obtained after a first EM run along with the one of the pristine state in black dots as a reference. We observe that the right bridge (close the anode) is not affected while in the left bridge the normal state resistance increased considerably and T_c decrease with a wide transition. The central bridge exhibits a higher normal state resistance, a second transition at T_c at $\sim 30K$ with dissipative state at low temperatures. The broadening of the T_c in the central and left bridges indicates a very in-homogeneous state, as it was already proposed in [160]. In all bridges a transition at 90 K is still visible, meaning that a part of the bridge was not affected by the EM. In the inset of figure 4.7 (b) we show an optical image taken at the end of the EM in

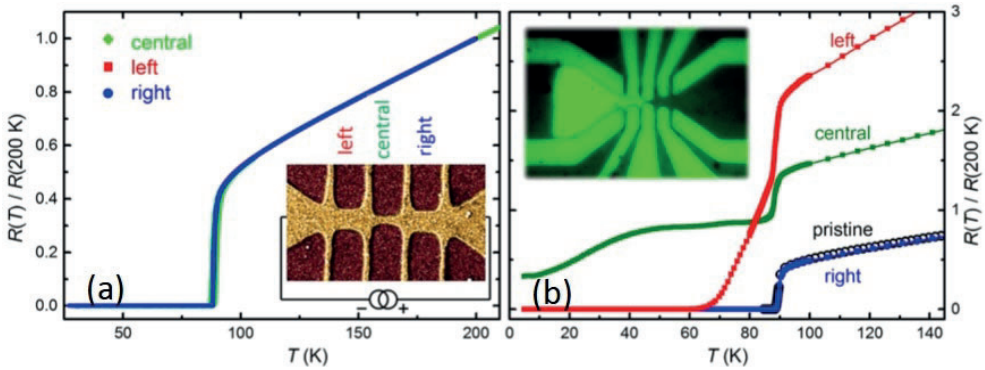


FIGURE 4.7: $R(T)/R(200\text{ K})$ for the central bridge (green), left bridge (red), and right bridge (blue) for the sample in the pristine state (a) and after electromigration (b). Inset in panel (b): optical microscopy image obtained after the electromigration process. The affected area on the cathode side is clearly visible as a bright region.

bright field and with the analyzer adjusted to optimize the contrast. The bright region indicates the affected part, starting at the central bridge and extending to the left. The optical properties of YBCO have been studied in references [117, 159, 161–163]. In the case of electric field parallel to the a -axis a decrease of reflectance with increasing oxygen content was reported, and an increase of the reflectance for the electric field parallel to the c -axis [159]. It was also reported that measurements of c -axis normal films show increased reflectivity in oxygen depleted regions [117]. According to all this, the cathode side and the central bridge are oxygen depleted zones (or rich in oxygen vacancies), in agreement with what we obtain through transport measurements.

At this point we aim to control the oxygen diffusion in our devices by performing subsequent EM runs, tuning the oxygen vacancies in the central and left bridges. In figure 4.8 (a) the evolution of T_c in the three bridges after several EM runs is displayed. Along with every T_c we also measured the carrier density n by performing Hall measurements at 105 K, using the four contacts close to the central bridge (contacts 2, 3, 6 and 7 in the inset in figure 4.8 (b)). The number of carriers in the union of the left and central bridges as a function of the electromigration run was plotted with red points and the carriers in the union of the central and right bridges is

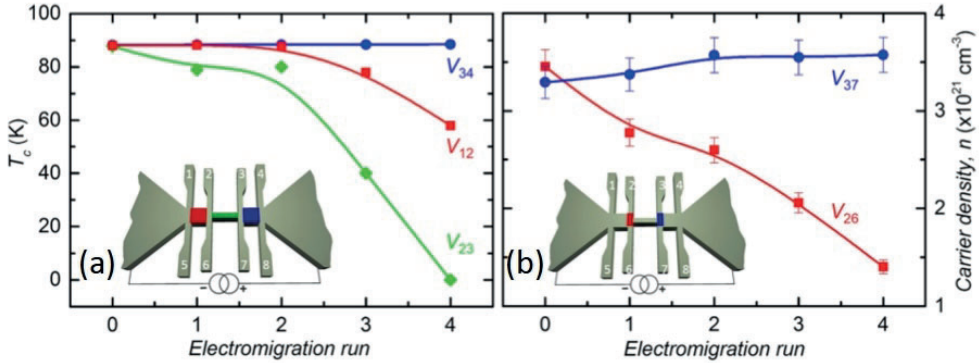


FIGURE 4.8: Evolution of the critical temperature T_c (a) and the carrier density, n (b), at different regions of the YBCO constriction. The color code of the data points corresponds to the signal picked up at the colored regions in the insets. Numbers indicate the voltage contacts addressed in each measurement.

plotted with blue points. The changes in both T_c and n are compatible with the scenario described before. With this polarity EM produces a diffusion of oxygen atoms towards the anode (right side) and a diffusion of oxygen vacancies towards the cathode (left side), meaning that the doping level increases in the cathode and decreases in the anode. Regarding the transport measurements T_c decreases and n is reduced in the cathode side. There is a slight increase in the carrier density of the anode side, due to maybe some oxygen atoms replenishing oxygen vacancies, and also a small decrease in the normal state resistance on the right bridge (anode side).

The information extracted from graphs 4.8 (a,b) can be used to determine the hole doping, this is, the number of holes per Cu atom in the CuO_2 planes. Hole doping p is a crucial parameter in cuprates, since it determines their T_c . This dependence along with the dependence of hole doping with the oxygen doping ($T_c(p)$ and $p(\delta)$) were calculated using several techniques in [164].

In figure 4.9 we plot the average T_c value of the left and central bridges as a function of the corresponding n value measured in the left Hall cross. We compare the obtained results with the data extracted from [164], finding a good agreement between them. It is important to note that results from [164] were obtained in single crystals and 300 K and our results on

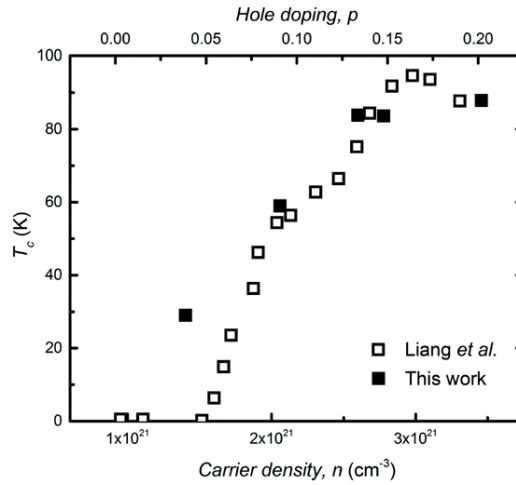


FIGURE 4.9: T_c as a function of the carrier density and hole doping estimated from our EM experiments (filled squares). For the sake of comparison, the data from [164] is included (empty squares).

YBCO films at 105 K. The fair agreement between the two independently determined experimental data points encourages us to propose the present method as an appealing approach to fine-tune the doping level in cuprates for eventually obtaining a detail mapping of the electronic phases in these materials.

4.3.3 Raman experiments

The displacement of oxygen atoms in our devices was further investigated using micro-Raman spectroscopy. With this technique it is possible to quantify the local oxygen content with micrometric resolution in different points of the device, after every EM run (see more details in section 2.5.2). The frequency of the O(4) vibration mode (directly related to the oxygen content x) is plotted in the pristine state and after two EM runs, in several points along the YBCO tracks (green points in figure 4.10).

In the pristine state (black dots) the phonon frequency value is 502 cm^{-1} , corresponding to an oxygen content $x = 6.95$ (optimally doped). The error bar is 2 cm^{-1} will only be plotted for these points. This value is constant along the whole track, supporting that our devices are homogeneous and

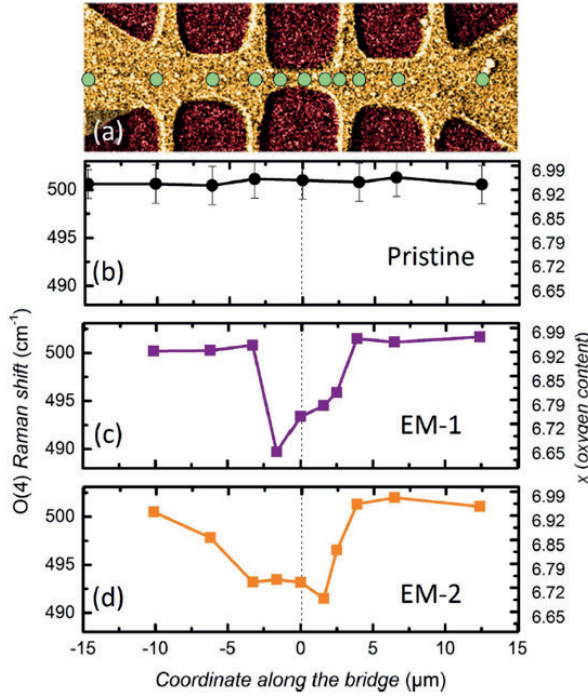


FIGURE 4.10: O(4) phonon mode frequency measured along the device (green points) for the pristine state and after two different EM runs (EM-1 and EM-2). The center of the constriction is marked with a dotted line.

well oxygenated in the pristine state. x can be determined from the phonon frequency with equation 2.5. After the first EM (EM-1) (purple squares) an important frequency shift appears, from 502 to 490 cm^{-1} , mainly in the central bridge and part of its left side. This shift corresponds to an oxygen depleted zone with $x \sim 6.65$ in the center towards the cathode. A small increase is found in the right side, meaning that oxygen content increased there (like in the Hall measurements). After the second EM (EM-2) the oxygen depleted zone is enlarged to the left side, supporting our previous optical observations and Hall measurements.

4.3.4 Anti-electromigration process

After performing several controlled electromigration runs, we tried to see if reversible oxygen motion could be obtained through an anti-electromigration (anti-EM) process by reversing the polarity of the bias current (figure 4.12 (a)). In this case the right bridge side corresponds to the cathode and the left bridge side to the anode. The evolution of the anti-EM run is shown in the optical microscope images in figure 4.11 (a-f), where we can see the progressive apparition of oxygen depleted zones (bright zones) extending to the cathode side. The time elapsed between consecutive images is close to 15 minutes. Again, as we observed in the anti-EM runs performed in previous sections, the oxygen depleted zones induced during electromigration runs cannot be healed with anti-EM. This effect is contrary to what we observed with field-induced oxygen migration (Chapter 3) probably because the electromigration process is much more drastic than the switching effect induced though voltage pulses thus producing non-reversible effects.

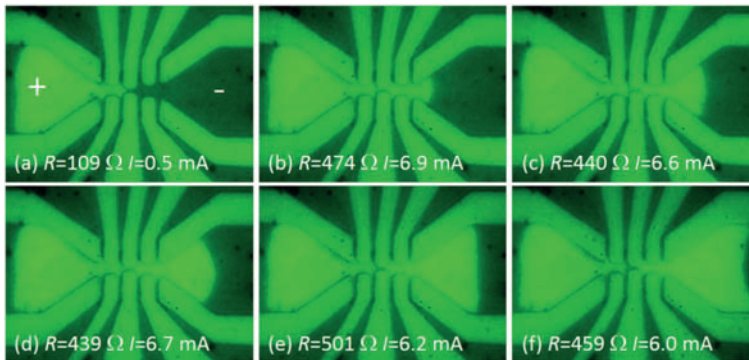


FIGURE 4.11: (a-f) Optical microscopy images of the oxygen-depleted zones (bright) during the anti-EM process. Labels (R, I) in panels a-f correspond to the coordinates along the R(I) curve shown in figure 4.12 (a).

Nevertheless, taking differential images by subtracting two consecutive images (figure 4.12 (b,c)) some dark points (rich in oxygen) can be detected meaning that a partial “healing” was attained during anti-EM run. The fact that this healing effect takes place in a restricted zone might indicate loss of oxygen from the sample. Bright zones appearing on the cathode indicate

oxygen depleted zones as detected in the optical images.

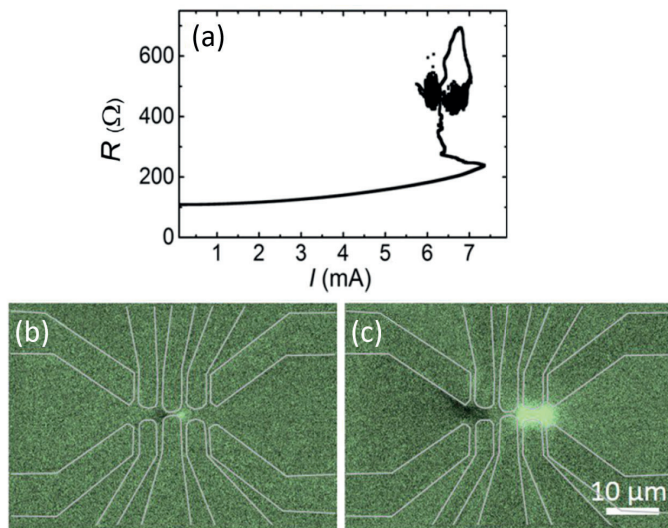


FIGURE 4.12: (a) $R(I)$ of the central bridge during the antielectromigration process. (b,c) Differential images illustrating the partial healing (black spots) due to anti-EM. The gray curve delineates the transport bridge.

4.4 Conclusions

In this chapter we studied the effect of current stimulated electromigration of oxygen atoms in micro-metric bridges patterned in YBCO thin films. We show that for YBCO, there is a temperature range where the superconducting critical current can exceed the extrapolated electromigration current. Within this regime, accessing the dissipative state can have detrimental consequences to the devices.

Progressive and well controlled electromigration runs have been used to finely tune the oxygen doping in specially pattern YBCO bridges. $R(T)$ curves measured before and after electromigration runs demonstrate that a metallic-insulating transition can be induced. Current reversal allows to perform anti-electromigration processes which produce a partial recovering of

the metallic state but without being able to achieve a reversible process.

We provide experimental evidence through Hall measurements, micro-Raman, and photoconductivity investigations that the electromigration process allows a selective displacement of oxygen atoms. The induced stoichiometry modulations become more stable (i.e., irreversible) as the excess current with respect to the onset of electromigration increases. The affected areas can be directly visualized by optical microscopy. This method represents a powerful alternative to locally fine-tune the charge carrier density in cuprates.

Chapter 5

YBCO films for neuromorphic applications

Neuromorphic computing, with processing elements trying to imitate the functioning of the brain, has shown superior performance over classical digital systems in processing cognitive functions with much low power consumption. In the last decades there has been a huge interest in exploring the possibility of designing novel devices capable of mimicking brain synapse and neuron functionalities. In this chapter we evaluated the use of the electric field-induced MIT modulation in YBCO, described in chapter 3, for the fabrication of neuromorphic devices which may emulate certain functions of a brain synapse. The resistive switching effect in YBCO can be powerful since it generates a homogeneous change of the resistance in an active volume, offering higher robustness and flexibility when compared to other RS devices that have been proposed as memristors to emulate synaptic functionalities [165].

We studied devices with two differentiated architectures. On one hand, we fabricated multi-terminal YBCO devices in top-top configuration to emulate the post-synaptic membrane and explore the possibility of tuning its synaptic weight or strength (the conductance or resistance of the channel)¹ with the action of several gate electrodes that act as pre-synaptic inputs. Electric pulses applied on gate electrodes will induce oxygen diffusion through the channel and thus modulate its resistance. The influence of different parameters like the geometrical disposition of the gates, the applied

¹The terms conductance (G) and resistance (R) are reciprocal, since $G=1/R$, so their variations are analogous. Both of them are commonly used in the bibliography of this field of research and so will be in this chapter.

voltage or the switching performance of each gate has been carefully investigated. Multi-terminal devices could offer the possibility of performing information transmission and learning processes at the same time, which cannot be performed with two-terminal memristors, and also the possibility of acquiring signals coming from different sources in a single channel.

On the other hand, we fabricated two-terminal YBCO top-bottom devices to analyze the possibility of inducing synaptic learning functionalities (potentiation and depression) in a simple device. Optimization of this simple device could be used to design more complex multi-terminal top-bottom structures, opening the path for the design of transistor-like devices with synaptic learning functionalities. Also, the behavior of the resistive switching in a top-bottom configuration may be different to the one obtained in a top-top configuration and needs to be examined. We have applied trains of pulses with different applied voltage and pulse duration, symmetric or asymmetric pulses, and evaluated their influence on the resistance modulation.

5.1 Device fabrication

In the experiments of this chapter, we have designed and fabricated two different kind of devices: devices with top-top configuration and devices in top-bottom configuration.

The devices in top-top configuration were patterned on YBCO films with thickness 100 nm grown by PLD. We fabricated transistor-like devices of 1000 μm in length and variable width from 5 to 100 μm . In some of the devices we sputtered large annealed Ag contacts of 200 nm in thickness to be used as external non-switchable electrodes thus inducing a switching just at the desired gate electrode. Gate contacts have smaller area (100x100 μm^2) and thickness 50 nm. A sketch of a multiterminal transistor-like device in top-top configuration can be seen in figure 5.1, along with an optical microscope image of several devices patterned with different widths.

In the case of the top-bottom YBCO devices a sample obtained from the lamination of a coated conductor was used (see 2.3.2), obtaining a YBCO epitaxial film on top of a silver over copper bottom electrode, supported on a silicon substrate. The patterning of the devices was similar to the one

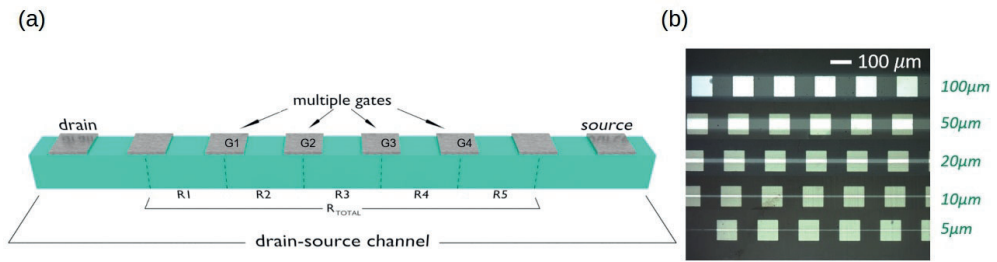


FIGURE 5.1: (a) Sketch of a YBCO multiterminal transistor-like device in top-top configuration. (b) Optical microscope image of devices patterned with widths from 5 to 100 μm .

used for the top-top configuration devices, but in this case only small silver contacts of $100 \times 100 \mu\text{m}^2$ were sputtered and none of them was annealed since to induce the resistive switching we used the bottom electrode. The patterned bridges were straight with a width slightly larger than the small deposited contacts, around $110 \mu\text{m}$. In this case, the width of the bridge had to be larger to the contact size in order to avoid a short-circuit between the top electrodes and the bottom electrode. A schematic representation of a resulting device is shown in figure 5.2.

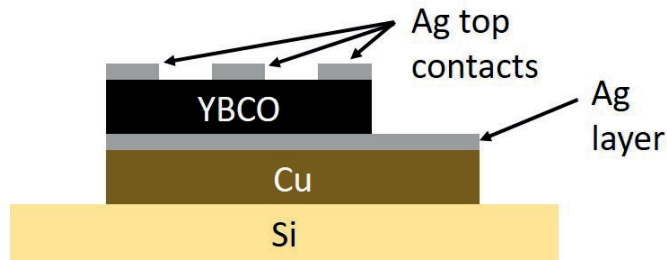


FIGURE 5.2: Sketch of a YBCO device with top Ag electrodes and a Ag over Cu bottom electrode, glued on top a Si substrate.

5.2 Multiple gate tuning of a drain-source channel conductance

In this section we studied the possibility of controlling the conductance of a source-drain-channel (which could mimic a post-synaptic membrane in a biological synapse) by using different gate electrodes (acting as pre-synaptic inputs) distributed along the channel. These experiments are similar to the ones discussed in LAT-gate devices in chapter 3 using top-top contacts, but in this case using more gates.

We use devices like the one shown in figure 5.1 where the evolution of the conductance in different segments of the channel (R_n , with $n = 1, 2, 3, 4$ or 5) is measured in a 4-point geometry using the source and drain electrodes to inject the current and the intermediate contacts to measure the voltage (and hence the resistance) in the volume between them. In this way we are measuring only the bulk resistance, avoiding the contribution of the contact resistances of the gates. The resistance of the different segments is modified by applying positive and negative voltage sweeps (of 100 pulses of 0.1 seconds) like the ones in chapter 3 in a two-point configuration between two gates in the channel, measuring the resistance and obtaining the corresponding R-V curve. We used a PPMS to do the 4-point measurements and an external source-measure unit for the two-point measurements (Keithley 2450), at room temperature. We demonstrated in chapter 3 that these voltage sweeps can generate an electric field-induced MIT driven by oxygen diffusion, with large reversible changes in the resistance of the material that are non-volatile (resistive switching). We also demonstrated that the effect is not confined in the contact regions, but it also reaches a certain volume below the contact and at a certain distance of the contacts.

The first test was performed in a multi-terminal device of width $10 \mu\text{m}$ with two central gates separated by a distance of $100 \mu\text{m}$ (figure 5.3 (a)). The R-V loops shown in figure 5.3 (b) were measured by using the two central active gates (in gold color) by applying a voltage of $\pm 12 \text{ V}$. Reversible and stable hysteresis loops were obtained showing a quite symmetrical complementary behaviour (for each polarity one contact switches to the LRS and the other the HRS). Taking into account that the channel should be homogeneous in its pristine state and that the eight gates were sputtered in the same way, the small asymmetry in the curves and the slightly different

values of the resistance in the HRS can be attributed to small differences in the contact resistance.

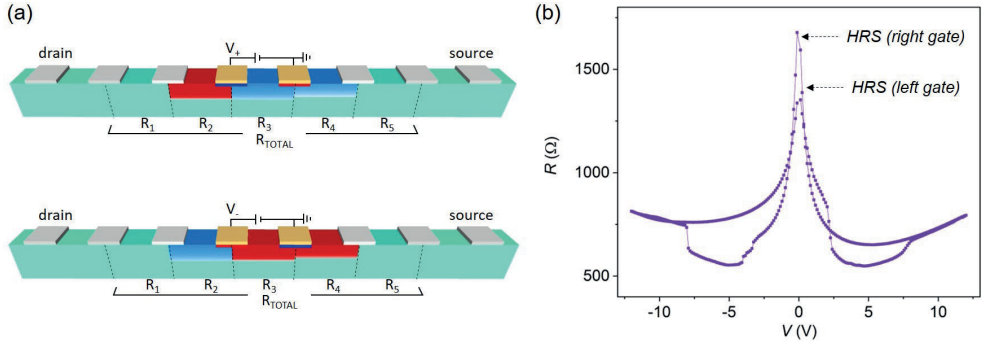


FIGURE 5.3: (a) Sketch illustrating the redistribution of oxygen and oxygen vacancies in a $10 \mu m$ wide and 100 nm thick YBCO device when applying positive (top) and negative (bottom) voltages between the central gates (in yellow), separated $100 \mu m$ from each other. Red and blue represent regions in HRS and LRS respectively, which thickness is in relation with the percentage of change of the resistance. (b) R-V curves obtained when applying voltage sweeps of $\pm 12 \text{ V}$ between the central gates (in yellow).

The gate at HRS is indicated for each polarity.

We evaluated how voltage sweeps through the gates modulate the conductance of the different segments of the channel. For that we plot the percentage of variation of the value of the resistance at different segments of the channel after applying different positive and negative voltage pulses (figure 5.4). The resistance variation has been calculated following equation 5.1, being $R_n(t)$ the resistance of the bulk of the segment n after certain voltage pulses and $R_n(i)$ the one measured at its initial state.

$$\Delta R_n = 100 \times [R_n(t) - R_n(i)] / R_n(i) \quad (5.1)$$

A clear and reproducible reversible variation of the resistance of different segments is observed. In segments 2, 3 and 4, the ones in direct contact with the two active gates variations of 15 to 35 % were measured while in segments 1 and 5, far from the switching gates the resistance is almost constant. The variation of resistance of the whole channel, including the 5 segments, is almost constant (ΔR_{TOTAL} in figure 5.4). This is compatible with the scenario of a field-induced redistribution of oxygen vacancies in

the channel with no exchange with the exterior. The initial value of the resistance of all the regions of the channel is $R_i \sim 150\text{-}200 \Omega$.

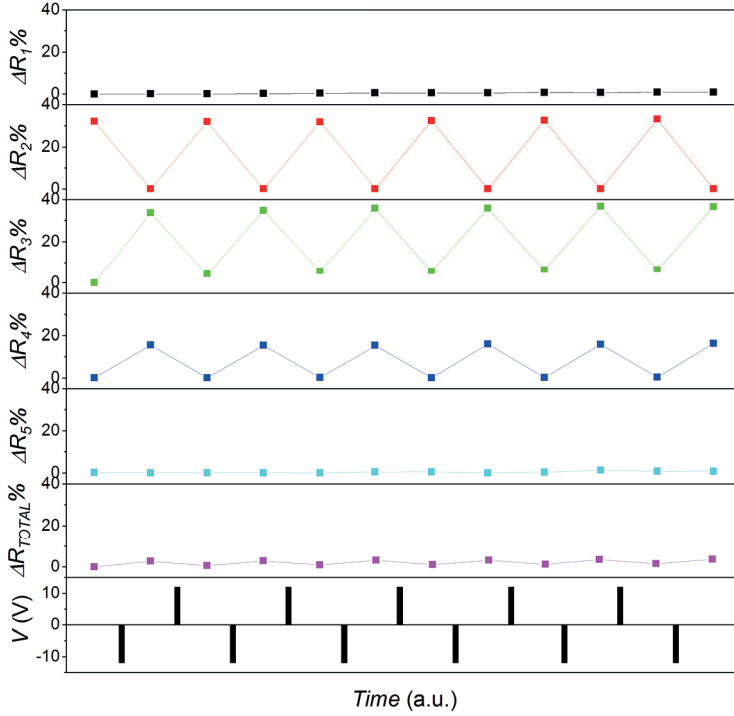


FIGURE 5.4: Percentage of variation of the resistance measured with a 4-point configuration at the five segments of the channel R_i and the whole channel R_{TOTAL} after each voltage sweep.

The observed variations can be explained assuming that the resistance of a certain region of the bridge is directly related to its oxygen content, as already demonstrated in previous chapters and can also be found in literature [100, 166]. The most significant effect of the electric field generated when applying the voltage between the gates is the induction of oxygen diffusion, and as a result a drift of oxygen vacancies from the gate positively charged to the gate negatively charged. When a positive voltage is applied, oxygen vacancies are accumulated in a region confined below the right gate, that switches to the HRS (red color in a segment just below the gate in figure 5.3 (b)). At the same time, in a region confined below the left gate oxygen vacancies are occupied by oxygen ions and switches to the LRS (blue color in a segment just below the gate). We observe a complementary effect when

applying a negative voltage, the right gate switches to the LRS and the left one to the HRS. But this effect also influences the concentration of oxygen (and oxygen vacancies) in the bulk of the channel. The amount of switched volume depicted in the different regions of the channel in figure 5.3 can be related to its resistance variation if we assume that the resistance of a region in the HRS is much higher than the resistance of the region in the LRS. According to the variations of the resistance of the different segments of the channel and the switch of the active gates we can conclude that when a gate switches to the LRS certain surrounding region loses oxygen (or has more oxygen vacancies), and when a gate switches to the HRS certain surrounding region gains oxygen. The fact that the resistive switching of the gates has an effect in the resistance (and hence the oxygen content) in volumes away from them enforces the expected large oxygen mobility in our devices along the a and b axes.

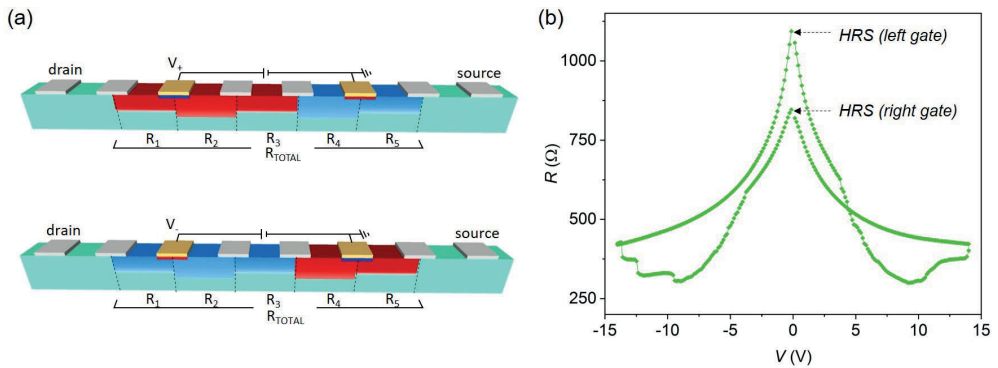


FIGURE 5.5: (a) Sketch illustrating the redistribution of oxygen and oxygen vacancies in a $100 \mu\text{m}$ wide and 100nm thick YBCO device when applying positive (top) and negative (bottom) voltages between two gates (in yellow), separated $500 \mu\text{m}$ from each other. Red and blue represent regions in HRS and LRS respectively, which thickness is in relation with the percentage of change of the resistance. (b) R-V curves obtained when applying voltage sweeps of $\pm 14 \text{V}$ between the central gates (in yellow).

The gate at HRS is indicated for each polarity.

In the second experiment we performed the same analysis but this time in a $100 \mu\text{m}$ wide channel and applying the voltage between two gates at a distance of $500 \mu\text{m}$ (indicated in gold color in figure 5.5 (a)). R-V loops obtained are shown in figure 5.5 (b) where notable asymmetry can be seen,

with a big difference in the resistance value at the HRS of both gates.

This particular situation has an important effect in the resistance variation of the different segments of the channel, which is highly inhomogeneous. In figure 5.6 we see changes of up to 200% in segment 4, close to the right gate while a complementary effect can be observed in the region of the channel formed by segments 1, 2 and 3. Again the resistance of the whole channel remains almost constant and the gate that switches to a higher value of the resistance in its insulating state generates the diffusion of oxygen vacancies to further distances. The initial value of the resistance of all the regions of the channel is $R_i \sim 150\text{-}200 \Omega$.

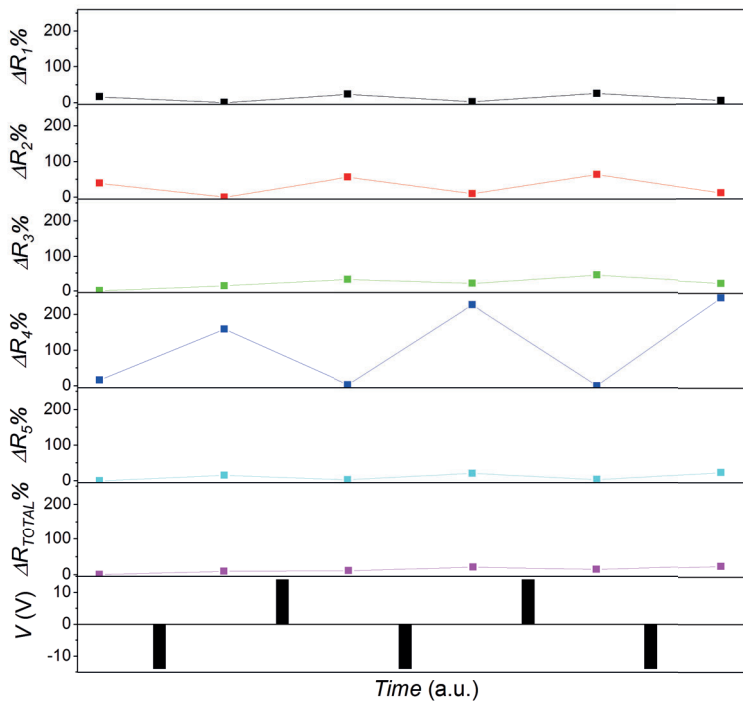


FIGURE 5.6: Percentage of variation of the resistance measured with a 4-point configuration at the five segments of the channel R_i and the whole channel R_{TOTAL} after each voltage sweep.

Finally a third experiment was performed to explore the variation of the channel resistance when inducing the switching in just one of the gates. The experiment was performed on a channel of width $30 \mu\text{m}$ using two gates separated a distance of $500 \mu\text{m}$. In this case however we just switch

one of the gates by applying asymmetric voltage pulses, as described in chapter 3. Figure 5.7 (b) shows the obtained $R(V)$ loops where one can observe that only the left gate is switched by applying a negative voltage larger than the one needed to switch the left gate but a positive voltage lower than the one needed to switch the right gate to the HRS.

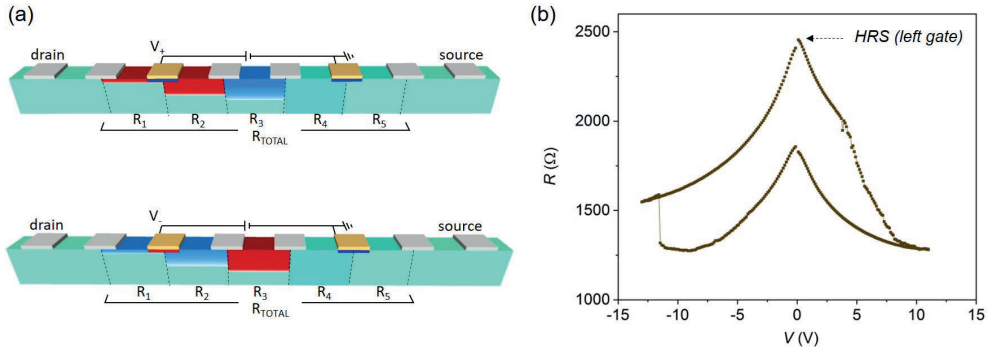


FIGURE 5.7: (a) Sketch illustrating the redistribution of oxygen and oxygen vacancies in a $30 \mu\text{m}$ wide and 100 nm thick YBCO device when applying positive (top) and negative (bottom) voltages between the central gates (in yellow), separated $500 \mu\text{m}$ from each other. Red and blue represent regions in HRS and LRS respectively, which thickness is in relation with the percentage of change of the resistance. (b) R - V curves obtained when applying voltage sweeps of $+12$ and -14 V between the two gates (in yellow). The applied positive voltage is lower than V_{reset} so that the right contact stays at the LRS and only the left gate switches between LRS and HRS.

Figure 5.8 shows that in segments 4 and 5, the ones close to the non-switched contact the resistance does not change, remaining in their initial LRS, while segments 1 and 2 have the opposite behavior to that obtained in segment 3. When switching the left gate to the HRS oxygen vacancies flow from segment 1 and 2 to segment 3. The initial value of the resistance of all the regions of the channel is $R_i \sim 400\text{-}500 \Omega$. It is important to note that in this case there is a non negligible variation of the resistance of the whole channel (segments 1, 2, 3, 4 and 5). This variation of R_{total} , which is reversible in contrast with the insignificant variations in the two previous experiments can be due to resistance variations induced close to the drain

contact which have not been included in the measurements.

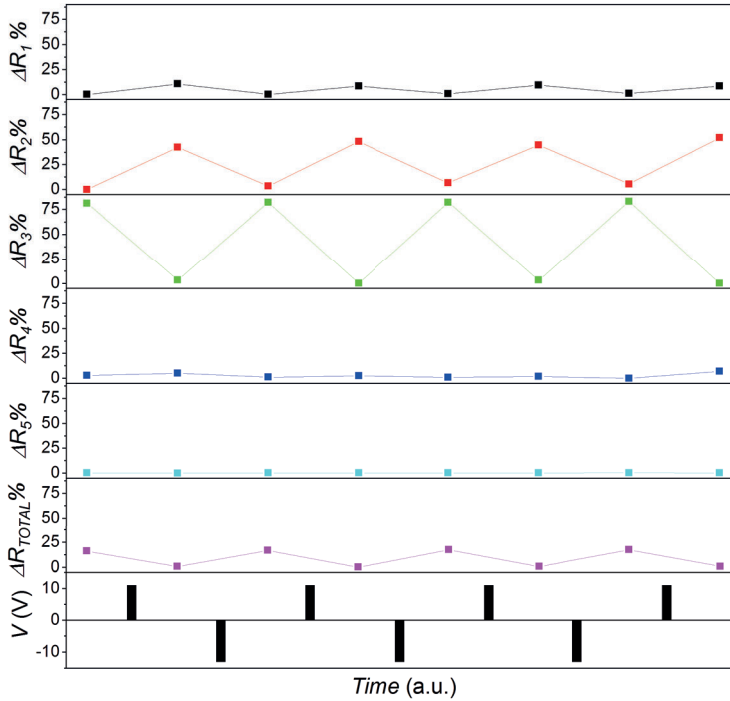


FIGURE 5.8: Percentage of variation of the resistance measured with a 4-point configuration at the five segments of the channel R_i and the whole channel R_{TOTAL} after each voltage sweep.

As a conclusion, we demonstrated the possibility of modulating the conductance of a drain-source YBCO channel by inducing resistive switching in different gates thus generating oxygen diffusion not only in the vicinity of the gates but also in a significant volume of the channel. The effect can be tuned by gate selection, switching performance of the gate, applied voltage and device geometry. These devices can be interesting for neuromorphic applications to emulate the behavior of a brain synapse, with the source-drain channel acting as the post-synaptic membrane, which weight is controlled through multi terminal gates (pre-synaptic inputs).

5.3 Potentiation and depression effects in top-bottom devices

In this section we will study the possibility to modulate the conductance of a device by applying voltage pulses using a top-bottom configuration. We aim to generate a controllable variation of the resistance through oxygen modulation using a configuration that may be better integrated in transistor-like devices. We will explore the symmetry and linearity of the resistance changes obtained in a two-point configuration by applying voltage trains with different number of pulses, amplitude and duration.

Before starting with each voltage pulse experiment, we perform a previous characterization of the resistive switching characteristics of the device by measuring controlled $R(V)$ loops. To do so, we apply continuous voltage sweeps between top and bottom electrodes progressively increasing the amplitude.

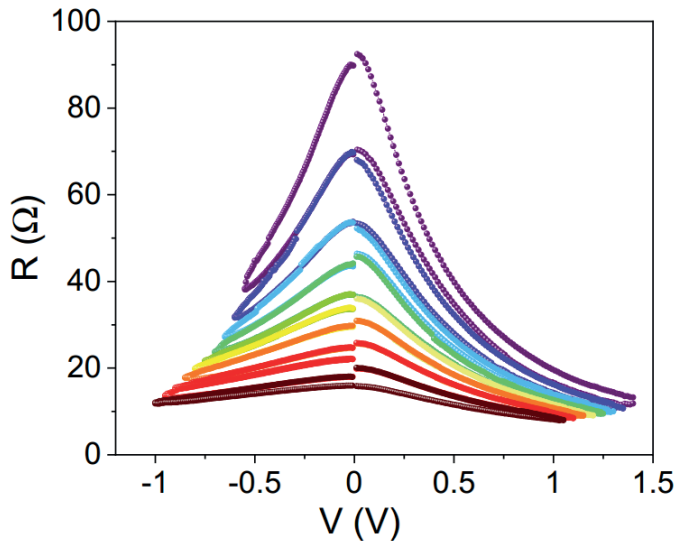


FIGURE 5.9: Example of the $R(V)$ loops measured in a top-bottom device with a progressive increase of the applied voltage in the positive polarity and a progressive decrease of the applied voltage in the negative polarity.

In figure 5.9 we can see an example of the $R(V)$ loops measured in a top-bottom device, progressively increasing/decreasing the positive/negative

voltage applied between the top Ag electrode and the bottom Cu electrode. We observe that many different intermediate non-volatile resistance values may be reversibly obtained with gradual and smooth transitions. This is a key advantage of volumic resistive switching which produce a robust and reproducible effect, as compared to devices showing filamentary switching since its stochastic nature produce abrupt set and reset processes. In our case, having a homogenous change of the bulk resistance, stochastic effects can be eliminated, making them particularly appealing for memory and neuromorphic applications [134].

One the switching performance of our systems is evaluated, we proceed to analyze the effect of voltage pulses on the device resistance. Figure 5.10 schematically shows the procedure followed in all the measurements. Different number of pulses of a given maximum voltage (V_{write}) are used to change the system resistance. After each pulse a small voltage (V_{read}) is used to read the achieved state without modifying it. The duration of every pulse is determined as (t_{on}) which is kept constant and equal to the time between pulses (t_{off}).

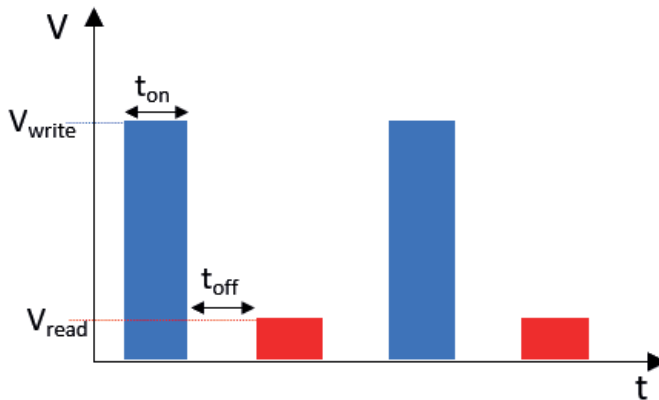


FIGURE 5.10: Sketch of a small part of a train of pulses.

5.3.1 Effect of the applied voltage

First of all we analyzed effect of the maximum voltage applied by performing ten trains of 20 pulses, alternating the polarity, at $V_{write} = \pm 0.8V, \pm 1.0V$

and $\pm 1.2V$. These values of voltages have been taken close to the value that produced large resistance variation in the R(V) loops. For all the measurements, the duration of every pulse (t_{on}) and the distance between pulses (t_{off}) was kept constant with a value of 0.1 s.

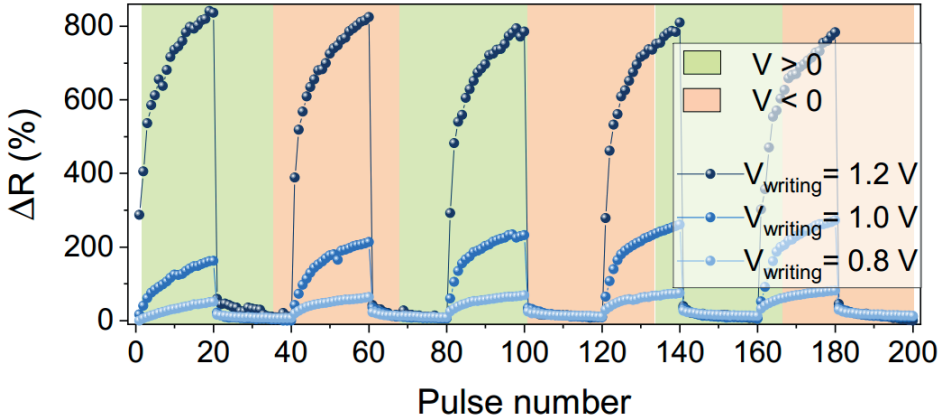


FIGURE 5.11: Graph with resistance variations measured after applying trains of voltages ± 0.8 V, ± 1.0 V and ± 1.2 V in a top-bottom device.

Figure 5.11 shows the variation of the resistance ($\Delta R(\%)$) measured with the reading voltage (V_{read}). Green regions correspond to pulses of positive voltage while pink regions correspond to pulses of negative voltage. Clear potentiation/depression effects are observed with an enhancement/decreasing of the resistance with the number of positive/negative pulses. We also observe that the measurements are reversible for all the voltages and, as expected, large variations are obtained by applying larger voltages. The change of the measured resistance may be associated to the creation of oxygen vacancies which increases with the applied voltage. As we described in chapter 1, efficient and accurate training of synaptic weight needs not only reversible conductance potentiation or depression with the number of pulses but also a high degree of conductance linearity. From the curves obtained in Figure 5.11 we see that as we reduce the applied voltage the potentiation/ depression curves tend to be more linear although small resistance variations are obtained. Further experiments by applying different amount of pulses and/or changing the values t_{on} and t_{off} should be performed in order to improve the linearity of the curves keeping large resistance changes.

5.3.2 Effect of the duration of the pulses

We performed an experiment similar to the previous one, but in this case, we analyzed the influence of the duration of the voltage pulses (t_{on}) and the time between two consecutive pulses (t_{off}). In each measurement both times are equal due to equipment limitations, but we expect the effect of the t_{off} to be less important than the effect of the t_{on} . We chose to apply pulses of $\pm 1.2V$ so as to get bigger changes. Three different values for the duration of the pulse (t_{on} and t_{off}) were used: 0.001 s, 0.01 s and 0.1 s. They were applied in this order as a precaution since the lower the time the lower effect is expected in the material.

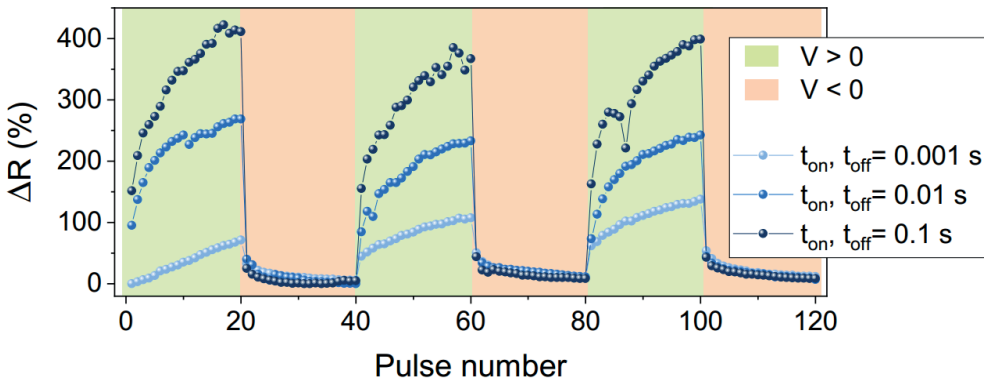


FIGURE 5.12: Graph with resistance variations measured after applying trains of $\pm 1.2 V$ and $t_{on} = t_{off}$ 0.001 s, 0.01 s and 0.1 s in a top-bottom device.

Graph 5.12 shows that the obtained results are similar to the previous study with different voltages. Reversible changes are obtained again with a progressive increase of the resistance with the number of pulses for positive polarity (green regions), tending to a saturation value that we did not reach in any case. The resistance changes are less progressive for the negative polarity (pink zones) where we observe that a very fast decay is obtained after the first applied pulse, specially for the ones with larger duration. With $t_{on}=t_{off}=0.001$ s the change in resistance is small and quite linear at the first trend of pulses, although it is not completely reproducible. For $t_{on}=t_{off}=0.01$ s and 0.1 s the changes in resistance are considerable higher as expected, but with a less linear behavior. The longer the duration

of the pulse, the more oxygen vacancies can be mobilized. Again, we have the same behavior that fulfils the desired potentiation and depression processes expected for synaptic devices though it may be optimized to achieve a better linearity specially for the depression curves.

5.3.3 Effect of asymmetric voltages

With the aim to obtain a much progressive decrease of the resistance also with negative voltages we tried to apply trains of pulses with different positive and negative voltage, in particular we used +1.2 V and -1.0 V, with three different values for the duration of the pulse (t_{on} and t_{off}), 0.001 s, 0.01 s and 0.1 s.

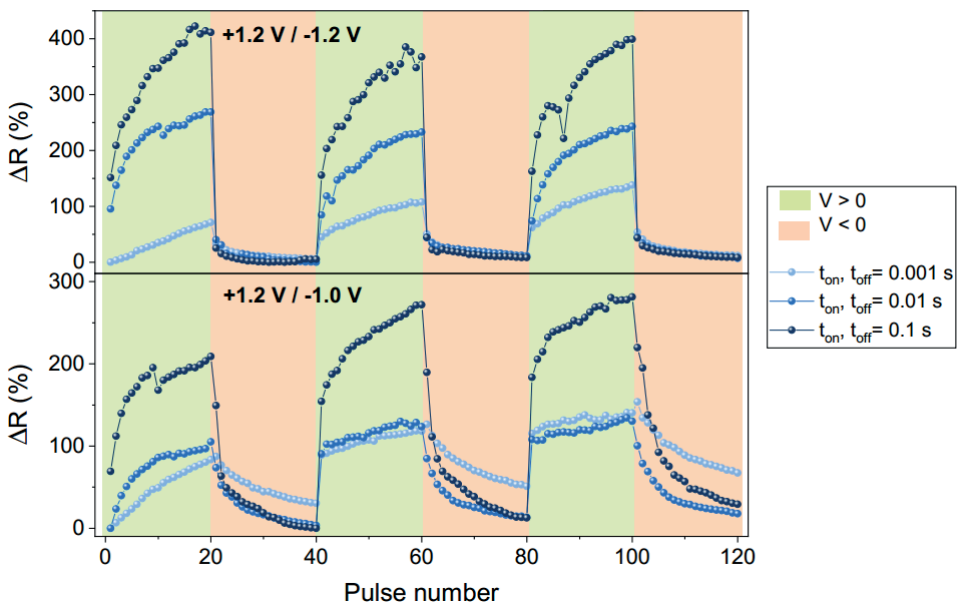


FIGURE 5.13: Graph with the measured resistance variations measured after applying trains of pulses of +1.2/-1.2 V (above) and +1.2/-1.0 V (below) and t_{on} 0.001 s, 0.01 s and 0.1 s in a top-bottom device.

In graph 5.13 we plotted at the top panel the changes of the resistance ($\Delta R(\%)$) measured in the previous experiment, when applying trains of pulses with amplitude 1.2 V for both positive and negative polarities. In

the bottom panel we plotted the changes of resistance measured when applying asymmetric pulses with +1.2 V and -1.0 V. We can see that the decrease of the resistance for the latter case is much more progressive than by applying symmetric voltage pulses for both polarities. It is important to mention that in this case the curves are less reproducible since the lower resistance is not completely recovered after applying the trend of negative voltage pulses.

As a conclusion, we demonstrated that we can emulate synapse potentiation and depression processes in YBCO top-bottom devices. We observed that by tuning the voltage pulses as well as the duration of the pulse we can obtain a stable, reproducible and controllable effect. With these experiments we demonstrate that the linearity and symmetry of the resistance variation may be modulated with different parameters thus offering the possibility to optimize the device performance. This along with the possibility of achieving multiple resistance states by proper selection of the input signal, with long retention times, make them promising candidates for synaptic devices.

5.4 Potentiation and depression effects in top-top devices

After demonstrating the possible resistance modulation with voltage pulses applied in top-bottom devices using a two-contact configuration, we aim to go a step further and try to study the possibility to modulate the resistance of a drain-source channel by using a top gate electrode (G). In this case we may decouple reading and writing processes and thus introducing extra flexibility in the device. We used a 100 μm wide, 500 μm long and 100 nm thick device with three top silver contacts, identical to the ones in the multiterminal devices of the previous experiments (see figure 5.14). An "external" annealed contact of thickness 200 nm and area 700 x 250 μm^2 , which does not switch at the working voltages, is used to apply the voltage pulses in contact G. The other two contacts (D and S) are used to measure the changes of the resistance in the drain-source channel induced by the pulses, using a 2-point configuration and applying a small reading voltage $V_{\text{reading}} = 0.1\text{V}$.

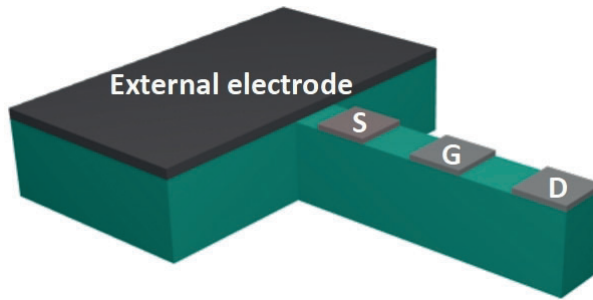


FIGURE 5.14: Sketch of a transistor-like device with three not-annealed contacts in the drain-source channel (D-S) and an annealed external electrode to induce the switching in the central gate electrode (G).

The application of the pulses in this case is more complex since we have to apply reading and writing pulses through different contacts. The protocol used is depicted in figure 5.15. We apply different writing pulse trains at the gate electrode, starting with one pulse and successively increasing the number of pulses in units of 2 since we reach a total number of 19. After each train of G pulses a reading pulse of 0.1 V is applied at D-S. As in the previous section we depict with green the area with positive pulses and pink the area with negative pulses. The voltage used in the writing trend of pulses was +7 V and -6 V and the duration of both writing and reading pulses was $t_{on} = t_{off} = 0.1$ s.

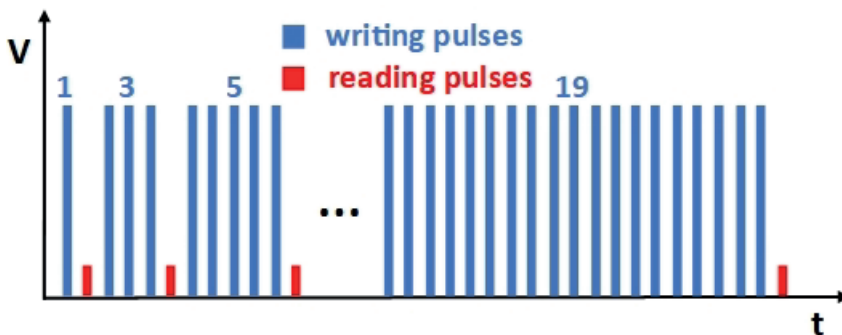


FIGURE 5.15: Scheme of the measurement protocol in the potentiation and depression experiments in top-top devices. The number of writing pulses (blue columns) is $N=2n+1$, with $n=0,1,2,\dots,9$. The reading pulse after each train is indicated in red.

Figure 5.16 shows the variation of the D-S channel conductance as a function of the number of trains. We observe that we are able to modify it by applying gate voltage pulses and thus it is possible to decouple writing and reading processes. Potentiation and depression curves are obtained emulating the synaptic weight. In this case it is important to note that the resistance response is almost linear with the train number which is ideal for the design of learning rules in synaptic devices. However, further studies need to be performed in order to improve the reversibility of resistance changes and eventually increase the D-S conductance variation which in this case is quite small (2%).

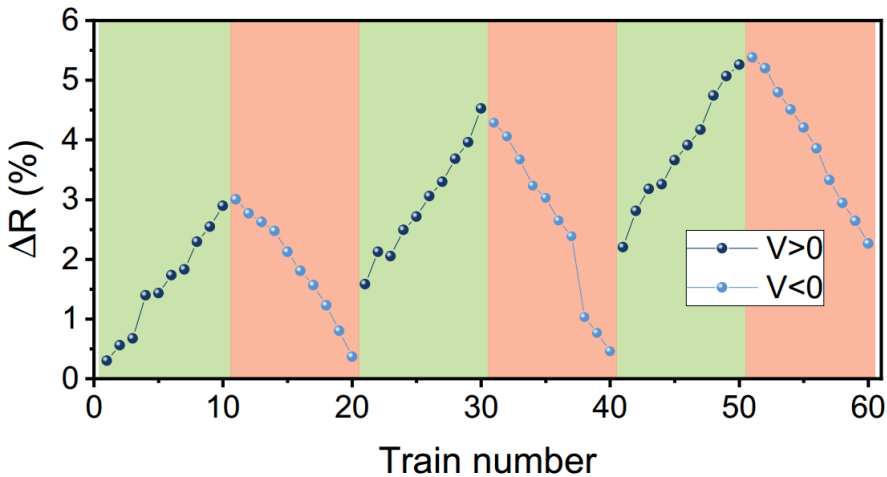


FIGURE 5.16: Graph with the measured change of the resistance of the drain-source channel after applying trains of pulses of $+7.0/-6$ V and t_{on} 0.1 s in a top-top transistor-like device.

5.5 Conclusions

As a conclusion for this chapter, we demonstrated that YBCO can be a good candidate for the fabrication of neuromorphic devices, in particular emulating synapses, taking advantage of the possibility of inducing reversible MIT through electric field-induced oxygen diffusion, in a reversible, non-volatile and controlled way, using two different architectures.

With specially designed top-top devices we emulated part of the behavior of a brain synapse, with a source-drain channel as the post-synaptic membrane which could be modulated by multiple metallic gates that act as pre-synaptic inputs. By proper control of the voltage applied, gate performance and device geometry we can analogically tune the bulk resistance or conductance of different parts of the channel, which would be equivalent to the synaptic weight, in a non-volatile and reversible way. The use of multi-terminal devices with several gates would allow to obtain signals from different sources simultaneously which can experience spatiotemporal effects not available using two terminal devices.

With simple top-bottom devices we demonstrated learning capabilities emulating the potentiation and depression of the synaptic weight through voltage pulses. Tuning of the analogic resistance change could be obtained with external control parameters such as applied voltage, duration of the pulse, and the number of pulses, being possible to achieve different reversible synaptic weights (resistance values) with long retention times. Linearity and symmetry of potentiating and depression curves can be optimized by proper design of the device with a good control of the local oxygen diffusion. Potentiation and depression effects could be also induced in three terminal top-top devices where the resistance of a drain-source channel was modulated by using a central gate. This kind of devices may be used to design neuromorphic systems with decoupled reading and writing processes.

As a future work, it would be interesting to analyze the effect of time spaced voltage pulses from different neurons with the aim of emulating the STDP characteristics of a synapse. Volatile resistance changes could be also investigated, with the aim of emulating the behavior of a neuron and thus offering the possibility to design a full neuromorphic system based on YBCO that can implement the functions of both neurons and synapses. The aim of this thesis is studying the field-induced reversible tuning of oxygen doping in YBCO.

General conclusions

The aim of this Thesis is the study of current and electric-field induced reversible oxygen diffusion in superconducting YBCO films. Local modulation of the metallic (superconducting)-insulator transition and resistive switching effects were explored by designing and fabricating devices with different geometries and configurations. We used several characterization techniques and numerical simulations to elucidate the mechanisms that control volume gate-tunable oxygen doping in our systems and studied the possibility of exploiting this phenomenon for emerging technological applications.

In chapter 3 we investigated the tuning of Metal-Insulator Transition (MIT) and non-volatile resistive switching in YBCO fields by means of electric-field induced oxygen diffusion. We have shown that both normal state resistance and the superconducting critical temperature can be reversibly manipulated in confined active volumes of the film by gate-tunable oxygen doping. Vertical and lateral oxygen mobility may be finely modulated, at the micro- and nano-scale, by tuning the applied bias voltage and operating temperature thus providing the basis for the design of homogeneous and flexible transistor-like devices with loss-less superconducting drain-source channels. We analyze the experimental results in light of a theoretical model, which incorporates thermally activated and electrically driven volume oxygen diffusion. The MIT induced in our systems is not just confined at the vicinity of the interface between the superconductor and the gate but allows a nonvolatile homogeneous bulk modulation of the carrier density, appearing as a very appealing mechanism for the design of robust and homogeneous devices. Completely reversible phase transitions may be tuned by directly using a metallic gate, without the need of an electrostatic or ferroelectric layer, thus simplifying very much the device design. The demonstrated switching properties can be exploited for the fabrication of novel energy-efficient memories and transistor-like superconducting functional devices.

In chapter 4 we focused on the investigation of oxygen doping in YBCO bridges through current-stimulated oxygen migration. Specially designed patterned multi-terminal transport bridges allowed us to electrically assess the directional oxygen atom diffusion and generation of oxygen vacancies. The effect of electromigration in the physical properties of the material was explored by using electric transport measurements, optical microscopy, photo-conductivity experiments and Raman spectroscopy. We observed an in-homogeneous oxygen vacancy distribution with a controllable propagation speed in extended regions of the devices. The irreversibility of the process is linked to the excess current applied with respect to the value at which electromigration starts. Contrary to what we obtained in voltage gate tunable devices, only partial recovering of the metallic state was achieved with electromigration doping. The studied electromigration effects complement the investigations of reversible field-induced oxygen doping in YBCO films and provide a powerful method to locally tune the charge carrier density in cuprates for a systematic study of their complex phase diagram.

In chapter 5 we have explored the potential of reversible MIT in YBCO for the design of robust and flexible multi-terminal memristive transistor-like devices for neuromorphic applications. We have studied different structures patterned on YBCO films using top-top and top-bottom gate configurations, which are able to display gate modulable non-volatile analogic resistance changes. We have analyzed several device configurations in which the lateral conduction between a drain-source channel (synaptic weight) may be effectively controlled by several metallic gates, acting as pre-synaptic inputs. The effect of applied voltage, number and duration of the pulses, on potentiation and depression curves has been analyzed. The key advantage of these materials is the volume resistive switching effects induced which allows to design flexible transistor like-devices with decoupled writing and reading events, and significant reduction of cycle-to-cycle and device-to-device variations.

Future work

Along all the work carried out in this thesis several new ideas to be further investigated appeared, as well as the possible variations in the experiments here depicted to fully understand the studied phenomena and open the path for new possible applications.

Regarding the resistive switching characteristics explored in chapter 3, the lateral dimensions of our devices in top-top configuration were on the order of hundreds of microns. We expect that fabricating devices some orders magnitude smaller, the switching speed would be hugely reduced, which is very interesting for memory or logic applications. Moreover, the resistive switching characteristics of the devices in top-bottom configuration used in chapter 5 need to be better explored by using non-conductive patterned buffer layers to be able to design transistor-like devices with improved switching performances.

The superconductor-insulator transition described in chapter 3 appears as a very appealing mechanisms to design electrically addressable functional superconducting devices. A much deeper study of this effect may be performed in order to better understand reversible gate tunable oxygen diffusion directly induced at the superconducting state. It is also very interesting to extend the present work to other strongly correlated oxides.

In chapter 4 we studied the reversibility of the electromigration process by inverting the applied current. We succeeded only in some cases and not with a complete “healing of the devices”. A further study on this point would be very interesting for the practical applicability of electromigration processes.

Chapter 5 introduces several functionalities which may be exploited to emulate synaptic learning using transistor-like multi-terminal devices.

Further studies need to be performed in order to use the flexibility of the material to approach the desired values of conductance change, multi-level states, symmetry/linearity of weight update and retention/endurance properties. Moreover, It would be very interesting to study the Spike-timing-dependent plasticity characteristics of our synaptic devices, using time spaced voltage pulses as inputs from different neurons and the possibility to induce volatile resistance changes to emulate a neuron behavior.

During this Thesis we have started to study the field-induced oxygen doping effect, and associated carrier density modulation in YBCO films, by means of in-situ X-ray absorption spectroscopy at the ALBA synchrotron, in collaboration with Dr. Carlo Marini and Dr. Laura Simonelli. Promising results, evidencing a clear modification of the Cu coordination after voltage pulses were obtained which can be correlated with a de-oxygenation of the CuO chains. Further analysis of the obtained results may be performed in order to achieve a better understanding of the electrochemical oxygen doping effect and associated mechanisms.

List of abbreviations

AFM: Atomic Force Microscopy

ALD: Atomic Layer Deposition

B: Magnetic field

BC-MIT: Bandwidth Controlled Metal-Insulator Transition

BNC: Bayonet Neill-Concelman connector

BSCCO: Bismuth strontium calcium cuprate ($Bi_2Sr_2Ca_{n-1}Cu_nO_{2n+4+x}$)

CC: Coated Conductor

CCD: Charge-Coupled Device

CMOS: Complementary Metal-Oxide-Semiconductor

CSD: Chemical Solution Deposition

DC: Direct Current

DRAM: Dynamic Random-Access Memory

D-S: Drain-Source

E: Electric field

ECM: Electrochemical Metallization Mechanism

E_f : Fermi energy

EM: Electromigration

FC: Field Cooled

FC-MIT: Filling Controlled Metal-Insulator Transition

FeRAM: Ferroelectric Random-Access Memory

F_e : Electrostatic Force

F_L : Lorentz Force

F_m : Magnetic Force

FWHM: Full Width at Half Maximum

HRS: High Resistance State

HTS: High Temperature Superconductor

I: Electric current

I-V: Current vs Voltage

J: Current density

J_c : Critical current density

J_{em} : Electromigration current density

- LAO:** Lanthanum Aluminate $LaAlO_3$
- LabVIEW:** Laboratory Virtual Instrument Engineering Workbench
- LCCO:** Lanthanum Cerium Cuprate ($La_{2-x}Ce_xCuO_4$)
- LHB:** Lower Hubbard Band
- LIF:** Leaky Integrate and Fire
- LMO:** Lanthanum Manganite ($LaMnO_3$)
- LRS:** Low Resistance State
- LSCO:** Lanthanum Strontium Cuprate ($La_{2-x}Sr_xCuO_4$)
- LSMO:** Lanthanum Strontium Manganite ($La_{1-x}Sr_xMnO_3$)
- LTD:** Long-Term Depression
- LTP:** Long-Term Potentiation
- MBE:** Molecular-Beam Epitaxy
- MIT:** Metal-Insulator Transition
- MRAM:** Magnetoresistive Random-Access Memory
- NNO:** Neodymium nickelate ($NdNiO_2$)
- NPLC:** Number of Power Line Cycles
- PCRAM:** Phase-Change Random-Access Memory
- PLD:** Pulsed Laser Deposition
- p(O₂):** Oxygen partial pressure
- PPMS:** Physical Property Measurement System
- R:** Resistance
- R_H:** Resistance of the HRS
- R_L:** Resistance of the LRS
- RAM:** Random Access Memory
- ReRAM:** Resistive Random Access Memory
- RS:** Resistive Switching
- RT:** Room Temperature
- R-V:** Resistance vs Voltage
- R_{vol}:** Volume resistance
- SEM:** Scanning Electron Microscopy
- SIT:** Superconductor-Insulator Transition
- SMU:** Source Measure Unit
- SQUID:** Superconducting QUantum Interference Devices)
- STDP:** Spike-Timing-Dependent Plasticity
- STO:** Strontium titanate $SrTiO_3$
- T:** Temperature
- T_c:** Critical Temperature or Curie Temperature
- TF:** Goldsmith Tolerance Factor

TFA: Trifluoroacetic Acid

TMO: Transition Metal Oxide

U: Coulomb Repulsion U

UHB: Upper Hubbard Band

UV: UltraViolet

UHV: Ultra High Vacuum

V: Voltage

***v*:** Velocity

VCM: Valence Change Mechanism

V_H :

V_H : Hall voltage

V_{O-} : Oxygen vacancies

W: Bandwidth

XRD: X-Ray Diffraction

XRR: X-Ray Reflectivity

YBCO: Yttrium Barium Copper Oxide ($YBa_2Cu_3O_{7-\delta}$)

ZFC: Zero Field Cooled

List of publications

Anna Palau, Alejandro Fernandez-Rodriguez, Juan Carlos Gonzalez-Rosillo, Xavier Granados, Marion Coll, Bernat Bozzo, Rafael Ortega-Hernandez, Jordi Suñé, Narcis Mestres, Xavier Obradors y Teresa Puig. "Electrochemical Tuning of Metal Insulator Transition and Nonvolatile Resistive Switching in Superconducting Films." In: *ACS Applied Materials & Interfaces* 10, 36, 30522–30531 (2018). DOI: [10.1021/acsami.8b08042](https://doi.org/10.1021/acsami.8b08042).

X. D. A. Baumans, A. Fernández-Rodríguez, N. Mestres, S. Collienne, J. Van de Vondel, A. Palau y A. V. Silhanek. "Electromigration in the dissipative state of high-temperature superconducting bridges." In: *Applied Physics Letters* 114, 012601 (2019). DOI: [10.1063/1.5063797](https://doi.org/10.1063/1.5063797).

Stefan Marinković, Alejandro Fernández-Rodríguez, Simon Collienne, Sylvain Blanco Alvarez, Sorin Melinte, Boris Maiorov, Gemma Rius, Xavier Granados, Narcis Mestres, Anna Palau y Alejandro V. Silhanek. "Direct Visualization of Current-Stimulated Oxygen Migration in $YBa_2Cu_3O_{7-\delta}$ Thin Films." In: *ACS Nano* 14, 9, 11765–11774 (2020). DOI: [10.1021/acsnano.0c04492](https://doi.org/10.1021/acsnano.0c04492).

Alejandro Fernández-Rodríguez, Jordi Alcalà, Jordi Suñe, Narcis Mestres y Anna Palau. "Multi-Terminal Transistor-Like Devices Based on Strongly Correlated Metallic Oxides for Neuromorphic Applications." In: *MDPI Materials* 13(2), 281 (2020). DOI: [10.3390/ma13020281](https://doi.org/10.3390/ma13020281).

List of contributors

Alejandro Fernández Rodríguez CSD deposition, optical lithography, sputter deposition, ion milling, wet etching, profilometer measurements, ultrasonic wire-bonding, transport measurements in PPMS, Resistive Switching in perovskite oxides, Source Measure Unit control programming with LabVIEW, Raman spectroscopy, X-ray absorption spectroscopy.

Dr. Florencio Sánchez & Raúl Solanas & Dr. Mengdi Qian: PLD deposition.

Dr. Anna Crespi & Xavier Campos & Joan Esquiú: XRD measurements.

Dr. Bernat Bozzo & Dr. Ferran Vallès: Electronic and magnetic measurements with SQUID.

Dr. Gemma Rius: Raman spectroscopy.

Dr. Xavier Granados: Numerical simulations using COMSOL Multiphysics.

Prof. Alejandro Silhanek & Stefan Marinkovic & X. D. A. Baumans: Electromigration experiments

Bibliography

- [1] Yoshinori Tokura, Masashi Kawasaki, and Naoto Nagaosa. “Emergent functions of quantum materials”. In: *Nature Physics* 13.11 (2017), pp. 1056–1068. ISSN: 1745-2481. DOI: [10.1038/nphys4274](https://doi.org/10.1038/nphys4274).
- [2] J. H. de Boer and E. J. W. Verwey. “Semi-conductors with partially and with completely filled 3d-lattice bands”. In: *Proceedings of the Physical Society* 49.4S (1937), pp. 59–71. ISSN: 0959-5309. DOI: [10.1088/0959-5309/49/4s/307](https://doi.org/10.1088/0959-5309/49/4s/307).
- [3] N. F. Mott and R. Peierls. “Discussion of the paper by de Boer and Verwey”. In: *Proceedings of the Physical Society* 49.4S (1937), pp. 72–73. ISSN: 0959-5309. DOI: [10.1088/0959-5309/49/4s/308](https://doi.org/10.1088/0959-5309/49/4s/308).
- [4] E. J. W. Verwey. “Electronic Conduction of Magnetite (Fe_3O_4) and its Transition Point at Low Temperatures”. In: *Nature* 144.3642 (1939), pp. 327–328. ISSN: 1476-4687. DOI: [10.1038/144327b0](https://doi.org/10.1038/144327b0).
- [5] Hasan Bakheet. *Theoretical and Experimental Study For (CdSe) Nanoparticles*. 2019.
- [6] N. F. Mott. “The Basis of the Electron Theory of Metals, with Special Reference to the Transition Metals”. In: *Proceedings of the Physical Society. Section A* 62.7 (1949), pp. 416–422. DOI: [10.1088/0370-1298/62/7/303](https://doi.org/10.1088/0370-1298/62/7/303).
- [7] N. F. Mott. “Metal-Insulator Transition”. In: *Rev. Mod. Phys.* 40 (4 1968), pp. 677–683. DOI: [10.1103/RevModPhys.40.677](https://doi.org/10.1103/RevModPhys.40.677).
- [8] J. Hubbard and Brian Hilton Flowers. “Electron correlations in narrow energy bands”. In: *Proceedings of the Royal Society of London. Series A. Mathematical and Physical Sciences* 276.1365 (1963), pp. 238–257. DOI: [10.1098/rspa.1963.0204](https://doi.org/10.1098/rspa.1963.0204).
- [9] J. Hubbard and Brian Hilton Flowers. “Electron correlations in narrow energy bands. II. The degenerate band case”. In: *Proceedings of the Royal Society of London. Series A. Mathematical and Physical Sciences* 277.1369 (1964), pp. 237–259. DOI: [10.1098/rspa.1964.0019](https://doi.org/10.1098/rspa.1964.0019).

- [10] J. Hubbard and Brian Hilton Flowers. “Electron correlations in narrow energy bands III. An improved solution”. In: *Proceedings of the Royal Society of London. Series A. Mathematical and Physical Sciences* 281.1386 (1964), pp. 401–419. DOI: [10.1098/rspa.1964.0190](https://doi.org/10.1098/rspa.1964.0190).
- [11] Masatoshi Imada, Atsushi Fujimori, and Yoshinori Tokura. “Metal-insulator transitions”. In: *Rev. Mod. Phys.* 70 (4 1998), pp. 1039–1263. DOI: [10.1103/RevModPhys.70.1039](https://doi.org/10.1103/RevModPhys.70.1039).
- [12] Etienne Janod et al. “Resistive Switching in Mott Insulators and Correlated Systems”. In: *Advanced Functional Materials* 25.40 (2015), pp. 6287–6305. DOI: <https://doi.org/10.1002/adfm.201500823>.
- [13] C Acha and M J Rozenberg. “Non-volatile resistive switching in the dielectric superconductor $\text{YBa}_2\text{Cu}_3\text{O}_{7-\delta}$ ”. In: *Journal of Physics: Condensed Matter* 21.4 (2009), p. 045702. DOI: [10.1088/0953-8984/21/4/045702](https://doi.org/10.1088/0953-8984/21/4/045702).
- [14] César Moreno et al. “Reversible Resistive Switching and Multilevel Recording in $\text{La}_{0.7}\text{Sr}_{0.3}\text{MnO}_3$ Thin Films for Low Cost Nonvolatile Memories”. In: *Nano Lett.* 10.10 (2010), pp. 3828–3835. ISSN: 1530-6984. DOI: [10.1021/nl1008162](https://doi.org/10.1021/nl1008162).
- [15] Juan Carlos Gonzalez-Rosillo et al. “Volume Resistive Switching in metallic perovskite oxides driven by the Metal-Insulator Transition”. In: *Journal of Electroceramics* 39.1 (2017), pp. 185–196. ISSN: 1573-8663. DOI: [10.1007/s10832-017-0101-2](https://doi.org/10.1007/s10832-017-0101-2).
- [16] Akihito Sawa. “Resistive switching in transition metal oxides”. In: *Materials Today* 11.6 (2008), pp. 28–36. ISSN: 1369-7021. DOI: [https://doi.org/10.1016/S1369-7021\(08\)70119-6](https://doi.org/10.1016/S1369-7021(08)70119-6).
- [17] Rainer Waser et al. “Redox-Based Resistive Switching Memories – Nanoionic Mechanisms, Prospects, and Challenges”. In: *Advanced Materials* 21.25-26 (2009), pp. 2632–2663. DOI: <https://doi.org/10.1002/adma.200900375>.
- [18] Y. Tsymbal Evgeny and Kohlstedt Hermann. “Tunneling Across a Ferroelectric”. In: *Science* 313.5784 (2006), pp. 181–183. DOI: [10.1126/science.1126230](https://doi.org/10.1126/science.1126230).
- [19] Ilia Valov et al. “Electrochemical metallization memories—fundamentals, applications, prospects”. In: *Nanotechnology* 22.28 (2011), p. 289502. DOI: [10.1088/0957-4484/22/28/289502](https://doi.org/10.1088/0957-4484/22/28/289502).

- [20] A. Asamitsu et al. “Current switching of resistive states in magnetoresistive manganites”. In: *Nature* 388.6637 (1997), pp. 50–52. ISSN: 1476-4687. DOI: [10.1038/40363](https://doi.org/10.1038/40363).
- [21] Pablo Stoliar et al. “Universal Electric-Field-Driven Resistive Transition in Narrow-Gap Mott Insulators”. In: *Advanced Materials* 25.23 (2013), pp. 3222–3226. DOI: <https://doi.org/10.1002/adma.201301113>.
- [22] J. G. Simmons, R. R. Verderber, and Nevill Francis Mott. “New conduction and reversible memory phenomena in thin insulating films”. In: *Proceedings of the Royal Society of London. Series A. Mathematical and Physical Sciences* 301.1464 (1967), pp. 77–102. DOI: [10.1098/rspa.1967.0191](https://doi.org/10.1098/rspa.1967.0191).
- [23] A. Sawa et al. “Interface resistance switching at a few nanometer thick perovskite manganite active layers”. In: *Applied Physics Letters* 88.23 (2006), p. 232112. DOI: [10.1063/1.2211147](https://doi.org/10.1063/1.2211147).
- [24] R. Ortega-Hernandez et al. “Resistive switching in $\text{CeO}_2/\text{La}_{0.8}\text{Sr}_{0.2}\text{MnO}_3$ bilayer for non-volatile memory applications”. In: *Microelectronic Engineering* 147 (2015). Insulating Films on Semiconductors 2015, pp. 37–40. ISSN: 0167-9317. DOI: <https://doi.org/10.1016/j.mee.2015.04.042>.
- [25] Juan Carlos Gonzalez-Rosillo et al. “Engineering Oxygen Migration for Homogeneous Volume Resistive Switching in 3-Terminal Devices”. In: *Advanced Electronic Materials* 5.9 (2019), p. 1800629. DOI: <https://doi.org/10.1002/aelm.201800629>.
- [26] H.K. Onnes. “The superconductivity of mercury”. In: *Comm. Phys. Lab. Univ. Leiden* (1911), pp. 122–124.
- [27] J. G. Bednorz and K. A. Müller. “Possible high T_c superconductivity in the Ba-La-Cu-O system”. In: *Zeitschrift für Physik B Condensed Matter* 64.2 (1986), pp. 189–193. ISSN: 1431-584X. DOI: [10.1007/BF01303701](https://doi.org/10.1007/BF01303701).
- [28] Dirk van Delft and Peter Kes. “The discovery of superconductivity”. In: *Physics Today* 63.9 (2010), pp. 38–43. DOI: [10.1063/1.3490499](https://doi.org/10.1063/1.3490499).

- [29] Pusheng Yuan et al. "Vortex pinning properties in Co-doped BaFe₂As₂ thin films with a high critical current density over 2 MA cm⁻² at 9 T". In: *Superconductor Science and Technology* 30.2 (2016), p. 025001. ISSN: 1361-6668. DOI: [10 . 1088 / 0953 - 2048 / 30 / 2 / 025001](https://doi.org/10.1088/0953-2048/30/2/025001).
- [30] Anna Palau et al. "6. Vortex dynamics in nanofabricated chemical solution deposition high-temperature superconducting films: Superconductors at the Nanoscale: From Basic Research to Applications". In: ed. by Roger Wördenweber et al. De Gruyter, 2017, pp. 195–220. DOI: [10 . 1515/9783110456806-007](https://doi.org/10.1515/9783110456806-007).
- [31] K. J. Kihlstrom et al. "Large enhancement of the in-field critical current density of YBCO coated conductors due to composite pinning landscape". In: *Superconductor Science and Technology* 34.1 (2020), p. 015011. ISSN: 1361-6668. DOI: [10 . 1088/1361-6668/ab9f64](https://doi.org/10.1088/1361-6668/ab9f64).
- [32] R. Algarni et al. "Enhanced critical current density and flux pinning traits with Dy₂O₃ nanoparticles added to YBa₂Cu₃O_{7-d} superconductor". In: *Journal of Alloys and Compounds* 852 (2021), p. 157019. ISSN: 0925-8388. DOI: [10 . 1016/j . jallcom . 2020 . 157019](https://doi.org/10.1016/j.jallcom.2020.157019).
- [33] Akira Tonomura. "Conveyor belts for magnetic flux quanta". In: *Nature Materials* 5.4 (2006), pp. 257–258. ISSN: 1476-4660. DOI: [10 . 1038/nmat1624](https://doi.org/10.1038/nmat1624).
- [34] O. V. Dobrovolskiy et al. "Ultra-fast vortex motion in a direct-write Nb-C superconductor". In: *Nature Communications* 11.1 (2020), p. 3291. ISSN: 2041-1723. DOI: [10 . 1038/s41467-020-16987-y](https://doi.org/10.1038/s41467-020-16987-y).
- [35] Neven Barisic et al. "Universal sheet resistance and revised phase diagram of the cuprate high-temperature superconductors". In: *Proc Natl Acad Sci USA* 110.30 (2013), p. 12235. DOI: [10 . 1073 / pnas . 1301989110](https://doi.org/10.1073/pnas.1301989110).
- [36] Louis Taillefer. "Scattering and Pairing in Cuprate Superconductors". In: *Annual Review of Condensed Matter Physics* 1.1 (2010), pp. 51–70. DOI: [10 . 1146/annurev-conmatphys-070909-104117](https://doi.org/10.1146/annurev-conmatphys-070909-104117).
- [37] S. J. Rothman, J. L. Routbort, and J. E. Baker. "Tracer diffusion of oxygen in YBa₂Cu₃O_{7-δ}". In: *Phys. Rev. B* 40 (13 1989), pp. 8852–8860. DOI: [10 . 1103/PhysRevB . 40 . 8852](https://doi.org/10.1103/PhysRevB.40.8852).

- [38] N. Markovic et al. “Superconductor-insulator transition in two dimensions”. In: *Phys. Rev. B* 60 (6 1999), pp. 4320–4328. DOI: [10 . 1103/PhysRevB.60.4320](https://doi.org/10.1103/PhysRevB.60.4320).
- [39] A.M. Goldman. “Superconductor–insulator transitions in the two-dimensional limit”. In: *Physica E: Low-dimensional Systems and Nanostructures* 18.1 (2003). 23rd International Conference on Low Temperature Physics (LT23), pp. 1–6. ISSN: 1386-9477. DOI: [https://doi.org/10.1016/S1386-9477\(02\)00932-3](https://doi.org/10.1016/S1386-9477(02)00932-3).
- [40] Yonatan Dubi, Yigal Meir, and Yshai Avishai. “Nature of the superconductor-insulator transition in disordered superconductors”. In: *Nature* 449.7164 (2007), pp. 876–880. ISSN: 1476-4687. DOI: [10.1038/nature06180](https://doi.org/10.1038/nature06180).
- [41] Nyayabanta Swain and Madhuparna Karmakar. “Strain-induced superconductor-insulator transition on a Lieb lattice”. In: *Phys. Rev. Research* 2 (2 2020), p. 023136. DOI: [10.1103/PhysRevResearch.2.023136](https://doi.org/10.1103/PhysRevResearch.2.023136).
- [42] Ruoting Yin et al. “Reversible Superconductor-Insulator Transition in (Li, Fe)OHFeSe Flakes Visualized by Gate-Tunable Scanning Tunneling Spectroscopy”. In: *ACS Nano* 14.6 (2020), pp. 7513–7519. ISSN: 1936-0851. DOI: [10.1021/acsnano.0c03289](https://doi.org/10.1021/acsnano.0c03289).
- [43] Han-Byul Jang, Ji Soo Lim, and Chan-Ho Yang. “Film-thickness-driven superconductor to insulator transition in cuprate superconductors”. In: *Scientific Reports* 10.1 (2020), p. 3236. ISSN: 2045-2322. DOI: [10.1038/s41598-020-60037-y](https://doi.org/10.1038/s41598-020-60037-y).
- [44] A. T. Bollinger et al. “Superconductor-insulator transition in $\text{La}_{2-x}\text{Sr}_x\text{CuO}_4$ at the pair quantum resistance.” eng. In: *Nature* 472 (7344 2011), pp. 458–60.
- [45] Fang Wang et al. “Superconductor-insulator transition in space charge doped one unit cell $\text{Bi}_{2.1}\text{Sr}_{1.9}\text{CaCu}_2\text{O}_{8+x}$ ”. In: *Nature Communications* 12.1 (2021), p. 2926. ISSN: 2041-1723. DOI: [10.1038/s41467-021-23183-z](https://doi.org/10.1038/s41467-021-23183-z).
- [46] Xiang Leng. “Superconductor-Insulator Transition Induced by Electrostatic Charging in High Temperature Superconductors”. In: (2011).

- [47] Tayfun Gokmen and Yurii Vlasov. “Acceleration of Deep Neural Network Training with Resistive Cross-Point Devices: Design Considerations”. In: *Frontiers in Neuroscience* 10 (2016). ISSN: 1662-453X. DOI: [10.3389/fnins.2016.00333](https://doi.org/10.3389/fnins.2016.00333).
- [48] Paul M. Solomon. “Analog neuromorphic computing using programmable resistor arrays”. In: *Solid-State Electronics* 155 (2019), pp. 82–92. ISSN: 0038-1101. DOI: [10.1016/j.sse.2019.03.023](https://doi.org/10.1016/j.sse.2019.03.023).
- [49] Manan Suri et al. “Bio-Inspired Stochastic Computing Using Binary CBRAM Synapses”. In: *IEEE Transactions on Electron Devices* 60.7 (2013), pp. 2402–2409. DOI: [10.1109/TED.2013.2263000](https://doi.org/10.1109/TED.2013.2263000).
- [50] Shimeng Yu et al. “Stochastic learning in oxide binary synaptic device for neuromorphic computing”. In: *Frontiers in Neuroscience* 7 (2013), p. 186. ISSN: 1662-453X. DOI: [10.3389/fnins.2013.00186](https://doi.org/10.3389/fnins.2013.00186).
- [51] Duygu Kuzum, Shimeng Yu, and H-S Philip Wong. “Synaptic electronics: materials, devices and applications”. In: *Nanotechnology* 24.38 (2013), p. 382001. DOI: [10.1088/0957-4484/24/38/382001](https://doi.org/10.1088/0957-4484/24/38/382001).
- [52] Chang Jin Wan et al. “Flexible Metal Oxide/Graphene Oxide Hybrid Neuromorphic Transistors on Flexible Conducting Graphene Substrates”. In: *Advanced Materials* 28.28 (2016), pp. 5878–5885. DOI: <https://doi.org/10.1002/adma.201600820>.
- [53] Chang Jin Wan et al. “Proton-Conducting Graphene Oxide-Coupled Neuron Transistors for Brain-Inspired Cognitive Systems”. In: *Advanced Materials* 28.18 (2016), pp. 3557–3563. DOI: <https://doi.org/10.1002/adma.201505898>.
- [54] Adnan Mehonic and Anthony J. Kenyon. “Emulating the Electrical Activity of the Neuron Using a Silicon Oxide RRAM Cell”. In: *Frontiers in Neuroscience* 10 (2016), p. 57. ISSN: 1662-453X. DOI: [10.3389/fnins.2016.00057](https://doi.org/10.3389/fnins.2016.00057).
- [55] Pablo Stoliar et al. “A Leaky-Integrate-and-Fire Neuron Analog Realized with a Mott Insulator”. In: *Advanced Functional Materials* 27.11 (2017), p. 1604740. DOI: <https://doi.org/10.1002/adfm.201604740>.
- [56] Wesley H. Brigner et al. “Three Artificial Spintronic Leaky Integrate-and-Fire Neurons”. In: *SPIN* 10.02 (2020), p. 2040003. DOI: [10.1142/S2010324720400032](https://doi.org/10.1142/S2010324720400032).

- [57] Guang Chen et al. “Multi-Cue Event Information Fusion for Pedestrian Detection With Neuromorphic Vision Sensors”. In: *Frontiers in Neurorobotics* 13 (2019), p. 10. ISSN: 1662-5218. DOI: [10.3389/fnbot.2019.00010](https://doi.org/10.3389/fnbot.2019.00010).
- [58] Andy Thomas. “Memristor-based neural networks”. In: *Journal of Physics D: Applied Physics* 46.9 (2013), p. 093001. DOI: [10.1088/0022-3727/46/9/093001](https://doi.org/10.1088/0022-3727/46/9/093001).
- [59] Tino Zaehle, Stefan Rach, and Christoph S. Herrmann. “Transcranial Alternating Current Stimulation Enhances Individual Alpha Activity in Human EEG”. In: *PLOS ONE* 5.11 (2010), pp. 1–7. DOI: [10.1371/journal.pone.0013766](https://doi.org/10.1371/journal.pone.0013766).
- [60] Daniele Ielmini and Stefano Ambrogio. “Emerging neuromorphic devices”. In: *Nanotechnology* 31.9 (2019), p. 092001. DOI: [10.1088/1361-6528/ab554b](https://doi.org/10.1088/1361-6528/ab554b).
- [61] Sung Hyun Jo et al. “Nanoscale Memristor Device as Synapse in Neuromorphic Systems”. In: *Nano Lett.* 10.4 (2010), pp. 1297–1301. ISSN: 1530-6984. DOI: [10.1021/nl904092h](https://doi.org/10.1021/nl904092h).
- [62] Yi Wu et al. “AlO_x-Based Resistive Switching Device with Gradual Resistance Modulation for Neuromorphic Device Application”. In: *2012 4th IEEE International Memory Workshop*. 2012, pp. 1–4. DOI: [10.1109/IMW.2012.6213663](https://doi.org/10.1109/IMW.2012.6213663).
- [63] Sungjun Kim et al. “Analog Synaptic Behavior of a Silicon Nitride Memristor”. In: *ACS Appl. Mater. Interfaces* 9.46 (2017), pp. 40420–40427. ISSN: 1944-8244. DOI: [10.1021/acsmi.7b11191](https://doi.org/10.1021/acsmi.7b11191).
- [64] Shimeng Yu et al. “Scaling-up resistive synaptic arrays for neuro-inspired architecture: Challenges and prospect”. In: *2015 IEEE International Electron Devices Meeting (IEDM)*. 2015, pp. 17.3.1–17.3.4. DOI: [10.1109/IEDM.2015.7409718](https://doi.org/10.1109/IEDM.2015.7409718).
- [65] Hong Han et al. “Recent Progress in Three-Terminal Artificial Synapses: From Device to System”. In: *Small* 15.32 (2019), p. 1900695. DOI: <https://doi.org/10.1002/sml1.201900695>.
- [66] Li Qiang Zhu et al. “Artificial synapse network on inorganic proton conductor for neuromorphic systems”. In: *Nature Communications* 5.1 (2014), p. 3158. ISSN: 2041-1723. DOI: [10.1038/ncomms4158](https://doi.org/10.1038/ncomms4158).

- [67] Guangyang Gou et al. “Artificial synapses based on biopolymer electrolyte-coupled SnO₂ nanowire transistors”. In: *J. Mater. Chem. C* 4 (47 2016), pp. 11110–11117. DOI: [10.1039/C6TC03731C](https://doi.org/10.1039/C6TC03731C).
- [68] Vinod K. Sangwan et al. “Multi-terminal memtransistors from polycrystalline monolayer molybdenum disulfide”. In: *Nature* 554.7693 (2018), pp. 500–504. ISSN: 1476-4687. DOI: [10.1038/nature25747](https://doi.org/10.1038/nature25747).
- [69] Alison Stoddart. “Electronic devices: Making multi-terminal memtransistors”. In: *Nature Reviews Materials* 3.3 (2018), p. 18014. ISSN: 2058-8437. DOI: [10.1038/natrevmats.2018.14](https://doi.org/10.1038/natrevmats.2018.14).
- [70] Rajiv K Singh and Dhananjay Kumar. “Pulsed laser deposition and characterization of high-T_c YBa₂Cu₃O_{7-x} superconducting thin films”. In: *Materials Science and Engineering: R: Reports* 22.4 (1998), pp. 113–185. ISSN: 0927-796X. DOI: [10.1016/S0927-796X\(97\)00019-3](https://doi.org/10.1016/S0927-796X(97)00019-3).
- [71] X Obradors et al. “Growth, nanostructure and vortex pinning in superconducting YBa₂Cu₃O₇ thin films based on trifluoroacetate solutions”. In: *Superconductor Science and Technology* 25.12 (2012), p. 123001. DOI: [10.1088/0953-2048/25/12/123001](https://doi.org/10.1088/0953-2048/25/12/123001).
- [72] M. Lorenz et al. “Large-area double-side pulsed laser deposition of YBa₂Cu₃O_{7-x} thin films on 3-in. sapphire wafers”. In: *Appl. Phys. Lett.* 68.23 (1996), pp. 3332–3334. ISSN: 0003-6951. DOI: [10.1063/1.116048](https://doi.org/10.1063/1.116048).
- [73] D. M. Feldmann et al. “Influence of growth temperature on critical current and magnetic flux pinning structures in YBa₂Cu₃O_{7-x}”. In: *Appl. Phys. Lett.* 91.16 (2007), p. 162501. ISSN: 0003-6951. DOI: [10.1063/1.2799875](https://doi.org/10.1063/1.2799875).
- [74] S. R. Foltyn et al. “Strongly coupled critical current density values achieved in Y₁Ba₂Cu₃O_{7-δ} coated conductors with near-single-crystal texture”. In: *Appl. Phys. Lett.* 82.25 (2003), pp. 4519–4521. ISSN: 0003-6951. DOI: [10.1063/1.1584783](https://doi.org/10.1063/1.1584783).
- [75] L. Civale et al. “Understanding High Critical Currents in YBa₂Cu₃O₇ Thin Films and Coated Conductors”. In: *Journal of Low Temperature Physics* 135.1 (2004), pp. 87–98. ISSN: 1573-7357. DOI: [10.1023/B:JOLT.0000016966.07449.d1](https://doi.org/10.1023/B:JOLT.0000016966.07449.d1).

- [76] X. Obradors et al. “Chemical solution route to self-assembled epitaxial oxide nanostructures”. In: *Chem. Soc. Rev.* 43.7 (2014), pp. 2200–2225. ISSN: 0306-0012. DOI: [10.1039/C3CS60365B](https://doi.org/10.1039/C3CS60365B).
- [77] B. Dam, J. M. Huijbregtse, and J. H. Rector. “Strong pinning linear defects formed at the coherent growth transition of pulsed-laser-deposited $\text{YBa}_2\text{Cu}_3\text{O}_{7-\delta}$ films”. In: *Phys. Rev. B* 65 (6 2002), p. 064528. DOI: [10.1103/PhysRevB.65.064528](https://doi.org/10.1103/PhysRevB.65.064528).
- [78] A. Goyal et al. “Irradiation-free, columnar defects comprised of self-assembled nanodots and nanorods resulting in strongly enhanced flux-pinning in $\text{YBa}_2\text{Cu}_3\text{O}_{7-\delta}$ films”. In: *Superconductor Science and Technology* 18.11 (2005), pp. 1533–1538. ISSN: 1361-6668. DOI: [10.1088/0953-2048/18/11/021](https://doi.org/10.1088/0953-2048/18/11/021).
- [79] B. Maiorov et al. “Synergetic combination of different types of defect to optimize pinning landscape using BaZrO_3 -doped $\text{YBa}_2\text{Cu}_3\text{O}_7$ ”. In: *Nature Materials* 8.5 (2009), pp. 398–404. ISSN: 1476-4660. DOI: [10.1038/nmat2408](https://doi.org/10.1038/nmat2408).
- [80] Robert W. Schwartz. “Chemical Solution Deposition of Perovskite Thin Films”. In: *Chem. Mater.* 9.11 (1997), pp. 2325–2340. ISSN: 0897-4756. DOI: [10.1021/cm970286f](https://doi.org/10.1021/cm970286f).
- [81] Robert W. Schwartz, Theodor Schneller, and Rainer Waser. “Chemical solution deposition of electronic oxide films”. In: *Comptes Rendus Chimie* 7.5 (2004), pp. 433–461. ISSN: 1631-0748. DOI: [10.1016/j.crci.2004.01.007](https://doi.org/10.1016/j.crci.2004.01.007).
- [82] A. Queraltó et al. “Growth of ferroelectric $\text{Ba}_{0.8}\text{Sr}_{0.2}\text{TiO}_3$ epitaxial films by ultraviolet pulsed laser irradiation of chemical solution derived precursor layers”. In: *Appl. Phys. Lett.* 106.26 (2015), p. 262903. ISSN: 0003-6951. DOI: [10.1063/1.4923376](https://doi.org/10.1063/1.4923376).
- [83] C. Moreno et al. “Nanocomposite lanthanum strontium manganite thin films formed by using a chemical solution deposition”. In: *Appl. Phys. Lett.* 100.2 (2012), p. 023103. ISSN: 0003-6951. DOI: [10.1063/1.3675461](https://doi.org/10.1063/1.3675461).
- [84] J. Zabaleta et al. “Nanoscale magnetic structure and properties of solution-derived self-assembled $\text{La}_{0.7}\text{Sr}_{0.3}\text{MnO}_3$ islands”. In: *Journal of Applied Physics* 111.2 (2012), p. 024307. ISSN: 0021-8979. DOI: [10.1063/1.3677985](https://doi.org/10.1063/1.3677985).

- [85] X. Obradors et al. “Progress towards all-chemical superconducting $\text{YBa}_2\text{Cu}_3\text{O}_7$ -coated conductors”. In: *Superconductor Science and Technology* 19.3 (2006), S13–S26. ISSN: 1361-6668. DOI: [10.1088/0953-2048/19/3/003](https://doi.org/10.1088/0953-2048/19/3/003).
- [86] A. Gupta et al. “Superconducting oxide films with high transition temperature prepared from metal trifluoroacetate precursors”. In: *Appl. Phys. Lett.* 52.24 (1988), pp. 2077–2079. ISSN: 0003-6951. DOI: [10.1063/1.99752](https://doi.org/10.1063/1.99752).
- [87] N. Roma et al. “Acid anhydrides: a simple route to highly pure organometallic solutions for superconducting films”. In: *Superconductor Science and Technology* 19.6 (2006), pp. 521–527. ISSN: 1361-6668. DOI: [10.1088/0953-2048/19/6/019](https://doi.org/10.1088/0953-2048/19/6/019).
- [88] William Henry Bragg and William Lawrence Bragg. “The reflection of X-rays by crystals”. In: *Proceedings of the Royal Society of London. Series A, Containing Papers of a Mathematical and Physical Character* 88.605 (1913), pp. 428–438. DOI: [10.1098/rspa.1913.0040](https://doi.org/10.1098/rspa.1913.0040).
- [89] Brahim Tlili. “Caractérisation de films durs multicouches élaborés par pulvérisation magnétron. Influence des conditions d’élaboration sur leurs propriétés.” date de rédaction: 30/07/2010. Theses. Arts et Métiers ParisTech, 2010.
- [90] T.C. Huang, R. Gilles, and G. Will. “Thin-film thickness and density determination from x-ray reflectivity data using a conventional power diffractometer”. In: *Thin Solid Films* 230.2 (1993), pp. 99–101. ISSN: 0040-6090. DOI: [https://doi.org/10.1016/0040-6090\(93\)90499-F](https://doi.org/10.1016/0040-6090(93)90499-F).
- [91] B.D. Josephson. “Possible new effects in superconductive tunnelling”. In: *Physics Letters* 1.7 (1962), pp. 251–253. ISSN: 0031-9163. DOI: [https://doi.org/10.1016/0031-9163\(62\)91369-0](https://doi.org/10.1016/0031-9163(62)91369-0).
- [92] R. C. Jaklevic et al. “Quantum Interference Effects in Josephson Tunneling”. In: *Phys. Rev. Lett.* 12 (7 1964), pp. 159–160. DOI: [10.1103/PhysRevLett.12.159](https://doi.org/10.1103/PhysRevLett.12.159).
- [93] M. Buchner et al. “Tutorial: Basic principles, limits of detection, and pitfalls of highly sensitive SQUID magnetometry for nanomagnetism and spintronics”. In: *Journal of Applied Physics* 124.16 (2018), p. 161101. DOI: [10.1063/1.5045299](https://doi.org/10.1063/1.5045299).

- [94] L.J. Van der Pauw. “A Method of Measuring the Resistivity and Hall Coefficient on Lamellae of Arbitrary Shape”. In: *Philips Technical Review* 20 (1958), pp. 220–224.
- [95] S. Murase et al. “Critical temperature measurement method of composite superconductors”. In: *Physica C: Superconductivity* 357-360 (2001), pp. 1197–1200. ISSN: 0921-4534. DOI: [https://doi.org/10.1016/S0921-4534\(01\)00483-X](https://doi.org/10.1016/S0921-4534(01)00483-X).
- [96] C. P. Bean. “Magnetization of Hard Superconductors”. In: *Phys. Rev. Lett.* 8 (6 1962), pp. 250–253. DOI: [10.1103/PhysRevLett.8.250](https://doi.org/10.1103/PhysRevLett.8.250).
- [97] Vyacheslav S. Zharinov et al. “Controlled electromigration protocol revised”. In: *Review of Scientific Instruments* 89.4 (2018), p. 043904. DOI: [10.1063/1.5011953](https://doi.org/10.1063/1.5011953).
- [98] X. D. A. Baumans et al. “Electromigration in the dissipative state of high-temperature superconducting bridges”. In: *Applied Physics Letters* 114.1 (2019), p. 012601. DOI: [10.1063/1.5063797](https://doi.org/10.1063/1.5063797).
- [99] M. S. Raven and Y. M. Wan. “Hall effect of as-grown oxygen-deficient $\text{YBa}_2\text{Cu}_3\text{O}_x$ thin films”. In: *Phys. Rev. B* 51 (1 1995), pp. 561–567. DOI: [10.1103/PhysRevB.51.561](https://doi.org/10.1103/PhysRevB.51.561).
- [100] B Wuyts, VV Moshchalkov, and Y Bruynseraede. “Resistivity and Hall effect of metallic oxygen-deficient $\text{YBa}_2\text{Cu}_3\text{O}_x$ films in the normal state”. In: *Physical review B* 53.14 (1996), p. 9418.
- [101] Kouji Segawa and Yoichi Ando. “Intrinsic Hall response of the CuO_2 planes in a chain-plane composite system of $\text{YBa}_2\text{Cu}_3\text{O}_y$ ”. In: *Phys. Rev. B* 69 (10 2004), p. 104521. DOI: [10.1103/PhysRevB.69.104521](https://doi.org/10.1103/PhysRevB.69.104521).
- [102] Giuseppe Dattoli. “The fine structure constant and numerical alchemy”. In: (2010).
- [103] E. H. Hall. “On a New Action of the Magnet on Electric Currents”. In: *American Journal of Mathematics* 2.3 (1879), pp. 287–292. ISSN: 00029327, 10806377.
- [104] Chandrasekhara Venkata Raman. “A new radiation”. In: *Indian Journal of physics* 2 (1928), pp. 387–398.
- [105] B. Jalali et al. “Raman-based silicon photonics”. In: *IEEE Journal of Selected Topics in Quantum Electronics* 12.3 (2006), pp. 412–421. DOI: [10.1109/JSTQE.2006.872708](https://doi.org/10.1109/JSTQE.2006.872708).

- [106] E Faulques and S Lefrant. “Raman spectroscopy of superconducting materials”. In: *Condensed matter news* 5.3-4 (1996).
- [107] B. Friedl et al. “Intensity anomalies of Raman-active phonons in the superconducting state of $\text{YBa}_2\text{Cu}_3\text{O}_{7-\delta}$ ”. In: *Solid State Communications* 78.4 (1991), pp. 291–294. ISSN: 0038-1098. DOI: [https://doi.org/10.1016/0038-1098\(91\)90199-6](https://doi.org/10.1016/0038-1098(91)90199-6).
- [108] Rudolf Feile. “Lattice vibrations in high- T_c superconductors: Optical spectroscopy and lattice dynamics”. In: *Physica C: Superconductivity* 159.1 (1989), pp. 1–32. ISSN: 0921-4534. DOI: [https://doi.org/10.1016/0921-4534\(89\)90099-3](https://doi.org/10.1016/0921-4534(89)90099-3).
- [109] Pham Van Huong. “Microstructure of high temperature superconductor thin films as studied by micro-Raman spectroscopy”. In: *Physica C-superconductivity and Its Applications* 180 (1991), pp. 128–131.
- [110] M. Hangyo et al. “Effect of oxygen content on phonon Raman spectra of $\text{YBa}_2\text{Cu}_3\text{O}_{7-\delta}$ ”. In: *Solid State Communications* 65.8 (1988), pp. 835–839. ISSN: 0038-1098. DOI: [https://doi.org/10.1016/0038-1098\(88\)90515-7](https://doi.org/10.1016/0038-1098(88)90515-7).
- [111] Juan Carlos González González. “Coated Conductors and Chemical Solution Growth of YBCO Films: A Micro-Raman Spectroscopy Study”. PhD thesis. Universitat Autònoma de Barcelona, 2005.
- [112] Jinhua Ye and Keikichi Nakamura. “Quantitative structure analyses of $\text{YBa}_2\text{Cu}_3\text{O}_{7-\delta}$ thin films: Determination of oxygen content from x-ray-diffraction patterns”. In: *Phys. Rev. B* 48 (10 1993), pp. 7554–7564. DOI: [10.1103/PhysRevB.48.7554](https://doi.org/10.1103/PhysRevB.48.7554).
- [113] P. Zhang et al. “Raman spectra of ultrathin $\text{YBa}_2\text{Cu}_3\text{O}_{7-\delta}$ films”. In: *Journal of Applied Physics* 80.5 (1996), pp. 2935–2938. DOI: [10.1063/1.363149](https://doi.org/10.1063/1.363149).
- [114] V.A. Maroni, J Reeves, and G Schwab. “On-Line Characterization of YBCO Coated Conductors Using Raman Spectroscopy Methods”. In: *Applied spectroscopy* 61 (2007), pp. 359–66. DOI: [10.1366/000370207780466208](https://doi.org/10.1366/000370207780466208).

- [115] C. Thomsen et al. “Determination of the degree of epitaxy in high- T_c thin films by raman spectroscopy”. In: *Solid State Communications* 83.3 (1992), pp. 199–203. ISSN: 0038-1098. DOI: [10.1016/0038-1098\(92\)90837-Y](https://doi.org/10.1016/0038-1098(92)90837-Y).
- [116] C. Thomsen et al. “Systematic Raman and infrared studies of the superconductor $\text{YBa}_2\text{Cu}_3\text{O}_{7-x}$ as a function of oxygen concentration ($0 \leq x \leq 1$)”. In: *Solid State Communications* 65.1 (1988), pp. 55–58. ISSN: 0038-1098. DOI: [10.1016/0038-1098\(88\)90587-X](https://doi.org/10.1016/0038-1098(88)90587-X).
- [117] B. H. Moeckly, R. A. Buhrman, and P. E. Sulewski. “Micro-Raman spectroscopy of electromigration-induced oxygen vacancy aggregation in $\text{YBa}_2\text{Cu}_3\text{O}_{7-\delta}$ ”. In: *Applied Physics Letters* 64.11 (1994), pp. 1427–1429. DOI: [10.1063/1.111905](https://doi.org/10.1063/1.111905).
- [118] C Camerlingo, Ines Delfino, and Maria Lepore. “Micro-Raman spectroscopy on YBCO films during heat treatment”. In: *Superconductor Science and Technology* 15 (2002), p. 1606. DOI: [10.1088/0953-2048/15/11/321](https://doi.org/10.1088/0953-2048/15/11/321).
- [119] G. Thomsen C. Kaczmarczyk. “Handbook of Vibrational Spectroscopy”. In: ed. by John M. Chalmers and Peter R. Griffiths. John Wiley & Sons Ltd, 2002. Chap. Vibrational Raman Spectroscopy of High-temperature Superconductors, p. 2651.
- [120] S. J. Rothman et al. “Anisotropy of oxygen tracer diffusion in single-crystal $\text{YBa}_2\text{Cu}_3\text{O}_{7-\delta}$ ”. In: *Phys. Rev. B* 44 (5 1991), pp. 2326–2333. DOI: [10.1103/PhysRevB.44.2326](https://doi.org/10.1103/PhysRevB.44.2326).
- [121] Kouichi Semba and Azusa Matsuda. “Superconductor-to-Insulator Transition and Transport Properties of Underdoped $\text{YBa}_2\text{Cu}_3\text{O}_y$ Crystals”. In: *Phys. Rev. Lett.* 86 (3 2001), pp. 496–499. DOI: [10.1103/PhysRevLett.86.496](https://doi.org/10.1103/PhysRevLett.86.496).
- [122] J. Joshua Yang, Dmitri B. Strukov, and Duncan R. Stewart. “Memristive devices for computing”. In: *Nature Nanotechnology* 8.1 (2013), pp. 13–24. ISSN: 1748-3395. DOI: [10.1038/nnano.2012.240](https://doi.org/10.1038/nnano.2012.240).
- [123] Jae Sung Lee, Shinbuhm Lee, and Tae Won Noh. “Resistive switching phenomena: A review of statistical physics approaches”. In: *Applied Physics Reviews* 2.3 (2015), p. 031303. DOI: [10.1063/1.4929512](https://doi.org/10.1063/1.4929512).

- [124] S. Larentis et al. “Resistive Switching by Voltage-Driven Ion Migration in Bipolar RRAM—Part II: Modeling”. In: *IEEE Transactions on Electron Devices* 59.9 (2012), pp. 2468–2475. ISSN: 1557-9646. DOI: [10.1109/TED.2012.2202320](https://doi.org/10.1109/TED.2012.2202320).
- [125] Federico Nardi et al. “Complementary Switching in Oxide-Based Bipolar Resistive-Switching Random Memory”. In: *IEEE Transactions on Electron Devices* 60.1 (2013), pp. 70–77. DOI: [10.1109/TED.2012.2226728](https://doi.org/10.1109/TED.2012.2226728).
- [126] Yoshitaka Aoki et al. “Bulk mixed ion electron conduction in amorphous gallium oxide causes memristive behaviour”. In: *Nature Communications* 5.1 (2014), p. 3473. ISSN: 2041-1723. DOI: [10.1038/ncomms4473](https://doi.org/10.1038/ncomms4473).
- [127] A. Marchewka, R. Waser, and S. Menzel. “Physical simulation of dynamic resistive switching in metal oxides using a Schottky contact barrier model”. In: *2015 International Conference on Simulation of Semiconductor Processes and Devices (SISPAD)*. 2015, pp. 297–300. DOI: [10.1109/SISPAD.2015.7292318](https://doi.org/10.1109/SISPAD.2015.7292318).
- [128] Astrid Marchewka et al. “Nanoionic Resistive Switching Memories: On the Physical Nature of the Dynamic Reset Process”. In: *Adv. Electron. Mater.* 2.1 (2016), p. 1500233. ISSN: 2199-160X. DOI: [10.1002/aelm.201500233](https://doi.org/10.1002/aelm.201500233).
- [129] A. Marchewka, R. Waser, and S. Menzel. “A 2D axisymmetric dynamic drift-diffusion model for numerical simulation of resistive switching phenomena in metal oxides”. In: *2016 International Conference on Simulation of Semiconductor Processes and Devices (SISPAD)*. 2016, pp. 145–148. DOI: [10.1109/SISPAD.2016.7605168](https://doi.org/10.1109/SISPAD.2016.7605168).
- [130] Fu-Chien Chiu. “A Review on Conduction Mechanisms in Dielectric Films”. In: *Advances in Materials Science and Engineering* 2014 (2014), p. 578168. ISSN: 1687-8434. DOI: [10.1155/2014/578168](https://doi.org/10.1155/2014/578168).
- [131] C. Acha et al. “Transport mechanism through metal-cobaltite interfaces”. In: *Appl. Phys. Lett.* 109.1 (2016), p. 011603. ISSN: 0003-6951. DOI: [10.1063/1.4955204](https://doi.org/10.1063/1.4955204).
- [132] I.G. Baek et al. “Highly scalable nonvolatile resistive memory using simple binary oxide driven by asymmetric unipolar voltage pulses”. In: *IEDM Technical Digest. IEEE International Electron Devices Meeting, 2004*. 2004, pp. 587–590. DOI: [10.1109/IEDM.2004.1419228](https://doi.org/10.1109/IEDM.2004.1419228).

- [133] R. Oligschlaeger et al. “Resistive switching and data reliability of epitaxial (Ba, Sr)TiO₃ thin films”. In: *Applied Physics Letters* 88.4 (2006), p. 042901. DOI: [10.1063/1.2162860](https://doi.org/10.1063/1.2162860).
- [134] H. K. Lau and C. W. Leung. “Nonvolatile multilevel memory effect by resistive switching in manganite thin films”. In: *Journal of Applied Physics* 104.12 (2008), p. 123705. ISSN: 0021-8979. DOI: [10.1063/1.3043801](https://doi.org/10.1063/1.3043801).
- [135] Eike Linn et al. “Complementary resistive switches for passive nanocrossbar memories”. In: *Nature Materials* 9.5 (2010), pp. 403–406. ISSN: 1476-4660. DOI: [10.1038/nmat2748](https://doi.org/10.1038/nmat2748).
- [136] A. Michaelis et al. “A study of oxygen diffusion in and out of YBa₂Cu₃O_{7- δ} thin films”. In: *Journal of Applied Physics* 83.12 (1998), pp. 7736–7743. ISSN: 0021-8979. DOI: [10.1063/1.367947](https://doi.org/10.1063/1.367947).
- [137] J R Lloyd. “Electromigration in thin film conductors”. In: *Semiconductor Science and Technology* 12.10 (1997), pp. 1177–1185. DOI: [10.1088/0268-1242/12/10/002](https://doi.org/10.1088/0268-1242/12/10/002).
- [138] Ventsislav K. Valev et al. “Plasmon-Enhanced Sub-Wavelength Laser Ablation: Plasmonic Nanojets”. In: *Adv. Mater.* 24.10 (2012), OP29–OP35. ISSN: 0935-9648. DOI: [10.1002/adma.201103807](https://doi.org/10.1002/adma.201103807).
- [139] Surya Prakash Gurunaryanan et al. “Electrically Driven Unidirectional Optical Nanoantennas”. In: *Nano Lett.* 17.12 (2017), pp. 7433–7439. ISSN: 1530-6984. DOI: [10.1021/acs.nanolett.7b03312](https://doi.org/10.1021/acs.nanolett.7b03312).
- [140] Chun-Yeol You, In Mo Sung, and Byung-Kyu Joe. “Analytic expression for the temperature of the current-heated nanowire for the current-induced domain wall motion”. In: *Appl. Phys. Lett.* 89.22 (2006), p. 222513. ISSN: 0003-6951. DOI: [10.1063/1.2399441](https://doi.org/10.1063/1.2399441).
- [141] P. Parkin Stuart S., Hayashi Masamitsu, and Thomas Luc. “Magnetic Domain-Wall Racetrack Memory”. In: *Science* 320.5873 (2008), pp. 190–194. DOI: [10.1126/science.1145799](https://doi.org/10.1126/science.1145799).
- [142] D Staudt and R Hoffmann-Vogel. “Controlled electromigration of thin Pb films started from the normal and from the superconducting state”. In: *Journal of Physics D: Applied Physics* 50.18 (2017), p. 185301. DOI: [10.1088/1361-6463/aa67c6](https://doi.org/10.1088/1361-6463/aa67c6).

- [143] K. Govinda Rajan et al. “Electromigration of oxygen in $\text{YBa}_2\text{Cu}_3\text{O}_{7-\delta}$ ”. In: *Journal of Physics D: Applied Physics* 23.6 (1990), pp. 694–697. ISSN: 1361-6463. DOI: [10.1088/0022-3727/23/6/009](https://doi.org/10.1088/0022-3727/23/6/009).
- [144] Satish Vitta et al. “Electromigration failure in $\text{YBa}_2\text{Cu}_3\text{O}_{7-x}$ thin films”. In: *Appl. Phys. Lett.* 58.7 (1991), pp. 759–761. ISSN: 0003-6951. DOI: [10.1063/1.104539](https://doi.org/10.1063/1.104539).
- [145] G. N. Mikhailova et al. “Ion migration in high- T_c superconductors and the nature of the conducting state in d-wave superconductors”. In: *Inorganic Materials* 36.8 (2000), pp. 807–815. ISSN: 1608-3172. DOI: [10.1007/BF02758602](https://doi.org/10.1007/BF02758602).
- [146] Andrew J. Kerman et al. “Constriction-limited detection efficiency of superconducting nanowire single-photon detectors”. In: *Appl. Phys. Lett.* 90.10 (2007), p. 101110. ISSN: 0003-6951. DOI: [10.1063/1.2696926](https://doi.org/10.1063/1.2696926).
- [147] Ge He et al. “Combinatorial laser molecular beam epitaxy system integrated with specialized low-temperature scanning tunneling microscopy”. In: *Review of Scientific Instruments* 91.1 (2020), p. 013904. ISSN: 0034-6748. DOI: [10.1063/1.5119686](https://doi.org/10.1063/1.5119686).
- [148] Stefan Marinkovic. “Research master thesis: Direct Visualization of Current Stimulated Oxygen Migration in $\text{YBa}_2\text{Cu}_3\text{O}_{7-\delta}$ Thin Films”. MA thesis. Université de Liège, 2020.
- [149] Xavier D. A. Baumans et al. “Healing Effect of Controlled Anti-Electromigration on Conventional and High- T_c Superconducting Nanowires”. In: *Small* 13.26 (2017), p. 1700384. DOI: <https://doi.org/10.1002/sml1.201700384>.
- [150] Anna Palau et al. “Electrochemical Tuning of Metal Insulator Transition and Nonvolatile Resistive Switching in Superconducting Films”. In: *ACS Appl. Mater. Interfaces* 10.36 (2018), pp. 30522–30531. ISSN: 1944-8244. DOI: [10.1021/acsami.8b08042](https://doi.org/10.1021/acsami.8b08042).
- [151] Z. Li et al. “Degradation and subsequent healing by electromigration in Al-1 wt % Si thin films”. In: *Journal of Applied Physics* 72.5 (1992), pp. 1821–1832. ISSN: 0021-8979. DOI: [10.1063/1.351653](https://doi.org/10.1063/1.351653).

- [152] Chao-Fu Hong, Mitsuhiro Togo, and Koichiro Hoh. “Repair of Electromigration-Induced Voids in Aluminum Interconnection by Current Reversal”. In: *Japanese Journal of Applied Physics* 32.Part 2, No. 4B (1993), pp. L624–L627. ISSN: 0021-4922. DOI: [10.1143/jjap.32.1624](https://doi.org/10.1143/jjap.32.1624).
- [153] Chengxiang Xiang, Jung Yun Kim, and Reginald M. Penner. “Reconnectable Sub-5 nm Nanogaps in Ultralong Gold Nanowires”. In: *Nano Lett.* 9.5 (2009), pp. 2133–2138. ISSN: 1530-6984. DOI: [10.1021/nl900698s](https://doi.org/10.1021/nl900698s).
- [154] Tatiana Kozlova, Maria Rudneva, and Henny W. Zandbergen. “In situTEM and STEM studies of reversible electromigration in thin palladium-platinum bridges”. In: *Nanotechnology* 24.50 (2013), p. 505708. ISSN: 1361-6528. DOI: [10.1088/0957-4484/24/50/505708](https://doi.org/10.1088/0957-4484/24/50/505708).
- [155] J. Lombardo et al. “Electromigration-induced resistance switching in indented Al microstrips”. In: *New Journal of Physics* 21.11 (2019), p. 113015. ISSN: 1367-2630. DOI: [10.1088/1367-2630/ab5025](https://doi.org/10.1088/1367-2630/ab5025).
- [156] Joseph Lombardo et al. “In situ tailoring of superconducting junctions via electro-annealing”. In: *Nanoscale* 10 (4 2018), pp. 1987–1996. DOI: [10.1039/C7NR08571K](https://doi.org/10.1039/C7NR08571K).
- [157] Zheng Ming Wu et al. “Feedback controlled electromigration in four-terminal nanojunctions”. In: *Applied Physics Letters* 91.5 (2007), p. 053118. DOI: [10.1063/1.2760150](https://doi.org/10.1063/1.2760150).
- [158] K. Jin et al. “Anomalous enhancement of the superconducting transition temperature of electron-doped $\text{La}_{2-x}\text{Ce}_x\text{CuO}_4$ and $\text{Pr}_{2-x}\text{Ce}_x\text{CuO}_4$ cuprate heterostructures”. In: *PRB* 83.6 (2011), p. 060511. DOI: [10.1103/PhysRevB.83.060511](https://doi.org/10.1103/PhysRevB.83.060511).
- [159] J. Kircher et al. “Anisotropy and oxygen-stoichiometry dependence of the dielectric tensor of $\text{YBa}_2\text{Cu}_3\text{O}_{7-\delta}$ ($0 \leq \delta \leq 1$)”. In: *PRB* 44.1 (1991), pp. 217–224. DOI: [10.1103/PhysRevB.44.217](https://doi.org/10.1103/PhysRevB.44.217).
- [160] B. H. Moeckly, D. K. Lathrop, and R. A. Buhrman. “Electromigration study of oxygen disorder and grain-boundary effects in $\text{YBa}_2\text{Cu}_3\text{O}_{7-\delta}$ thin films”. In: *PRB* 47.1 (1993), pp. 400–417. DOI: [10.1103/PhysRevB.47.400](https://doi.org/10.1103/PhysRevB.47.400).

- [161] K. Kamarás et al. “Excitonic absorption and superconductivity in $\text{YBa}_2\text{Cu}_3\text{O}_{7-y}$ ”. In: *PRL* 59.8 (1987), pp. 919–922. DOI: [10.1103/PhysRevLett.59.919](https://doi.org/10.1103/PhysRevLett.59.919).
- [162] P. E. Sulewski et al. “Free-carrier relaxation dynamics in the normal state of sintered $\text{YBa}_2\text{Cu}_3\text{O}_{7-y}$ ”. In: *PRB* 36.4 (1987), pp. 2357–2360. DOI: [10.1103/PhysRevB.36.2357](https://doi.org/10.1103/PhysRevB.36.2357).
- [163] Guang-Lin Zhao et al. “Theoretical calculation of optical properties of Y-Ba-Cu-O superconductors”. In: *PRB* 36.13 (1987), pp. 7203–7206. DOI: [10.1103/PhysRevB.36.7203](https://doi.org/10.1103/PhysRevB.36.7203).
- [164] Ruixing Liang, D. A. Bonn, and W. N. Hardy. “Evaluation of CuO_2 plane hole doping in $\text{YBa}_2\text{Cu}_3\text{O}_{6+x}$ single crystals”. In: *Phys. Rev. B* 73 (18 2006), p. 180505. DOI: [10.1103/PhysRevB.73.180505](https://doi.org/10.1103/PhysRevB.73.180505).
- [165] Wenbin Zhang et al. “Analog-Type Resistive Switching Devices for Neuromorphic Computing”. In: *physica status solidi (RRL) – Rapid Research Letters* 13.10 (2019), p. 1900204. DOI: <https://doi.org/10.1002/pssr.201900204>.
- [166] Y. S. Lee et al. “Electrodynamics of the nodal metal state in weakly doped high- T_c cuprates”. In: *Phys. Rev. B* 72 (5 2005), p. 054529. DOI: [10.1103/PhysRevB.72.054529](https://doi.org/10.1103/PhysRevB.72.054529).